Gamma frequency entrainment attenuates amyloid load and modifies microglia

by

Hannah Frances Iaccarino
A.B., Dartmouth College (2012)

Submitted to the Department of Brain and Cognitive Sciences
in Partial Fulfillment of the Requirements for the Degree of

Doctor of Philosophy

at the

MASSACHUSETTS INSTITUTE OF TECHNOLOGY

January 2016 [February 2017]

Signature of Author Signature redacted

Hannah F. Iaccarino
Department of Brain and Cognitive Sciences
January 13, 2016

Certified by Signature redacted

Li-Huei Tsai, Ph.D.
Professor and Director – Picower Institute for Learning and Memory
Thesis Supervisor

Accepted by Signature redacted

Matthew A. Wilson, Ph.D.
Sherman Fairchild Professor of Neuroscience
Director of Graduate Education for Brain and Cognitive Sciences

Gamma frequency entrainment attenuates amyloid load and modifies microglia

by

Hannah Frances Iaccarino

Submitted to the Department of Brain and Cognitive Sciences on January 13, 2016
in Partial Fulfillment of the Requirements for the Degree of
Doctor of Philosophy in Neuroscience

Abstract

Gamma oscillations (20-50 Hz), a common local field potential signature in many brain regions, are generated by a resonant circuit between fast-spiking (FS)-parvalbumin (PV)-interneurons and pyramidal cells. Changes in gamma oscillations have been observed in several neurological disorders. However, the relationship between gamma oscillations and cellular pathologies of these disorders is unclear. Here, we investigated this relationship using the 5XFAD mouse model of Alzheimer's disease (AD) and found reduced behaviorally driven gamma activity before the onset of plaque formation or evidence of cognitive decline. Because of the early onset of gamma deficits, we aimed to determine if exogenous gamma manipulations could influence disease pathology progression. We discovered that optogenetically driving FS-PV-interneurons at gamma frequency (40 Hz) reduced levels of amyloid-β $(A\beta)_{1\text{-}40}$ and $A\beta_{1\text{-}42}$ isoforms in the hippocampus of 5XFAD mice. Neither driving FS-PV-interneurons at other frequencies, nor driving excitatory neurons, reduced Aβ levels. Furthermore, driving FS-PV-interneurons at 40 Hz reduced enlarged endosomes and amyloid precursor protein (APP) cleavage intermediates in hippocampus. Gene expression profiling revealed an induction of microglia specific genes associated with morphological transformation of microglia and increased Aβ phagocytosis by microglia. Inspired by these observations, we designed a non-invasive light-flickering paradigm that induced 40 Hz activity in visual cortex. The light-flickering paradigm profoundly reduced $A\beta_{1\text{-}40}$ and $A\beta_{1\text{-}42}$ levels in the visual cortex of pre-depositing mice and mitigated plaque load in aged, depositing mice. A $GABA_A$ antagonist completely blocked this effect; further evidence that GABAergic signaling is essential for this neuroprotective gamma activity. Finally, we showed that 40 Hz activity reduced tau phosphorylation in the TauP301S mouse model. Overall, our findings uncover a previously unappreciated function of the brain's gamma rhythms in neuroprotection by recruiting both neuronal and glial responses to mitigate AD-associated pathology.

Thesis supervisor: Li-Huei Tsai, Ph.D.
Title: Professor and Director – Picower Institute for Learning and Memory

Table of Contents

Acknowledgements

To Li-Huei, thank you. Words cannot express how much you have given me, how much I have learned, and how much I appreciate the gift and opportunity that was spending my graduate career in the Tsai lab. You are truly an inspiration. You are one of the hardest working women I know, and I will be forever grateful for your mentorship.

To my committee, Kay, Yingxi, and Chris, thank you for your support throughout my graduate career. You are incredible scientists and mentors, and I am so grateful for your guidance.

To Annabelle, you rock. None of this would be possible without you. You have inspired me as a scientist and a person. I will never forget our hours on end in the recording room together.

To the dweebs (Richard, Anthony, Fatema, Scarlett, Oleg, and Sara), thanks for keeping things weird.

To Ram, Jemmie, Omer, Jay, Adam, Yea-Jin, Alexi, and Marco, thanks for being smart scientists who taught me so much and also for being fun.

To Ying, thank you for being the best lab manager in the entire world, for expediting my orders when I needed you to, for the snacks I stole, for the tea, for the hugs, and for always hiding my water bottle before EHS inspections when I forgot to do it.

To Erica, thank you for taking such good care of my mouse colony and also for being a great friend.

To the Tsai lab, thank you for a glorious 4 years. We did this together.

To Andrii, Fan, Hans, Jinsoo, Chinna, Becky, Jennie, Emery, and Ed, thank you for your brilliant contributions to the manuscript.

To JP, thank you for being by my side always. Our friendship has helped carry me through so much, including this thesis project.

To Ty, can't wait to visit you in Denver. Thanks for the westerns and being the best boyfriend ever.

To Rachel, Nev, and Luna, thanks for being the best DC buds a girl could ask for. And Rach, thanks for loving my love of neuroscience. Dweeb for life.

To Dave, you made me love this stuff starting in Psych 006. Thanks for showing me the way.

This thesis is dedicated to Sophia, Margaret, Allie, Ann, Fran, Jack, and V. Thank you for being my family, for putting up with my weird, for inspiring me, and for always being there no matter what.

Chapter 1: Introduction

Alzheimer's disease

Over 5 million Americans currently suffer from Alzheimer's disease (AD). This progressive neurodegenerative disorder manifests as a severe loss of memory and executive function. It is the cause of 60-80% of all dementia. Two different types of AD have been defined. Approximately 1% of cases are the result of mutations of any of the three genes *APP, PSEN1,* and *PSEN2*, which contribute to the production and processing of amyloid precursor protein (APP). These patients can show symptoms as early as age 30, and therefore this form of the disorder is termed early-onset familial AD (FAD). All other cases with symptoms that emerge at age 65 or older likely arise from a combination of genetic and environmental mechanisms, which include age, cardiovascular health status, education, social and cognitive engagement, and traumatic brain injury. This late-onset AD (LOAD) affects over one third of Americans age 85 and older and is therefore a significant health risk for the American population.[1]

History: Alzheimer's disease was discovered in 1906 by a physician named Alois Alzheimer. His patient, a female adult named Auguste, suffered from severe memory loss and psychosis-like symptoms before her death. Because Dr. Alzheimer focused throughout his career on linking physical symptoms to molecular changes, he closely examined her brain tissue post-mortem to discover a novel pathology consisting of cell loss and abnormal deposits. It was not until years later in 1910 that his colleague Emil Kraepelin penned the name for the disease in the 8th edition of his book on psychiatry. Upon the founding of the Alzheimer's Association in 1980 by Jerome Stone and his family, financial support for research on AD increased significantly. In 1983, the United States Congress declared November National Alzheimer's Disease Month. With increased funding and public awareness, progress was made in the investigation of the

pathology and cause of the disease. In 1984, the protein thought to underlie AD pathogenesis, amyloid-β (Aβ), was discovered, and by 1986, the other prime suspect in AD, tau, was identified. Research and mechanistic understanding grew; various mouse models that replicate aspects of the disorder were created (**Table 1**).[2]

Genetics: Although the disease was discovered over a century ago, the battle to find a cure continues. The struggle to find a treatment for AD in spite of the significant time and resources already invested into a search for a cure over the past 30 years is in part because AD is a multifaceted disorder. First, most cases of AD are not fully explained by genetics, and the genetics of the disease alone are complex. Approximately 1% of cases are the result of fully penetrant mutations of any of the three genes *APP, PSEN1,* and *PSEN2*, which contribute to the production and processing of APP. APP is cleaved sequentially by β- and γ-secretases to form the toxic Aβ species implicated in AD. Alternative cleavage of APP by α-secretase leads to production of non-toxic sAPPα and α-C-terminal fragment of APP. Mutations in *APP, PSEN1,* and *PSEN2* shift APP processing to favor production of Aβ, likely causing the increased levels that eventually aggregate to form neuritic plaques in the brain. In fact, a total of 39 APP mutations have been discovered that promote production of the most toxic Aβ species, $A\beta_{1\text{-}42}$.[3] It is largely based on this genetic data from FAD that the amyloid hypothesis for AD was developed. This hypothesis states that disruptions in APP processing lead to the formation of amyloid plaques which have negative downstream effects on neurons, synapses, and immune cells of the brain and eventually cause neuronal dysfunction and loss in AD.[4] However, this hypothesis ignores many other contributing factors, including alternative genetic factors, in AD pathogenesis.

Table 1

Mouse model	Mutated gene	Aβ plaques	Hyperphosphorylated Tau	Neuronal loss	Synaptic loss	Primary reference
PDAPP	APP	Yes	Yes	No	Yes	Games et al. 1995
Tg2576	APP	Yes		No	No	Hsiao et al. 1996
TgCRND8	APP	Yes		No		Chishti et al. 2001
APP/PS1	APP, PS1	Yes				Holcomb et al. 1998
APP23	APP	Yes	Yes	Little	Yes	Struchler-Pierrat et al. 1997
Tg-SwDI	APP	Yes				Davis et al. 2004
APPDutch	APP	Low				Herzig et al. 2004
APPDutch/PS1	APP, PS1	Yes				Cheng et al. 2004
hAPP-Arc	APP	Yes				Lord et al. 2006
Tg-ArcSwe	APP	Yes				Knobloch et al. 2007
APPArc	APP	Yes				Ronnback et al. 2011
TAPP	APP, Tau	Yes				Lewis et al. 2001
3xTg-AD	APP, Tau, PS1	Yes	Yes		No	Oddo et al. 2003
APPSL/PS1	APP, PS1	Yes		Yes	Yes	Wirths et al. 2002
APP/PS1KI	APP, PS1	Yes		Yes	Yes	Casas et al. 2004
5XFAD	APP, PS1	Yes		Yes	Yes	Oakley et al. 2006
CK-p25	Cdk5	Yes	Yes	Yes	Yes	Cruz et al. 2003

Table 1: Table describing the various AD mouse models available. Blank cell indicates that no study has reported data for that mouse.

The strongest risk factor for both early- and late-onset AD is the *ε4* allele of *Apolipoprotein E*. Apolipoprotein E (ApoE) is a protein expressed in the liver, the brain, macrophages, and monocytes that mediates cholesterol metabolism. In humans, there are three different alleles of *APOE,* and the *ε4* allele markedly increases risk for AD. People carrying one copy of the *ε4* allele (heterozygotes) have a three-fold increased risk of developing AD, and *ε4* homozygotes have a fifteen-fold increased risk of developing AD. *APOE* is primarily expressed in astrocytes in the brain; the protein product has been shown to bind Aβ and mediate its entry into the bloodstream for clearance. It is hypothesized that the *ε4*-specific isoform mutation in the *APOE* gene causes impaired clearance and build up of Aβ.[5]

Recently 21 additional AD-related genetic loci were identified through genome-wide association studies (GWAS) and massive parallel sequencing (MPS) work, providing further insight into the mechanisms of the disease.[3] Although no single gene matches the risk incurred by the *APOE ε4* isoform, many important genetic factors were identified. *Clusterin (CLU)*, the first GWAS AD gene identified, mediates lipid transport and likely influences endocytosis-mediated Aβ clearance.[6] The second gene to show convincing association with AD by GWAS is *phosphatidylinositol-binding clathrin assembly protein (PICALM)*. Mechanistic studies showed that PICALM mediates migration of synaptic proteins to the synapse, and disruption of PICALM function caused by AD-associated single-nucleotide polymorphisms (SNPs) may contribute to the synaptic dysfunction and neuronal loss observed in AD.[6] Thus, it is clear from a wide body of genetic data that a broad and diverse array of genetic factors are sufficient to cause AD.

Pathology: The pathological complexity of the disease is best described in a recent review by Canter et al.[7] AD is histopathologically characterized by the aggregation of NFTs consisting of hyperphosphorylated tau protein and amyloid plaques composed of the Aβ peptide.

Additional neuronal changes caused by AD include enhanced DNA methylation and histone acetylation, impaired interneuron function, polymorphisms in *APOE* and related genes, synaptic loss, neurodegeneration and decreased functional connectivity.[7,8] In the earliest stages, AD manifests in the intracellular accumulation of pathogenic forms of tau bearing abnormal posttranslational modifications, such as phosphorylation and acetylation.[8–11] The accumulation begins in the parahippocampal circuit, including the hippocampus and layer II of the entorhinal cortex. As the disease progresses, tau accumulation extends systematically into the extrahippocampal space and finally into the neocortex. This progression correlates with cognitive decline in human AD patients. Amyloid pathology progresses from the entorhinal cortex throughout the cortex in a widespread manner.[12–14] The peptides ($A\beta_{1\text{-}40}$ and $A\beta_{1\text{-}42}$) that compose the plaques are 38-42 amino acid proteins whose normal physiological function remains unidentified. Aβ peptides are produced by the sequential proteolytic cleavage of APP by β- and γ-secretases.[15] Under normal conditions, soluble Aβ peptides are produced and secreted by neurons and subsequently cleared from the brain via cerebral spinal fluid (CSF) pathways.[16] In AD, Aβ aggregates into higher-order species to form soluble oligomers and insoluble plaques in a concentration-dependent manner. Although the interaction between tau and amyloid in AD has yet to be fully elucidated, there is a demonstrated interaction between the two pathologies. Toxic Aβ oligomers promote dendritic enrichment of abnormally modified tau, which leads to disrupted neurotransmission at the synapse.[17,18] Reciprocally, reduction of endogenous tau levels in transgenic mice carrying APP duplications prevents Aβ-induced synaptic loss and functional deficits. Therefore, Aβ may act upstream to promote pathogenesis; however, the toxic effects of Aβ pathology are hampered in the absence of tau, and the direction of the relationship between amyloid and tau remains unclear.[19]

One factor that links amyloid and tau pathology and drives AD pathogenesis is cycline-dependent kinase (Cdk5). Cdk5 is a proline-directed protein kinase that acts on serine and threonine residues and is physiologically activated by p35.[20] Cdk5 hyperactivation has been observed in various neurological disorders. This aberrant activity results from accumulation of a truncated form of p35. This truncated version, p25, causes more stable activation of Cdk5 with different subcellular localization. Interestingly, APP transgenic mice have increased Cdk5-mediated tau phosphorylation, and Cdk5 inhibition reduces Aβ-mediated neural toxicity *in vivo*.[21,22] Pioneering work from Cruz et al. showed that hyperactivation of Cdk5 by p25 caused formation of tau neurofibrillary tangles (NFTs) and neurodegeneration.[23] Taken together, these data suggest a role for Cdk5 in linking amyloid and tau pathology and directing phosphorylation of substrates involved in AD pathogenesis and neurodegeneration.

A wide body of literature points to another AD culprit: inflammation. Various studies showing changes in immune genes and pathways in the early stages of AD have prompted the hypothesis that inflammation is causative in AD and may exacerbate other aspects of AD pathology.[24] Microglia are the primary cell-type responsible for neuroinflammation in AD patients. Under normal conditions, microglia serve many important roles: assisting in synapse formation, phagocytosing of metabolic products and other toxins, and driving the ligand-mediated neuroprotective response after neural insults. However, aberrant activation of these cells has been linked to AD pathogenesis. Human patient genetic analysis has established a set of immune-related AD risk genes, including triggering receptor expressed on myeloid cells 2 (TREM2).[24] Animal studies have verified the role of several of these factors in AD pathogenesis. For example, in the 5XFAD mouse, a well-established AD mouse model, loss of TREM2 expression results in increases in hippocampal Aβ.[25] In short, there is a clear link between

microglia, inflammation, and AD; a therapy that can target immune-related pathways has potential to treat the disease.

Circuit dysfunction is tightly linked to AD pathophysiology

Despite debate over the precise molecular cascade that results in full blown cognitive dysfunction and neurodegeneration, aberrant neuronal activity and circuit dysfunction have clearly been shown to be a significant effect of AD pathogenesis. In 2012, Verret et al. demonstrated that AD pathology in a human APP (hAPP) mouse model does not simply silence neuronal activity, but rather disrupts rhythmic network activity in learning and memory circuits. Specifically, FS-PV-interneurons have reduced levels of voltage-gated sodium channels (VGSCs) that result in impaired gamma oscillations in these transgenic mice.[26] Cognitive function critically depends on the precise timing of oscillations in neural network activity, specifically in the gamma frequency.[27] Therefore, the disruption of gamma oscillatory activity in neural circuits compromised by neuropathology in AD may represent a key determinant of memory impairment in the disease. In addition, the spread of amyloid pathology follows a regular pathway defined by specific neural circuits. In human patients, plaque deposition begins in the neocortex in regions that constitute the default network. A vast body of literature has defined these areas as active when subjects are not engaged in a particular task and associated with thinking and "day dreaming."[28] Moreover, using an AD mouse model, Bero et al. demonstrated that there are a defined set of brain regions most vulnerable to amyloid aggregation and that these brain regions have the highest levels of endogenous brain activity.[29] Therefore, there is a clear association between specific neural circuits and amyloid pathology. Finally, the literature has firmly established that neuronal activity is a potent modulator of endogenous

concentrations of both Aβ and tau. A groundbreaking study demonstrated that pharmacological manipulation of synaptic activity *in vitro* modulates neuronal activity. Specifically, treatment of organotypic hippocampal slices prepared from transgenic mice overexpressing APP with tetrodotoxin decreased neuronal activity and subsequently Aβ levels. The opposite effect was observed upon treatment with picrotoxin.[30] Since this finding, the dynamic modulation of Aβ concentration and later plaque deposition by neuronal activity *in vivo* has been clearly demonstrated.[7] More recently, a clear relationship between levels of hyperphosphorylated tau and neuronal activity has been demonstrated.[31] Taken together, these data show a strong connection between circuits, activity, and AD pathology.

Oscillations are a fundamental property of neural circuits

A fundamental emergent property of neural circuits studied for almost a century is their oscillatory activity. Brain oscillations are recorded extracellularly and extracranially and reflect the summation of synaptic activity across many neurons. These rhythms are ubiquitous across brain regions, are preserved across species, and are tightly correlated with certain behaviors and brain states.[32] The rate of these oscillations ranges from infraslow (<0.01 Hz) to ultrafast (90 – 200 Hz) (**Table 2**).[33] There remains passionate debate in the field as to whether oscillations are simply a by-product of the faster synaptic activity produced by neurons or whether they represent something more, an emergent property of brain circuits critical to their function.[27] Those who study the role of oscillations in brain function cite their hierarchical, synchronous structure as a framework in which the brain can organize its activity on multiple timescales.[32]

Table 2

Class	Frequency (Hz)
Slow 4	15-40 s
Slow 3	5 - 15 s
Slow 2	2 - 5 s
Slow 1	0.7 - 2 s
Delta	1.5 - 4 Hz
Theta	4 - 12 Hz
Beta	12 - 20 Hz
Gamma	20 - 80 Hz
Fast/Sharp-wave ripple	80 - 200 Hz
Ultrafast	200 - 600 Hz

Table 2: Table describing name and frequency of recorded brain oscillations.[33]

Brain rhythms are well organized across species. All nervous systems favor rhythmic activation centered at particular frequencies. Excitatory pyramidal cells fire at random and at low frequencies. However, from Hebb's principle, it is known that "neurons that fire together, wire together."[34] This principle means that for connections between neurons to have relevance and maintain, there must be multiple simultaneous synaptic inputs on them. Oscillatory networks facilitate this process. In complex nervous system structures, such as the human brain, inhibitory interneuron microcircuits create oscillators that input on and create rhythm within a pyramidal cell network.[27] These networks drive pyramidal cell firing at various steady frequencies to create groups of neurons that fire in sync and therefore "wire together" in distinct function units, or circuits. In addition, Buzsáki points out that neural oscillators progress linearly on a logarithmic scale, which further supports their purposeful organization as part of brain function.[32] Moreover, distinct types of rhythms interact with and modulate each other, and this interaction is structured: slower oscillations control emergence and amplitude of faster rhythms.[35] Finally, oscillation patterns are preserved across all mammals despite the change in size and organization of the mammalian brain. The maintenance of these dynamic time clocks throughout evolution argues for their functional importance despite changes in brain structure and volume.[32] Taken together, these data demonstrate that oscillations are structured functional units fundamental to brain function.

In addition, neural oscillations are tightly linked to behavioral states. Theta oscillations (4-12 Hz) occur during two distinct periods: during active exploration and rapid eye movement (REM) sleep.[33] When rodents are quiescent, sharp-wave ripples (SWRs) (150-200 Hz) are observed. Gamma oscillations (20-50 Hz) in the hippocampus are present during distinct periods of activity in rodents: during running, when theta oscillations (4-12 Hz) are present, and during

quiescent and exploratory behavior, when sharp-wave ripples (SWRs) occur[36–38]. During sleep, delta rhythms (1.5 – 4 Hz) predominate.[32] This connection between behavioral states and neural oscillations is similar across rabbits, cats, mice, monkeys, rats, bats, and humans[33] and suggests that oscillations are a fundamental property of brain function.

Gamma oscillations as a potential therapeutic target

One type of oscillatory activity that the literature has demonstrated to be disrupted in neurological disease is gamma oscillations.[26,39] However, the interplay between pathology and this emergent circuit property has yet to be determined. Important to understanding how gamma and pathology interact is to know what mechanisms underlie gamma oscillations in the normally functioning, healthy brain. Despite rhythms of the brain having been a prominently studied area of neuroscience for almost 100 years, the cellular mechanisms that support and define them are not fully understood.[27] However, gamma oscillations are a well-defined frequency band of oscillations mechanistically. Activation of local circuits of excitatory and fast-spiking inhibitory neurons that resonate at 20-50 Hz gives rise to oscillations in the local field potential (LFP), called gamma oscillations.[40–42] Knowledge of the cellular origins of the gamma rhythm has allowed for disruption of these mechanisms to find a causative role for gamma in proper neuronal function and behavior. In 2009, Cardin et al. showed that gamma synchrony supports sensory processing.[42] Furthermore, driving gamma with optogenetic techniques to specifically target FS-PV-interneurons improved neuronal signaling via increased spike synchrony.[43] Given the importance of gamma in regulating spike timing as well as the role of spike timing and synchrony in learning and memory formation, it is hypothesized that gamma oscillations play a fundamental role in cognition.[44]

There is converging evidence of gamma deficits in different mouse models of AD (hAPP and apoE4),[26,45] and reports that gamma is altered in humans with AD.[46] By seeking converging evidence from multiple mouse models of AD, including transgenic and knock-in models, we can be assured that these results are not due solely to overexpression of transgenes or to other side effects particular to one model. That said, we do not know the cause of gamma deficits in the AD models or in humans with AD: these deficits could arise from elevated Aβ, APP overexpression, or other causes. One potential molecular deficit in humans that has been linked to gamma deficits is reduced levels of VGSC subunit Nav1.1, an interneuron specific subunit that is predominantly expressed in PV cells. Verret et al. have found reduced Nav1.1 levels in humans and in the hAPP mouse model of AD, and they have shown that increasing Nav1.1 levels in the hAPP mouse model rescues gamma deficits found in these mice.[26] Because gamma rhythms are disrupted in AD, gamma recruits synaptic activity in local circuits, and changes in synaptic activity can alter AD molecular pathology, it will be important to determine how gamma oscillations might affect cellular and molecular pathology in a mouse model of AD. Understanding how gamma may affect disease pathogenesis has important implications for elucidating both the basic pathology of and possible therapeutic interventions for the many neurological diseases with altered gamma activity.

Microglia

The interaction between Aβ and neuronal activity was discussed above as a potential mechanism in disease pathogenesis and also therapy design. Another way in which neuronal activity can affect AD pathology is through communication between neurons and microglia.

Microglia are the brain's resident immune cells. As mononuclear phagocytes, they play critical roles in brain homeostasis, development, and disease.[47]

As the brain's primary defense system, microglia possess transcriptional programming that allows them to respond to changes in the neural environment. Resting microglia have a distinct morphology defined by a small cell body and highly motile, long processes.[25] When microglia detect injury signals, such as sharp increases in extracellular calcium, they react by shrinking in their processes and expanding their cell bodies into a so-called "activated" state.[25] Recent evidence has shown that there are many, diverse microglia activation states, and two have been well defined: M1 and M2. The M1 state is defined as the pro-inflammatory state. This type of activation induces microglia to decrease production of neurotrophic factors, secrete pro-inflammatory cytokines and chemokines, and produce reactive oxygen species. Persistent activation of M1-like microglia causes chronic brain inflammation and neuronal dysfunction.[48] Contrastingly, M2 microglia increase secretion of neurotrophic factors, produce proteases to inactivate toxins, and engage in phagocytic activities. Therefore, the M2 state is associated with clearance of debris, decreased inflammation, and limited neuronal damage.[48]

An alternative pathway of microglial activation has recently been demonstrated to promote neuronal health in response to brain injury. Treatment of microglia with macrophage colony-stimulating factor (MCSF) promotes phagocytosis and cytokine production. MCSF treatment suppresses certain inflammatory immune activities by modulating Toll-like receptors (TLRs). Modulation of TLRs by MCSF dampens the inflammatory reaction of microglia but continues to promote non-inflammatory cytokine production.[49] Interestingly, activation of this microglia response has been demonstrated to be highly therapeutic in Alzheimer's disease. Microglia with increased MCSF receptors (CSF-1Rs) more aggressively surround Aβ plaques.[50]

In addition, a recent study showed that treatment of microglia with MCSF increased engulfment of Aβ.[51] Because microglia are very sensitive to the neural environment, can respond to the presence of Aβ, and display phagocytic activity under certain activation states, it will be important to determine how altering microglia in an AD mouse model might affect cellular and molecular pathology. Understanding how microglia may affect disease pathogenesis has important implications for elucidating both the basic pathology of and possible therapeutic interventions.

Current state of AD therapeutics

FDA approved drugs: Currently, five drugs are approved by the FDA for the treatment of AD. These include donepezil (brand name Aricept), galantamine (brand name Razadyne), memantine (brand name Namenda), rivastigmine (brand name Exelon), and donepezil/memantine (brand name Namazaric). Donepezil, galantamine, and rivastigmine are acetylcholinesteraste inhibitors (AChEIs), which act at the synapse to prevent reuptake of acetylcholine (ACh) and maintain levels of ACh at the synapse. A leading hypothesis in the field for many years was the cholinergic hypothesis. During AD, neuronal transmission in the hippocampus and cortex is compromised due to loss of cholinergic neurons in the nucleus basalis of Myenert that input onto those areas[52]. It was hypothesized that restoration of normal ACh levels would promote cholinergic transmission in the hippocampus and cortex and have beneficial effects on cognition to compensate for the loss of cholinergic neurons. Unfortunately, donepezil and other AChEIs are not an effective treatment for AD; although they delay symptom progression temporarily, they have no lasting effect on pathology or neurodegeneration[53].

Another FDA approved drug, memantine, acts as an N-methyl-D-aspartate receptor (NMDAR) antagonist. Interestingly, it was first synthesized by Eli Lilly to treat diabetes and later repurposed as an AD drug.[53] During AD, as neurons begin to die, they release excess glutamate, which causes excitotoxicity in the remaining healthy cells, accelerating neurodegeneration. Memantine acts by blocking binding of glutamate to NMDARs to counteract the high levels of glutamatergic transmission. As with the AChEIs, memantine is mildly effective at slowing symptom development in mild-to-moderate AD but has no lasting effect on pathology or learning and memory impairment.[7]

The amyloid cascade hypothesis: A long-standing hypothesis about the pathogenesis of AD is that the accumulation of the Aβ peptide and its subsequent aggregation into senile plaques is a primary event in the progression of AD that leads to neurotoxicity, inflammation, tau pathology, and neurodegeneration.[15] Strong evidence for the role of Aβ in AD comes from genetic studies. 1% of AD cases are the result of fully penetrant mutations of any of the three genes *APP, PSEN1,* and *PSEN2*. These mutations shift APP processing to favor production of Aβ, likely causing the increased levels that eventually aggregate to form neuritic plaques in the brain. In addition, Aβ has various detrimental effects on neurons. Neurons treated with Aβ *in vitro* have increased DNA damage and apopotosis and display higher levels of synaptic depression.[7] Therefore, many therapies have been developed to target Aβ in an attempt to ameliorate its effects on neurons and repair damage caused by AD.

Indeed, anti-amyloid strategies have been the focus of the pharmaceutical industry for the past two decades. β-secretase is the first enzyme to cleave APP in the sequential process that produces Aβ. Inhibitors of this enzyme, which include E2609, MK-8931, and LY2886721, showed promising results in clinical trials.[53] However, β-secretase cleaves a diverse subset of

substrates required for proper brain function. Quantitative proteomics revealed that the enzyme targets various cell-surface signaling molecules including neuregulin-1, which is important for myelination and synaptic plasticity.[54] Therefore, although β-secretase inhibition is a promising strategy, the wide range of potential side effects may outweigh its Aβ-reducing effects.

Cleavage of APP by γ-secretase is the final step in production of $A\beta_{1-40}$ and $A\beta_{1-42}$. Therefore, reducing the activity of this enzyme has the potential to reduce Aβ.[55–57] Inhibition of γ-secretase, like β-secretase, can have disastrous secondary effects. In particular, one target of γ-secretase is Notch, which is a signaling protein critical for cell division and proliferation as well as development. The recently completed Eli Lilly trial was evidence of the risk of secondary effects: treatment with semagacestat (LY450139) increased cognitive deficits in AD patients and further impaired their ability to perform activities required for daily life.[57] Another γ-secretase inhibitor (avagecestat) trial was halted because the treatment was ineffective at reducing pathology and cognitive deficits.[58]

A more recent strategy that targets the Aβ peptide is anti-amyloid immunotherapy. Previous studies using animal models of AD have shown that passive immunization targeting Aβ is effective at reducing pathology and behavioral deficits. Recently, however, two monoclonal Aβ antibodies, bapineuzumab and solanezumab, failed phase III clinical trials.[53] Bapineuzumab showed promise because CSF Aβ and tau levels were reduced, but no change in cognitive symptoms was observed.[53] Solanezumab also did not significantly affect cognition in mild-to-moderate AD patients.[53] In a recent study, Busche et al. showed that anti-amyloid antibodies increased Ca^{2+} signaling measured by two-photon microscopy in the PDAPP mouse model, which indicates that although passive immunization improves Aβ-associated pathology, it simultaneously exacerbates neuronal hyperexcitation and chronic hyperactivity responsible for

cognitive deficits in AD.[59] Taken together, these data suggest that therapies targeting Aβ alone are insufficient at treating AD and even have dangerous side effects.

Tau-related therapies: In the earliest stages, AD manifests in the intracellular accumulation of pathogenic forms of tau bearing abnormal posttranslational modifications, such as phosphorylation and acetylation.[8–11] These modifications lead to the formation of insoluble paired helical fragments (PHFs) and neurofibrillary tangles (NFTs). Because tau normally acts as a microtubule stabilizing molecule, its aggregation leads to inactivation and subsequent microtubule destabilization and neurodegeneration. Although tau is phosphorylated under physiological conditions, in AD tau is hyperphosphorylated and unable to perform its normal functions. Proteins known to promote tau phosphorylation include microtubule affinity regulatory kinase (MARK), mitogen-activated protein kinase (MAPK), protein kinase C (PKC), cyclin-dependent kinase 5 (CdK5) and glycogen synthase kinase 3β (GSK3β). Various inhibitors of these kinases are being developed to target tau to treat AD.[60] Two phosphatases are known to modify tau, protein phosphatase 1 (PP1) and 2A (PP2A). Upregulating the activity of these proteins is another therapeutic strategy. Sodium selenate (VEL015) is a PP2A agonist currently in clinical trial phase II.[53] The caveats for these strategies are similar to those for anti-amyloid approaches. Tau is a critical protein needed to stabilize microtubules and maintain neuronal health, and tampering with its phosphorylation levels may have detrimental effects on its endogenous activity.

Other strategies against tau include anti-aggregation drugs and anti-tau immunotherapy. Methylene blue showed promise in disrupting tau aggregates and several clinical trials are ongoing to test its ability to treat AD. Recently, a study in rodents showed that treatment with anti-hyperphosphorylated tau antibodies reduced cognitive deficits in tau mouse model.[61]

Clinical trials will reveal whether targeting these pathological forms of tau can improve AD symptoms without causing adverse secondary effects.

ApoE-related therapies: APOE is the strongest genetic risk factor for both early- and late-onset AD. The frequency of AD is 91% among people carrying two copies of the *ε4* allele. The average age of AD onset is 68 years for *ε4* homozygotes compared to 84 years in *ε4* noncarriers.[62] In addition, more amyloid plaque deposits are present in *ε4* carriers compared to noncarriers.[62] Interestingly, overall Aβ levels and plaque load are ApoE-isoform dependent (*ε2* < *ε3* < *ε4*), implicating ApoE in Aβ metabolism and clearance and leading to the hypothesis that *ε2* is protective against AD.[63] Moreover, recent evidence suggests a role for ApoE in synaptic function. For example, in mice expressing human *APOE ε4* (ApoE4-TR), spine density is decreased compared to *APOE ε3* (ApoE3- TR) control mice.[64] Given the growing evidence that ApoE plays a critical role in AD pathogenesis, recent efforts have targeted ApoE for therapeutic purposes. Liver X receptor (LXR) and retinoid X receptor (RXR) stimulation triggers ApoE expression. Therefore, drugs that activate these receptors, such as LXR agonist TO901317, are being developed to treat AD.[65] However, given the complex relationship between *APOE* isoform and AD pathogenesis, a general modulator of ApoE may have deleterious effects. ApoE4 is structurally different than ApoE2 and ApoE3, and these structural characteristics may contribute to its toxic effects. Therefore, substances that modify the structure of ApoE4 and make it more ApoE2- or ApoE3-like may be successful at ameliorating AD pathology. Two candidates are GIND-25 (disulphonate) and GIND-105 (monosulphoalkyl), which disrupt the N- and C-terminal domain interactions in ApoE4 and reduce Aβ.[63] CB9032258 disrupts the structure of ApoE4 and reverses synaptic deficits caused by ApoE4 in neurons.[66] Finally, ApoE receptors, low-density lipoprotein receptor-related protein 1 (LRP1) and low-density lipoprotein receptor

(LDLR), may be additional therapeutic targets. Modulation of their levels and binding efficacy to ApoE may be a method by which ApoE-mediated Aβ clearance is regulated.[63] ApoE is a promising therapeutic target; however, because of the complex relationship between ApoE, normal brain function, and Aβ pathology, one must be careful of aversive secondary effects.

Anti-inflammatory strategies: As described above, neuroflammation is strongly associated with AD pathology. The large body of evidence has even motivated the hypothesis that inflammation is causative in AD. These recent developments make the prospect of targeting inflammation as a therapeutic option enticing, but success has not yet been achieved. A recent clinical trial with the anti-inflammatory drug entanercept, which is an antagonist of TNF-α, failed to improve cognitive performance and increased the rate of infection in AD patients.[67] Given the complexity of the role of immune cells and immune signaling in the brain, it is likely that multiple aspects of the neuroimmune system must be modulated to significantly alter AD pathogenesis without negative side effects.

Currently, the AD therapeutics field has many promising routes to discovery of prevention, treatment, and even a cure for AD. Because many factors affect AD pathology, it is likely that modulation of multiple, diverse proteins and pathways will be required to treat AD. It will be especially important to focus on the development of therapies that disrupt pathogenesis and leave normal physiological functions intact.

Summary of the thesis

In the current study, we uncover a previously unknown dramatic effect of brain gamma oscillations on ameliorating Alzheimer's disease-associated pathology. We show that optogenetic induction of 40 Hz gamma activity results in a strong decrease of $A\beta_{1-40}$ and $A\beta_{1-42}$

levels in the hippocampus of a familial AD mouse model, 5XFAD. This effect is likely to be mediated by reduced BACE1-dependent APP cleavage, as we discovered that gamma oscillations decreased the amount of APP cleavage intermediates as well as enlarged endosomes in the hippocampus of 5XFAD mice. We also discovered that gamma stimulation produces a distinct brain microglia response, characterized by increased expression of genes responsible for microglia activation and phagocytic transformation.

In addition to employing optogenetic techniques, we designed a non-invasive method to induce gamma activity. We showed that light flicker at 40 Hz could produce gamma oscillations in the mouse visual cortex. We also found that, similar to optogenetic induction, this non-invasive procedure caused a decrease of Aβ in 5XFAD mice as well as plaque load in the visual cortex in older animals. Moreover, by applying this technique we were able to significantly reduce levels of another AD-related pathogenic marker, phosphorylated tau, in a commonly used tauopathy mouse model, TauP301S.

The novelty of this study is several fold. First, we made the unexpected observation that driving gamma oscillations reduced amyloid abundance and phosphorylation of tau. Second, we found that gamma oscillations not only influence neurons, but other cell types in the brain, including microglia. Indeed, microglia underwent morphological transformation and showed increased phagocytosis of Aβ. Third, we used a completely non-invasive sensory stimulation to induce gamma oscillations and demonstrated similar beneficial effects in the corresponding brain regions.

In summary, the findings reported in this thesis not only establish previously unknown functional connections between brain gamma oscillations, microglia function, and AD-related

pathology, but also demonstrate a proof of principle of a completely novel approach to treating AD, which may have revolutionary clinical implications for this devastating disease.

Role of the thesis

Novel prevention and treatment strategies for AD are needed: AD is the most common cause of dementia and the sixth leading cause of death in the United States. AD is a progressive neurodegenerative disorder that manifests in severe loss of memory and executive function. The most recent report from the Alzheimer's Association states that 1 in 9 people 65 and older (11%) and 1 in 3 people 85 and older (33%) has AD. Moreover, the prevalence of the disease is estimated to increase by 40% in the next ten years due to the aging American population combined with social, medical, and environmental improvements.[4] AD has a massive financial impact on patients and caregivers. Recent analysis done by the Alzheimer's Association showed that the cost of care for AD patients in the US totaled $221.3 billion. Moreover, 28% of caregivers of AD patients eat less than other adults in order to afford care. An estimated $15,000 of annual income per household is lost due to decreased work hours in order to care for an AD patient. In 2016, Americans spent $236 billion on AD, and will spend approximately $1.1 trillion in the year 2050 given the increased patient population. Finally, AD is the only disease in the top ten causes of death in the United States that cannot be cured, slowed, or prevented even though it was first identified over 100 years ago. Therefore, further research is fundamental to understanding the mechanisms that drive AD progression and developing novel therapeutic strategies to dampen the impact of this devastating disease.[68]

The study takes a composite approach towards understanding AD pathology: AD is a complex neurological disorder with a multifaceted pathological phenotype. The disease is

histopathologically characterized by the accumulation of amyloid plaques composed of the Aβ peptide and NFTs composed of the tau protein. Additional neural changes caused by AD include enhanced DNA methylation and histone acetylation, impaired interneuron function, polymorphisms in *APOE* and related genes, synaptic loss, inflammation, neurodegeneration and decreased functional connectivity.[7,8] Despite the diversity of symptoms that ultimately result in impaired cognition and death, current treatment strategies have singular targets.[7] For example, several therapeutics have been developed to affect either Aβ, such as active immunization to clear plaques, or tau, such as phenothiazine methylene blue to reduce insoluble tau, but not both. These single-molecule treatment methods have been determined either to be unsafe or have little to no clinical benefit.[7,9-11] Therefore, novel treatment strategies aimed at the many levels of AD pathology are needed. This study targets circuit level function by activating FS-PV-interneuron driven gamma oscillations and measure outcomes at the genetic, molecular, and cellular levels.

Chapter 2: Gamma is disrupted in 5XFAD mice early in disease and optogenetic gamma stimulation reduces Aβ levels

Gamma is decreased during hippocampal sharp wave ripples in 5XFAD mice early in disease

Altered gamma has been observed in multiple brain regions in several neurological and psychiatric disorders, including a reduction in spontaneous gamma synchronization in AD patients and reduced gamma power in multiple AD mouse models.[26,39,45,46] However, it is unclear if gamma is altered in other mouse models of AD, if it occurs early in disease progression, and if gamma affects disease pathology. Accordingly, we recorded neural activity from behaving 5XFAD mice, a well-established model of Alzheimer's disease.[69] In 3-month-old mice, which have elevated levels of Aβ but no major plaque accumulation in the hippocampus or manifestation of learning and memory deficits,[69] we recorded neural activity from hippocampal subregion CA1, where gamma has been particularly well characterized (e.g.[27,44,70,71]), using a virtual environment (**Ext. Data Fig. 1a**). In CA1, gamma is present during distinct periods of activity: running, when theta oscillations (4-12 Hz) occur (**Ext. Data Fig. 1b,** *left*), and quiescent behavior, when sharp-wave ripples (SWR) occur[37,38] (**Ext. Data Fig. 1b,** *right*). We found no clear differences in slow gamma power (20 to 50 Hz) between 5XFAD mice and wild-type (WT) littermates during theta (**Ext. Data Fig. 1c, d**).

We next examined gamma during SWRs, high frequency oscillations of 150-250 Hz lasting around 50-100 ms (**Ext. Data Fig. 1b, e**).[44] Prior work has shown that slow gamma is elevated during SWRs and increased gamma synchrony across CA3 and CA1 during SWR correlates with more coordinated firing between neurons.[38] Similarly, we found increased gamma power during SWRs (**Fig. 1da** yellow arrow indicates elevated gamma, **Ext. Data Fig. 1e**). The instantaneous frequencies of these slower oscillations (10-50 Hz, Methods) were a unimodal

Figure 1

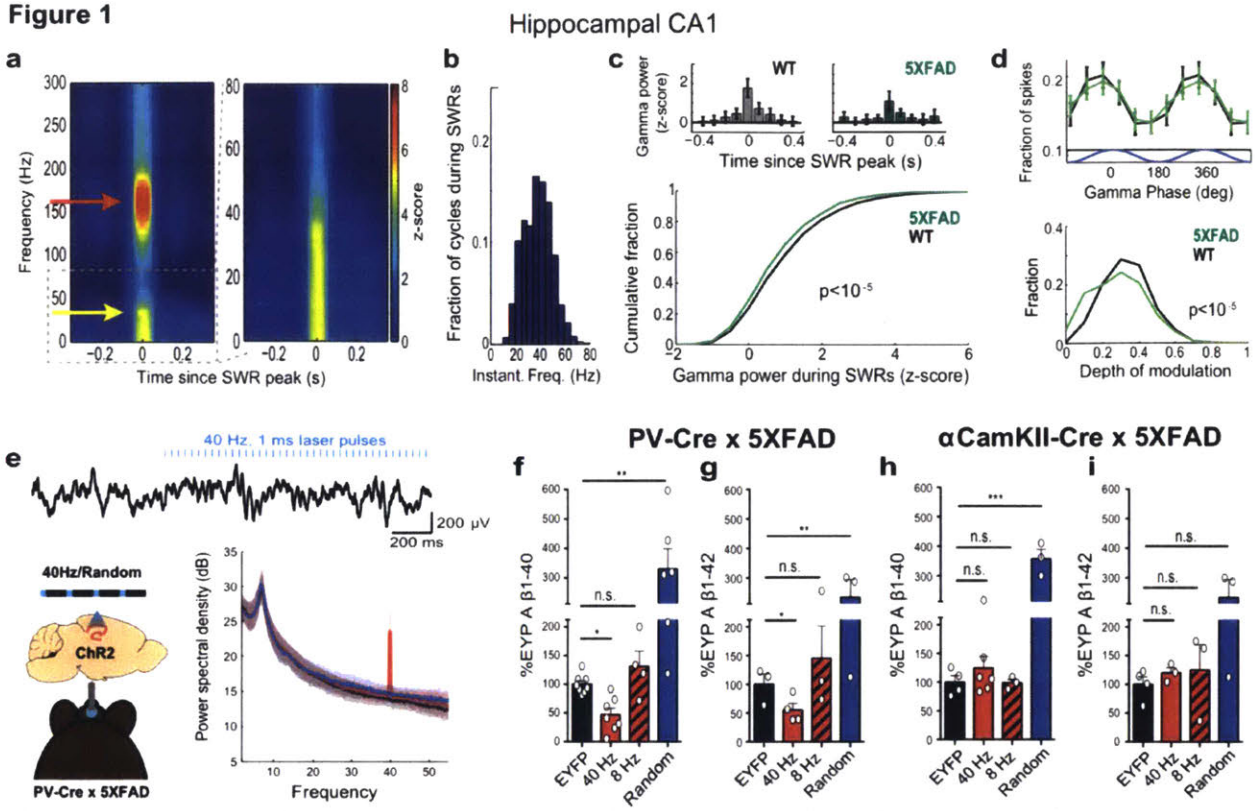

Figure 1: 5XFAD mice have reduced power in gamma during hippocampal SWRs

a) Average SWR-triggered spectrograms for one mouse (left) showing gamma (yellow arrow) during SWRs (red arrow); *right:* frequencies below 80 Hz enlarged (n=370 SWRs).

b) Histogram of instantaneous gamma frequencies during SWRs for mouse in ***a***.

c) *Above:* Z-scored gamma power around SWR peak for one WT and one 5XFAD mouse (mean ± SEM).

Below: Cumulative distribution of gamma power during SWRs (ranksum test, n=2166 and 3085 SWRs in 6 5XFAD and WT mice, respectively).

d) *Above:* Fraction of spikes during SWRs as a function of gamma phase (mean ± SEM).

Below: Depth of gamma spiking modulation during SWRs. (ranksum test, bootstrap resampling, n=2500 5XFAD and 3000 WT phase distributions).

e) *Above:* Local field potential trace before and during 40 Hz optogenetic stimulation. *Below:* Mean and standard deviation of power spectral density (n=4 5XFAD and 3 WT mice).

f) Relative $A\beta_{1-40}$ levels in CA1 of 5XFAD/PV-Cre mice in each stimulation condition normalized to EYFP controls (n=8 EYFP, n=7 40 Hz, n=4 8 Hz n=6 random mice).

g) As in ***f*** for $A\beta_{1-42}$ (n=4 EYFP, n=4 40 Hz, n=3 8 Hz n=3 random mice).

h) Relative $A\beta_{1-40}$ levels in CA1 of 5XFAD/αCamKII-Cre mice in each stimulation condition normalized to EYFP controls (n=6 40 Hz, n=3 8 Hz n=3 random mice).

i) As in ***h*** for $A\beta_{1-42}$ (n=3 mice per group).

n.s. not significant, * $p<0.05$, ** $p<0.01$, *** $p<0.001$ by one-way ANOVA; circles indicate n, mean + SEM in bar graphs unless otherwise specified.

Extended Data Figure 1

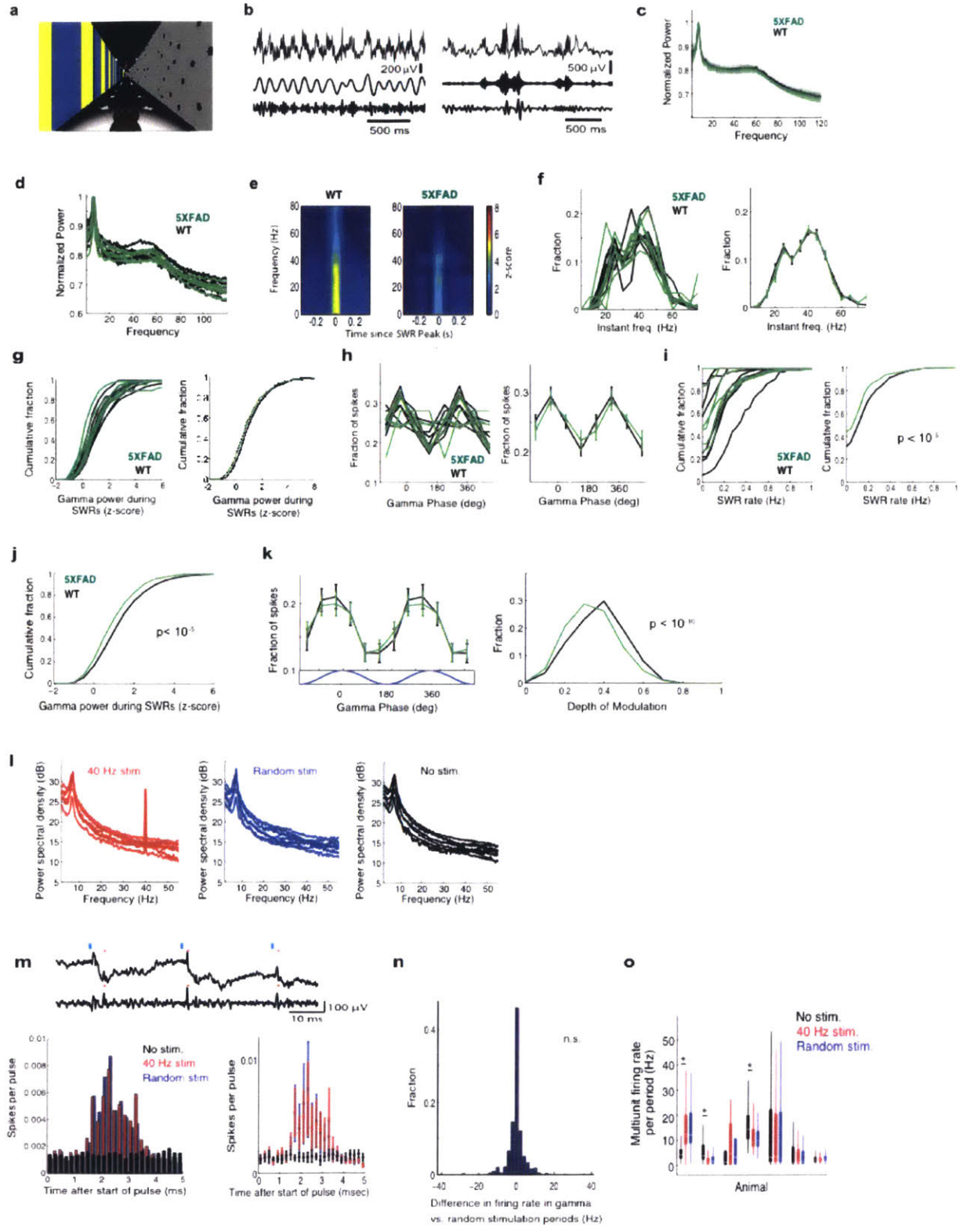

Extended Data Figure 1: 5XFAD mice have reduced power in gamma during hippocampal SWRs

a) Mouse in virtual reality environment.

b) Local field potential recorded in CA1, above, filtered for theta (left) or sharp wave ripples (right), middle, and gamma, below.

c) Mean and standard deviation of the normalized power spectrum during theta. Each animal's power spectral density was normalized to its peak (n=6 mice per group).

d) Normalized power spectral densities during theta periods in 3-month-old 5XFAD (green, n=6 mice) and WT (black/grey, n=6 mice) mice. Each animal's power spectral density was normalized to its peak (in theta).

e) Average SWR-triggered spectrograms for one WT and one 5XFAD mouse shows an increase in the gamma band during SWRs. This increase is lower in the 5XFAD mouse than in the WT mouse (n=370 and 514 SWRs in WT and 5XFAD, respectively; WT mouse shown here is the same as in **Fig. 1*a***).

f) Distributions for each recording (left) and the mean and standard error across sessions (right) of instantaneous gamma frequencies during SWRs in 5XFAD (green) and WT (black) mice show distributions around 40 Hz (n=820, 800, 679, 38, 1875, 57 gamma cycles per session in 6 5XFAD animals and 181, 1075, 919, 1622, 51, 1860, 1903 gamma cycles per session in 6 WT animals).

g) Cumulative distribution of the Z-scored gamma power during the 100 ms around the peak of the SWR for WT (black) and 5XFAD animals (green) for each animal (left) and the mean and standard error (shaded) across animals (right) (n=514, 358, 430, 22, 805, 37

SWRs per session in 6 5XFAD animals and 82, 311, 370, 776, 18, 710, 818 SWRs per session in 6 WT animals)

h) Fraction of spikes in CA1 during SWRs as a function of the phase of gamma in 5XFAD (green) and WT (black) mice for each animal (left) and the mean and standard error across animals (right, n=2475, 1060, 3092, 25, 6521, 123 spikes during SWRs per session in 6 5XFAD mice and 360, 4741, 1564, 2961, 88, 3058, 4270 spikes during SWRs per session in 6 WT mice).

i) SWR rate per non-theta period in 5XFAD (green) and WT (black) mice for each animal (left) and all animals combined (right, ranksum test, $p < 10^{-10}$, n=117, 210, 151, 55, 100, 1 non-theta periods per session in 6 5XFAD mice and 80, 68, 115, 95, 15, 159, 218 non-theta periods per session in 6 WT mice).

j) The cumulative distribution of gamma power during large SWRs (detection threshold greater than 6 standard deviations above the mean, Methods) shows significantly smaller increases in 5XFAD (green) than WT (black) mice (ranksum test, $p<10^{-5}$, n=1000 SWRs in 6 5XFAD mice and 1467 SWRs in 6 WT mice).

k) Fraction of spikes as a function of the phase of gamma during large SWRs (detection threshold greater than 6 standard deviations above the mean, Methods), mean ± SEM (left) and histogram of the depth of modulation of spiking (right) as a function of gamma phase in 3-month-old 5XFAD (green, n=6 mice) and WT (black, n=6 mice) mice (ranksum test, bootstrap resampling $p < 10^{-10}$, n=2500 5XFAD spike-gamma phase distributions and 3000 WT distributions).

l) Power spectral density during 40 Hz stimulation (red, left), random stimulation (blue, center), or no stimulation (black, right) of FS-PV-interneurons in CA1 for each mouse

(n=4 5XFAD mice with 169, 130, 240, 73 40 Hz, 143, 129, 150, 72 random, and 278, 380, 52, 215 no stimulation periods per animal and n=3 WT mice with 65, 93, 91 40 Hz, 64, 93, 90 random, and 187, 276, 270 no stimulation periods per animal).

m) *Above*: Example raw LFP trace (above) and the trace filtered for spikes (300-6000 Hz, below), with spikes indicated with red stars after optogenetic stimulation (blue vertical lines). *Below*: histogram of spikes per pulse after the onset of the 1 ms laser pulse during 40 Hz stimulation (red), random stimulation (blue), or no stimulation (black, n=345762 40 Hz, 301559 random pulses, and 32350 randomly selected no stimulation times at least 500 ms apart from 552 40 Hz, 543 random, and 1681 no stimulation periods in 4 5XFAD and 3 WT mice).

n) Histogram of the difference in firing rates between 40 Hz stimulation and random stimulation periods shows that both types of stimulation elicit similar amounts of spiking activity (Wilcoxon signed rank test for zero median, $p>0.6$, n=538 stimulation periods from 4 5XFAD and 3 WT mice, n.s. indicates not significant).

o) Multiunit firing rates per 40 Hz stimulation (red), random stimulation (blue), and no stimulation (black) period for each animal. Box and whisker plots show median (white lines in box) and quartiles (top and bottom of box). In all animals firing rates between 40 Hz and random stimulation were not significantly different, showing that the random stimulation condition serves as a control for spiking activity (ranksum tests for each animal, 3 WT and 4 5XFAD mice, p's>0.09,, n=87, 130, 8, 65, 93, 91, 73 40 Hz stimulation periods and 85, 129, 5, 64, 93, 90, 72 random stimulation periods per animal). We also examined whether 40 Hz stimulation caused neuronal hyperactivity relative to no stimulation, because according to a recent report, this could have negative effects on

neural circuit function.[26] In most animals the firing rates between 40 Hz or random stimulation and no stimulation were not significantly different (ranksum tests for each animal, 2 WT and 2 5XFAD, p's>0.25, n=8, 93, 91, 73 40 Hz stimulation periods and 15, 277, 270, 215 baseline periods per animal) or the firing rates during 40 Hz or random stimulation were lower than during no stimulation (ranksum tests for each animal, 1 WT and 1 5XFAD, p's<10^{-5}, which is significant when corrected for performing multiple comparisons, n=130, 65 40 Hz stimulation periods and 379, 187 baseline periods per animal) indicating that 40 Hz stimulation did not cause neuronal hyperactivity. In one animal there was significantly more activity with 40 Hz or random stimulation than during baseline (ranksum test for 1 5XFAD, mouse, p<10^{-5}, n=87 40 Hz stimulation periods and 251 baseline periods per animal). Therefore in six out of seven animals we see no evidence that the 40 Hz optogenetic stimulation of FS-PV-interneurons causes hyperactivity.

distribution centered around 40 Hz (**Fig. 1b, Ext. Data Fig. 1f**). Comparing gamma during SWRs in WT and 5XFAD littermates, we found that gamma power was significantly lower in 5XFAD than in WT mice (Methods, **Fig. 1c, Ext. Data Fig. 1g, j**; examples in **Fig. 1c,** *top*). Spiking was phase modulated by gamma in both groups, although the depth of modulation was significantly smaller in 5XFAD than in WT animals (**Fig. 1d, Ext. Data Fig. 1h, k**). Furthermore, there were fewer SWRs per time in non-theta periods in 5XFAD mice compared to WT (**Ext. Data Fig. 1i**), reducing periods when gamma power is elevated (**Fig. 1a,c, Ext. Data Fig. 1e**). These results reveal deficits in gamma modulation of CA1 spiking in a mouse model of AD prior to the development of major amyloid plaque accumulation or evidence of cognitive impairment. This deficit in gamma converges with evidence of gamma deficits in different mouse models of AD, and reports that gamma is altered in humans with AD.[26,45,46] Indeed, molecular deficits in Nav1.1 in humans have been linked with gamma deficits in hAPP mice.[26]

Gamma stimulation reduced Aβ production in hippocampal CA1

These gamma deficits during SWRs early in disease progression in this mouse model of AD prompt the question of whether gamma could affect molecular and cellular AD pathophysiology. To test this, we induced gamma optogenetically in 5XFAD/PV-Cre mice (Methods, **Fig. 1e,** *left,* **Ext. Data Fig. 2a, b, c**). We chose to drive FS-PV-interneurons at 40 Hz because we found deficits in gamma during SWRs, and instantaneous gamma frequencies during SWRs were centered around 40 Hz. Delivering 1 ms 473 nm light pulses at 40 Hz resulted in increased power at 40 Hz in LFPs in CA1, while random stimulation did not (**Fig. 1e, Ext. Data Fig. 1l**). Both resulted in similar firing rates (**Ext. Data Fig. 1m, n, o**).

Extended Data Figure 2

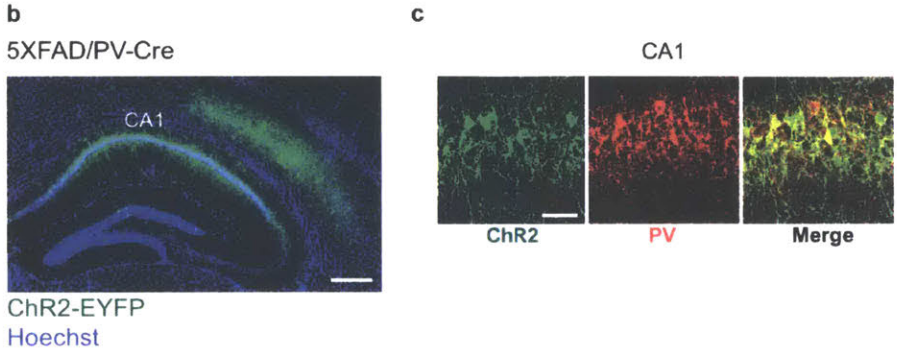

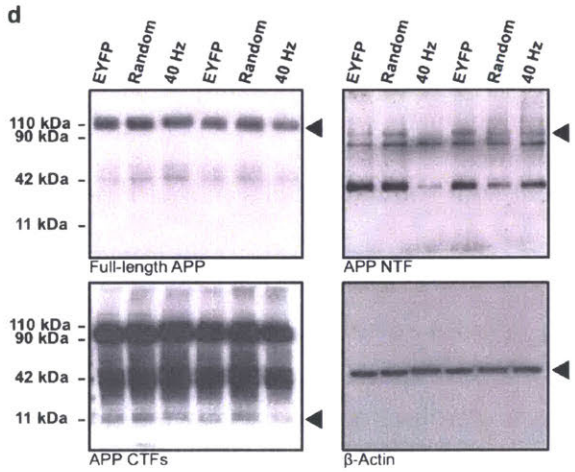

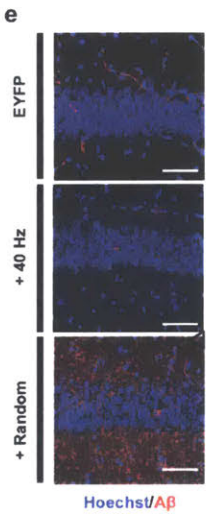

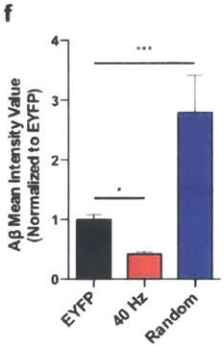

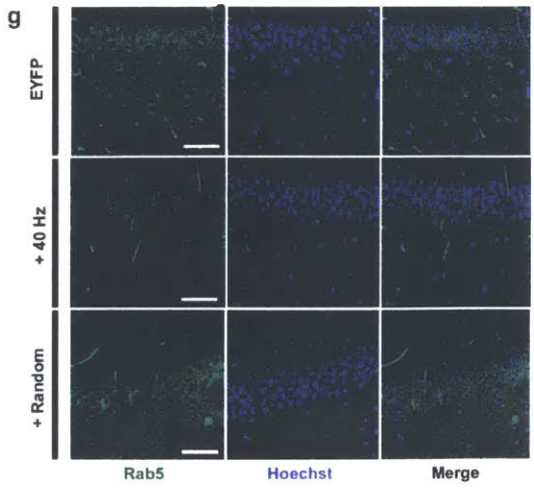

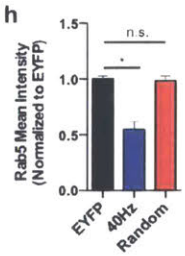

Extended Data Figure 2: ChR2 was expressed in FS-PV-interneurons for optogenetic stimulation

a) AAV-DIO-ChR2-EYFP or AAV-DIO-EYFP drives Cre-dependent expression of ChR2-EYFP or EYFP to produce celltype-specific targeting of ChR2 or EYFP, respectively. In the presence of Cre, ChR2-EYFP or EYFP is inverted into the sense direction and expressed from the EF-1α promoter in PV-positive cells. ITR, inverted terminal repeat; polyA; WPRE, woodchuck hepatitis B virus post-transcriptional element.

b) ChR2-EYFP was strongly expressed in PV-positive interneurons in CA1 of 3-month-old 5XFAD/PV-Cre mice (scale bar = 100 μm).

c) Immunohistochemistry with anti-EYFP and anti-PV antibodies in CA1 of 3-month-old 5XFAD/PV-Cre mice expressing AAV-DIO-ChR2-EYFP shows EYFP expression only in PV-positive cells (scale bar = 50 μm).

d) Representative western blots showing levels of full-length APP (top left, CT695), APP CTFs (bottom left, CT695), APP NTFs (top right, A8967) and β-actin (bottom right, A5316, loading control) in CA1 in EYFP, random, and 40 Hz stimulation conditions, 1 mouse per lane, with 2 biological replicates of each condition.

e) Immunohistochemistry with anti-Aβ (12F4, red) antibodies in CA1 of 5XFAD/PV-Cre mice expressing only EYFP or ChR2 with 40 Hz, and random stimulation conditions (scale bar = 50 μm).

f) Bar graphs represent the relative immunoreactivity of Aβ normalized to EYFP (n=4 mice per group; * indicates $p<0.05$ and *** indicates $p<0.001$ by one-way ANOVA). Bar graphs show mean + SEM.

g) Immunohistochemistry with anti-Rab5 antibody (ADI-KAP-GP006-E, green) in CA1 of 5XFAD/PV-Cre mice (scale bar = 50 μm).

h) Relative Rab5 intensity levels normalized to EYFP controls (n=3 mice per group).

Aβ accumulation is thought to initiate multiple neurotoxic events typical for AD pathology. Therefore, we examined whether gamma stimulation affected overall Aβ peptide levels in the hippocampus of 5XFAD mice. We found that 1 hr of FS-PV-interneuron stimulation reduced $A\beta_{1\text{-}40}$ by 53.22% and $A\beta_{1\text{-}42}$ by 44.62% in the 40 Hz group which expresses ChR2 compared to the EYFP control group, as measured in CA1 by Aβ enzyme-linked immunosorbent assay (ELISA) (**Fig. 1f, g,** raw concentration (pg/ml) in **Ext. Data Table 1**). We performed a comprehensive set of control experiments to determine whether the effect was specific to frequency, cell type, and/or rhythmicity. Neither stimulation of CamKII-positive excitatory neurons at 40 Hz, nor FS-PV-interneurons at 8 Hz or random intervals significantly reduced Aβ levels (**Fig. 1f-i,** Methods). Immunohistochemical analysis using two β-amyloid-specific antibodies (Cell Signaling Technology; D54D2, BioLegend; 12F4[72]) in CA1 confirmed these results: Aβ labeling intensity was significantly reduced by 39.5% following 40 Hz stimulation compared to EYFP controls (**Fig. 2e, f,** D54D2 antibody, **Ext. Data Fig. 2e, f,** 12F4 antibody).

Brain amyloid concentration depends on Aβ production from amyloid precursor protein (APP) and Aβ clearance rates. To elucidate how 40 Hz stimulation reduced Aβproduction, we examined its effects on APP cleavage by measuring levels of the cleavage intermediates of APP, C-terminal fragments (CTFs) and N-terminal fragments (NTFs), in the hippocampus of the 5XFAD/PV-Cre mice. Following 40 Hz stimulation, we found significantly reduced APP CTFs and NTFs compared to EYFP and random controls (**Fig. 2a, b, c, d**, **Ext. Data Fig. 2d**). Prior work has shown that APP is transported and processed in recycling endosomes[73], and enlarged early endosomes have been observed in brain tissue from AD patients[74]. Therefore, we characterized endosomes in CA1 following stimulation using two markers, EEA1 (early endosomal antigen 1) and Rab5 (Ras-related protein encoded by the *RAB5A* gene). Altogether,

Figure 2

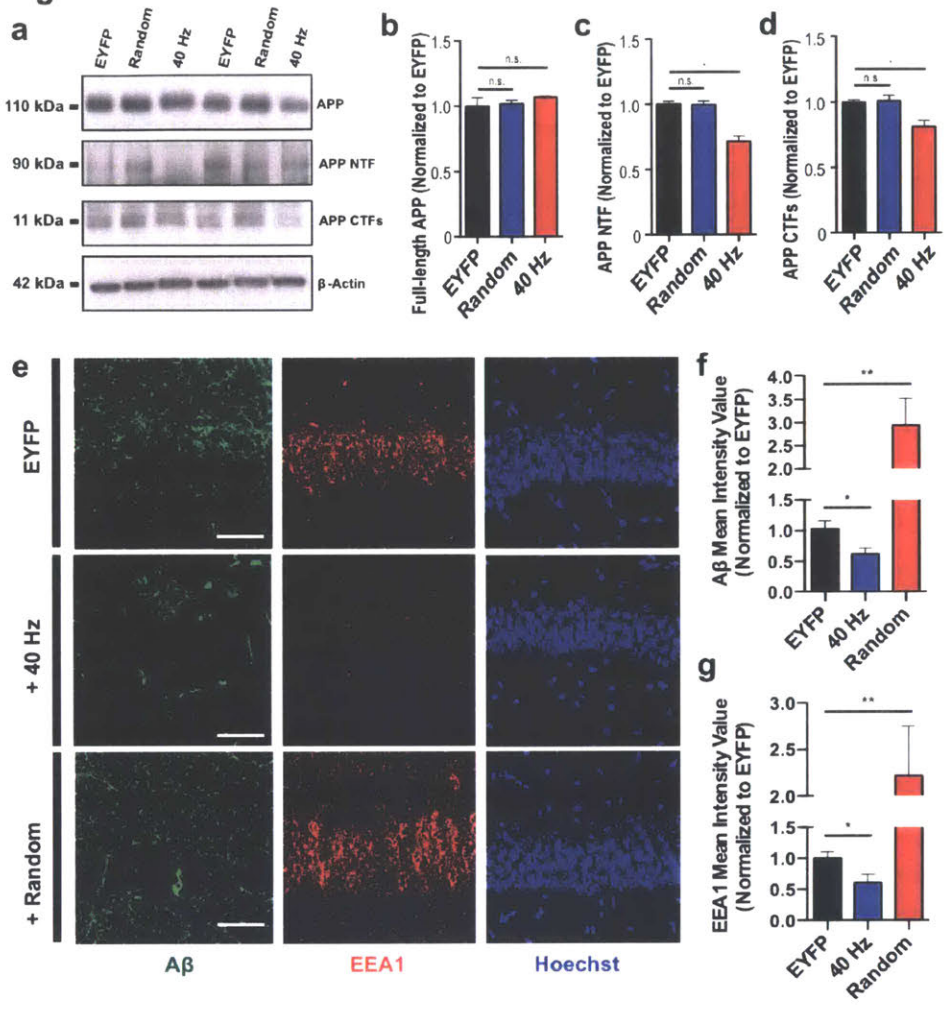

Figure 2: Driving 40 Hz oscillations optogenetically in hippocampus reduces Aβ in 5XFAD mice

a) Representative western blot showing levels of APP (CT695), APP NTFs (A8967), APP CTFs (CT695), and β-Actin (A5316, loading control) in CA1 of 5XFAD/PV-Cre mice expressing only EYFP or ChR2 with 40 Hz, or random stimulation conditions. 1 mouse per lane, 2 biological replicates.

b) Relative immunoreactivity of full-length APP normalized to actin (for ***b-d,*** n=6 mice per group).

c) Relative immunoreactivity of APP NTF normalized to actin.

d) Relative immunoreactivity of APP CTFs normalized to actin.

e) Immunohistochemistry with anti-Aβ(D54D2, green) and anti-EEA1 (610457, red) antibodies in CA1 of 5XFAD/PV-Cre mice (scale bar = 50 μm).

f) Relative immunoreactivity of Aβ normalized to EYFP controls (for ***f, g,*** n=3 mice per group).

g) Relative immunoreactivity of EEA1 normalized to EYFP controls.

n.s. not significant, * $p<0.05$, ** $p<0.01$, by one-way ANOVA; mean + SEM in bar graphs.

the intensity of endosomal labeling of CA1 neurons significantly decreased in both EEA1 (39.7%) and Rab5 (40.1%) following 40 Hz stimulation compared to EYFP controls (**Fig. 2e, g, Ext. Data Fig. 2g, h**). These results suggest that in addition to observed changes in APP cleavage products, 40 Hz stimulation also alters general endosomal processing.

Gamma stimulation induced morphological transformation of microglia

To further explore the cellular and molecular effects of stimulation in an unbiased manner, we performed genome-wide RNA sequencing (RNA-seq) of CA1 tissue following 1 hr of 40 Hz or no stimulation (EYFP) of the 5XFAD/PV-Cre mice (**Fig. 3a**, **Ext. Data Fig. 3a**, **b, c**). Interestingly, 35% of all up-regulated genes had their highest expression in microglia (**Fig. 3b**). This RNA-seq analysis strongly suggests that 40 Hz stimulation causes an alteration in the state of microglia, which is significant given the accumulating evidence that microglia play a role in AD pathology.[75] Transcriptomic changes following 40 Hz stimulation were positively correlated with changes due to increased neural activity (by NMDA and bicuculline), and negatively correlated with changes due to silencing activity (by tetrodotoxin) (**Ext. Data Fig. 3d**). The immediate early genes *Nr4a1*, *Arc*, and *Npas4*, which are up-regulated by neuronal activity, were elevated as shown by both RNA-seq and RT-qPCR (**Ext. Data Fig. 3e**). These transcriptomic results also suggest an engulfing state of microglia. The up-regulated genes were positively correlated with genomic changes induced by macrophage colony-stimulating factor (MCSF) and granulocyte macrophage colony-stimulating factor (GMCSF), known to promote microglial Aβ uptake (**Ext. Data Fig. 3d**).[49] RT-qPCR confirmed that up-regulated genes included microglial engulfment associated genes *Cd68*, *B2m*, *Bst2*, *Icam1*, and *Lyz2* (**Fig. 3c**). Microglia-enriched transcriptional regulator *Irf7*, cell adhesion and migration regulator

Figure 3

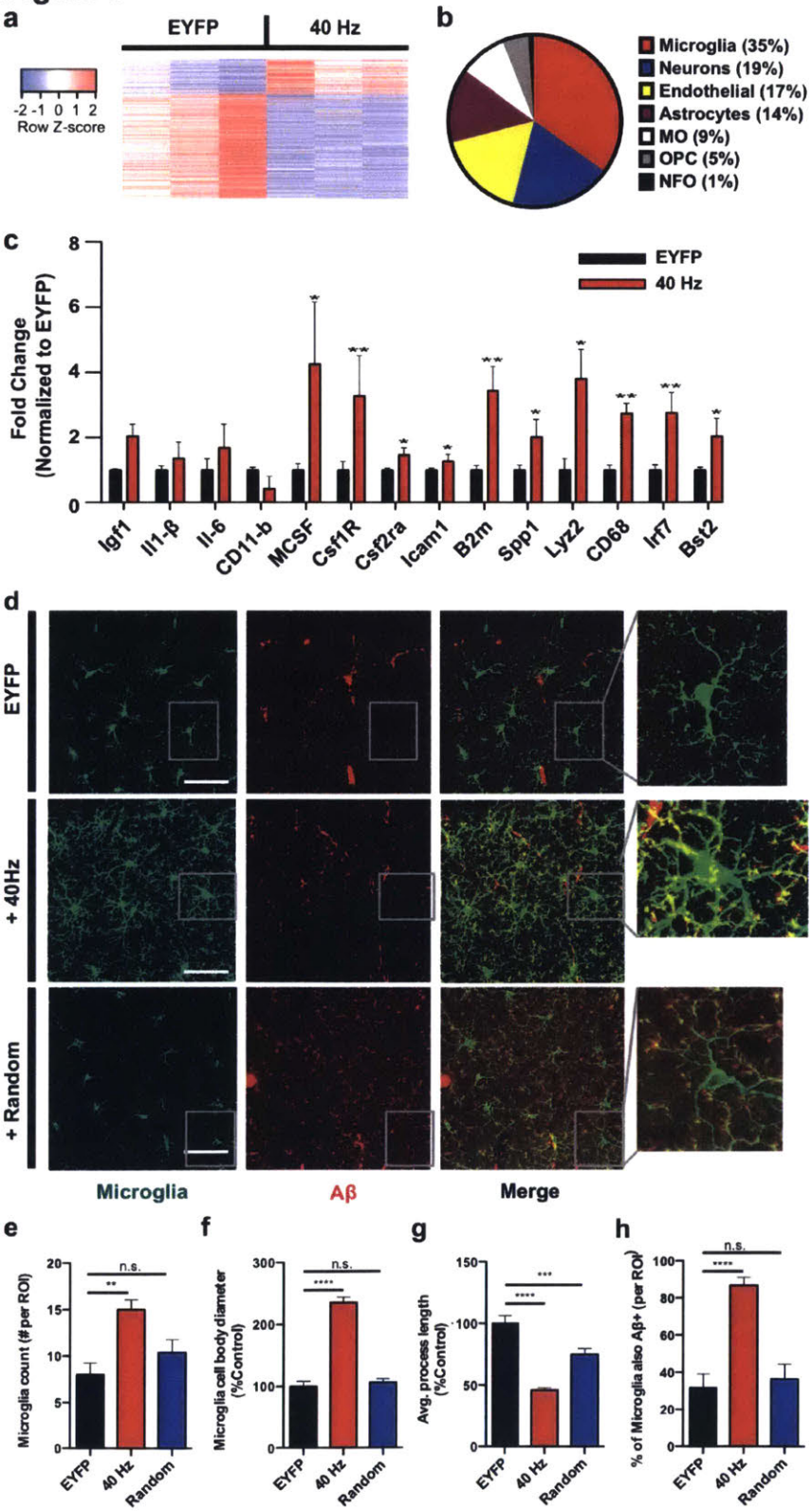
a
EYFP
40 Hz
-2 -1 0 1 2
Row Z-score
b
Microglia (35%)
Neurons (19%)
Endothelial (17%)
Astrocytes (14%)
MO (9%)
OPC (5%)
NFO (1%)
c
EYFP
40 Hz
Fold Change (Normalized to EYFP)
Igf1
Il1-β
Il-6
CD11-b
MCSF
Csf1R
Csf2ra
Icam1
B2m
Spp1
Lyz2
CD68
Irf7
Bst2
d
EYFP
+ 40Hz
+ Random
Microglia
Aβ
Merge
e
Microglia count (# per ROI)
n.s.
**
EYFP
40 Hz
Random
f
Microglia cell body diameter (%Control)
n.s.
****
EYFP
40 Hz
Random
g
Avg. process length (%Control)
***
****
EYFP
40 Hz
Random
h
% of Microglia also Aβ+ (per ROI)
n.s.
****
EYFP
40 Hz
Random

Figure 3: Driving 40 Hz oscillations optogenetically in hippocampus causes a distinct morphological transformation of microglia in 5XFAD mice

a) Heat map of differentially expressed genes determined by whole-transcriptome RNA-Seq of CA1 from 5XFAD/PV-Cre mice expressing only EYFP or ChR2 with 40 Hz stimulation. Normalized z-score values (high: red, low: blue) were calculated for each differentially expressed gene (row).

b) Cell-type-specific expression patterns of up-regulated genes following 40 Hz stimulation (MO: myelinating oligodendrocyte, OPC: oligodendrocyte progenitor cell, NFO: newly formed oligodendrocyte).

c) RT-qPCR of specific up-regulated genes: relative RNA levels (fold change) in CA1 of 5XFAD/PV-Cre expressing only EYFP or ChR2 with 40 Hz stimulation, normalized to EYFP controls (Student's t-test; n=6 mice per group).

d) Immunohistochemistry with anti-Iba1 (019-19741, green) to identify microglia and anti-Aβ (12F4, red) antibodies in CA1 of 5XFAD/PV-Cre mice expressing only EYFP or ChR2 with 40 Hz, and random stimulation (40x objective; scale bar = 50 μm).

e) Number of Iba1-positive microglia (for ***f-I***, *one*-way ANOVA; n=4 mice per group).

f) Diameter of Iba1-positive microglia cell bodies.

g) Average length of Iba1-positive microglia primary processes.

h) Percent of Iba1-positive microglia cell bodies that are also Aβ-positive.

n.s. not significant, * $p<0.05$, ** $p<0.01$, *** $p<0.001$, **** $p<0.0001$; mean + SEM in bar graphs.

Extended Data Figure 3

a Up-regulated genes

2010002N04Rik	Beta-s	Card10	Cyp2d22	Gldc	H1fx	Igfbp4	Lag3	Mpped1	Pcsk1n	Prrt1	Slc12a9	Tmem198
2010300C02Rik	Bst2	Cd68	Dcakd	Gm129	H2-D1	Igfbpl1	Lcat	Mt1	Pdzd2	Rab40b	Slc25a34	Tpst2
2410018L13Rik	C1qa	Cebpb	Egr4	Gm2115	H2-K1	Irf7	Lefty1	Mt2	Pqls	Rara	Slc29a4	Trim30a
Adra2c	C1qb	Cebpd	Erf	Gng7	Hipk4	Irf9	Lgals3bp	Mtap1s	Phyhd1	Rasl11b	Spp1	Tlr
Agfg2	C1qc	Cirbp	F730043M19Rik	Gpnmb	Hmox1	Itpka	Lingo3	Npy	Pitpnm2	Rbm3	Spsb1	Unc5a
Agxt2l1	C1ql2	Cnn2	Fam107a	Gpr25	I830012O16Rik	Junb	Lrg1	Nr1d1	Plekhg5	Rpph1	Ssbp4	Uqcr11
Arc	C1qtnf4	Cotl1	Fam163b	Gpr37l1	Icam1	Kcnc4	Ltbp4	Nr4a1	Pnpla7	Rprml	Sstr4	Usp18
Atf3	C3ar1	Crip2	Fmo2	Grm2	Icam5	Kcnh3	Lyz2	Oasl2	Pou3f1	Sbk1	Tfcp2l1	Vwf
B2m	C4b	Cst3	Fn1	Gstm1	Ifit1	Kcni4	Metrn	Palm	Ppp1r1a	Scara3	Thbs4	Wfs1
BC018242	Car7	Ctxn1	Gbp3	Gstm6	Ifit3	Klf16	Mmp12	Parp14	Prr7	Sh3bgrl3	Thrsp	Xdh

b Down-regulated genes

1700003M02Rik	A630089N07Rik	Arhgap24	Ccdc141	Cited2	Edil3	Fam19a4	Gpr115	Hs6st2	Kcnma1	Lrrc48	Necab2	Pcsk1	Prkcd	Rgs16	Sh3bgrl2	Spata18	Th	Tyrp1	Ysk4
1700007K13Rik	AF529169	Asb2	Ccdc153	Clec18a	Efcab1	Fbln7	Gpr123	Hsp90aa1	Kcnn3	Lrrc55	Necab3	Pdp1	Prkch	Rgs3	Shox2	Spock1	Timp2	Ubxn10	Zcchc12
1700009P17Rik	AU021034	Aspa	Ccdc19	Clic6	Efna5	Fgf1	Gpr139	Hsp90b1	Kcnq1ot1	Malat1	Nexn	Peg10	Prkcq	Rgs4	Shroom3	Spock3	Tm4sf1	Ugt8a	Zdbf2
1700026D08Rik	AW551984	Baiap3	Ccdc3	Cntn6	Eif5a2	Fgf10	Gpr151	Hspa4l	Kctd12b	Mcf2	Nfam1	Pgap1	Prkg2	Rgs6	Slc12a2	Srgap1	Tmem130	Unc13c	Zdhhc22
1700027A23Rik	Adamts15	Bbox1	Ccdc40	Cntnap4	Elavl2	Fhdc1	Gpr153	Htr2c	Kctd8	Megf11	Nob	Pgbd1	Prokr2	Rims3	Slc17a6	St8sia2	Tmem132c	Vangl1	Zfhx3
1700028P14Rik	Adamts9	Bmp7	Ccdc81	Cobl	Elavl4	Foxi1	Gpr26	Htr5b	Kif9	Mgat4c	Nhlh2	Phactr2	Prr5l	Rit2	Slc38a1	Strbp	Tmem163	Vat1	Zfp474
1700040L02Rik	Adcyap1	Btbd11	Cd109	Coch	Elfn1	Foxp2	Gpr4	Htr7	Kit	Mlf1	Nppa	Pirt	Prrg4	Rnf152	Slc39a4	Syt2b	Tmem176a	Vat1l	Zfp618
1700094D03Rik	Adra1b	C530008M17Rik	Cd24a	Col12a1	Emb	Frem3	Gprasp2	Hydin	Kitl	Mme	Npr1	Pkib	Plgds	Robo1	Slc5a3	Synpo2	Tmem212	Vav2	Zfp941
1810041L15Rik	Aebp1	Cacna2d2	Cdh26	Col8a2	Enkur	Fstl5	Gpx3	Inadl	Klhl1	Mob3b	Nr4a2	Plagl1	Ptpn14	Rorb	Slc5a7	Syt15	Tmem56	Vav3	Zic1
2310039L15Rik	Agt	Calb2	Cdhr3	Cone4	Eno4	Fzd1	Grb10	Ipce	Lars2	Mreg	Nrip3	Plcb4	Pvrl2	Rps6ka6	Slc6a9	Syt4	Tnc	Vwa5b1	Zic2
2410004P03Rik	Aif1l	Calr3	Cdr1	Cone9	Enox2	Fzd10	Grik4	Iqub	Lbh	Mrvi1	Nrp2	Plch1	Pvrl3	Rsph1	Slc7a11	Syt6	Tnnt1	Wbscr27	Zic3
3110047P20Rik	Ak4	Camk2d	Cdr2	Dach1	Epha6	Galntl3	Grid2ip	Irx1	Lhp	Msi2	Nrsn2	Plch2	Rab37	Rsph4a	Slc9a4	Syt9	Trhde	Wdr16	Zic4
3632451O06Rik	Ak7	Car10	Chat	Dcn	Epn3	Gap43	Grin3a	Irx2	Ldhd	Mtfr1	Ntng1	Plcxd2	Ramp3	Rspo2	Slco2a1	Tac1	Trim36	Wdr52	Zic5
4930451C15Rik	Akap12	Cast	Chgb	Ddc	Ermn	Gatm	Grk4	Irx3	Lect1	Mum1l1	Nudt4	Pid5	Ranbp3l	Scn1a	Slit2	Tac2	Trim66	Wdr6	
4932411L15	Amigo2	Cbln1	Chrdl1	Dnahc5	Etv1	Gdpd5	Grm4	Itga3	Lef1	Musk	Olfm3	Plekhg1	Rap1gap	Scube1	Sitrk6	Tacr1	Trpc3	Wdr78	
4932425I24Rik	Amotl1	Cbln2	Chrna3	Dnahc6	Exph5	Gfra1	Gucy1a3	Kcnc2	Lhfpl1	Myb	Optn	Plxnc1	Rasgef1b	Scube3	Sncg	Tcf7l2	Trps1	Wdr96	
5730508B09Rik	Ankrd29	Cbln4	Chrna4	Dpp10	Fabp7	Gm6300	Hcn4	Kcng4	Lhfpl3	Mycbpap	Otx2	Popdc3	Rassf9	Sema3d	Sntn	Tekt1	Tsku	Wtikkn2	
6330406I15Rik	Ankrd34c	Ccdc108	Chrnb3	Dpy19l1	Fam149a	Gm7609	Hdc	Kcnip1	Lhx9	Myoc	Pamr1	Pou4f1	Rbms3	Sema6a	Socs2	Tex15	Ttc18	Wif1	
A2m	Ang1	Ccdc135	Chrnb4	Dynlrb2	Fam198b	Gm973	Hhip	Kcnj12	Lrguk	Ndn	Pbx3	Ppp1r32	Resp18	Serpinf1	Sox5	Tex9	Ttc21a	Wls	
A330021E22Rik	Agp4	Ccdc136	Cit	Ebf1	Fam198b	Gng8	Hivep1	Kcnj16	Lrrc23	Necab1	Pcp4	Ppp1r36	Ret	Sgpp2	Spag16	Tgfb2	Ttc39a	Wnt3	

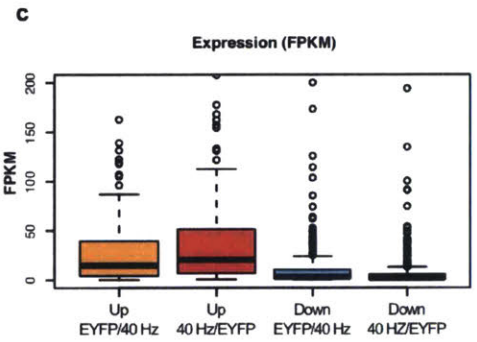

d

Enrichment of up-regulated genes under different perturbations

Name of perturbed transcriptome	NES	Nominal p-value	FDR q-value
MCSF treated microglia	1.76	0.000	0.000
NMDA treated neurons	1.62	0.000	0.000
IL34 treated microglia	1.59	0.000	0.000
GMCSF treated microglia	1.49	0.005	0.004
Bicuculline treated neurons	1.49	0.016	0.013
ALS SOD1 mutant microglia	-1.26	0.050	0.028
LPS&IFNg treated macrophage (M1)	1.18	0.122	0.081
MeCP2 null microglia	1.16	0.164	0.127
IL4 treated macrophage (M2)	-1.19	0.101	0.147
Huntington HTT mutant microglia	1.03	0.371	0.361
Germ-free microglia	0.94	0.604	0.667
Tetrodotoxin treated neurons	-0.76	0.941	0.970

NES: normalized enrichment score

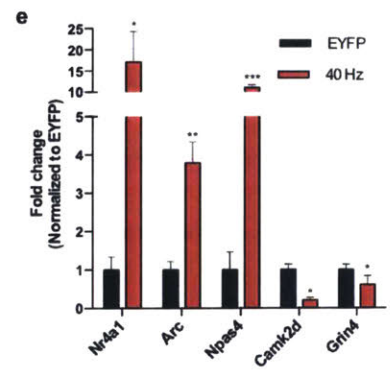

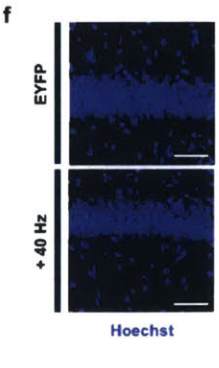

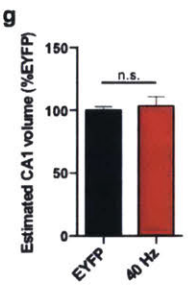

Extended Data Figure 3: Optogenetically driven 40 Hz oscillations in CA1 cause changes in gene regulation and immediate early gene expression

a) Table of 130 genes up-regulated by 40 Hz FS-PV-interneuron stimulation determined by whole transcriptome RNA-Seq of CA1 from 3-month-old 5XFAD/PV-Cre mice ($p<0.05$ by Cufflinks 2.2).

b) Table of 393 genes down-regulated by 40 Hz FS-PV-interneuron stimulation determined by whole transcriptome RNA-Seq of CA1 from 3-month-old 5XFAD/PV-Cre mice ($p<0.05$ by Cufflinks 2.2).

c) Box plot showing fragments per kilobase (FPKM) values of up- and down-regulated genes in EYFP and 40 Hz groups. Box shows median (black lines in box) and quartiles (top and bottom of box), whiskers show minimum and maximum values, and circles show outliers.

d) GSEA statistics tables showing statistical significance of correlation between genes up- or down- regulated by 40 Hz stimulation and publicly available neuron, microglia, and macrophage specific RNA-Seq data under different chemical and genetic perturbations; the perturbation terms were ranked based on the FDR q-values for the up-regulated gene list, from the smallest to the largest (Methods).

e) RT-qPCR verification of specific gene targets in the RNA-Seq data set. Bar graph shows relative RNA levels (fold change) from EYFP (black) and 40 Hz stimulation (red) conditions (* indicates $p<0.05$, ** indicates $p<0.01$,and *** indicates $p<0.001$ by Student's t-test, n=3 mice per group). All bar graphs show mean + SEM.

f) Immunohistochemistry with Hoechst to label all cell nuclei in CA1 of 5XFAD/PV-Cre mice expressing only EYFP or ChR2 with 40 Hz stimulation conditions (scale bar = 50 μm).

g) Bar graph represents the estimated CA1 thickness in 5XFAD/PV-Cre mice expressing only EYFP or ChR2 with 40 Hz stimulation conditions (n=4 mice per group; n.s. indicates not significant, by Student's t-test).

Spp1, and microglia proliferation markers *Csf1r* and *Csf2ra* were also up-regulated (**Fig. 3c**). Importantly, RT-qPCR showed that the expression levels of pro-inflammatory genes *Il6*, *Il1b* (*Il1-β*), *Itgam* (*CD11-b*) and an anti-inflammatory gene *Igf1* were not changed (**Fig. 3c**). Given that 40 Hz stimulation up-regulated both phagocytosis- and migration/cell adhesion-related genes, we examined morphological features of microglia activation. We used an antibody against microglial marker Iba1 to label microglia in CA1 sections from 5XFAD/PV-Cre mice after 1 hr of 40 Hz or random stimulation, or in mice expressing only EYFP (EYFP, **Fig. 3d**). We observed almost twice as many microglia in the 40 Hz group compared to EYFP and random control groups (**Fig. 3d, e**). Furthermore, microglia cell body diameter increased by 135.3% following 40 Hz stimulation compared to EYFP controls and by 138.7% compared to random stimulation (**Fig. 3d, f**). The length of microglia primary processes were reduced by 54.0% in the 40 Hz stimulation condition compared to EYFP controls and by 38.5% compared to random stimulation (**Fig. 3d, g**). Iba1 levels did not affect these findings as gene expression analysis showed that Iba1 expression did not differ between conditions (**Ext. Data Fig. 3a, b**). The increase in cell body size and decrease in process length observed after 40 Hz stimulation are consistent with a shift towards a phagocytic state of microglia.[25] To evaluate microglia Aβ uptake specifically, we measured co-localization of Aβ within microglia by co-immunostaining with an Aβantibody (12F4, Methods). The percent of microglia co-localized with Aβ in the cell body increased to 85.6% following 40 Hz stimulation from 31.7% (EYFP control, **Fig. 3d, h**). 3D renderings of microglia further demonstrate the presence of Aβ within microglia (**Ext. Data Vid. 1, 2, 3**). We did not find evidence of neuronal loss by measuring the CA1 cellular layer thickness (**Ext. Data Fig. 3f, g**). Together, these results suggest that gamma stimulation triggers microglia to increase Aβ uptake.

Chapter 3: Visual stimulation by light flicker decreases Aβ levels in visual cortex

Visual stimulation by light flicker induces gamma in visual cortex

Many studies have shown that visual stimulation can drive oscillations in the gamma range.[41,76] In particular, flickering lights at a specific frequency can induce that frequency in primary visual cortex (VC).[77] To determine if light flickering could entrain 40 Hz oscillations and subsequently alter Aβ, we exposed 5XFAD mice to 40 Hz flickering for 1 hr, analogous to optogenetic stimulation that reduced Aβ described above (**Fig. 4a**). In VC, we found that light flickering at 40 Hz increased power in the LFP at 40 Hz, while random interval flickering (random flicker) and dark exposure did not (**Fig. 4a, Ext. Data Fig. 4a**). All induced similar firing rates (**Ext. Data Fig. 4b, c**). Spiking increased and decreased concomitantly as the light flickered on and off, resulting in spiking entrained to 40 Hz during 40 Hz flicker but not during random flicker (**Fig. 4b**). Recordings from saline above the brain exhibited no change in 40 Hz power during 40 Hz flicker, showing that this effect was not due to photoelectric effects or electrical noise (**Ext. Data Fig. 4d, e**).

Given that 40 Hz light flicker entrains 40 Hz oscillations in VC, we aimed to determine whether 40 Hz flicker could reduce Aβ levels. 3-month-old 5XFAD mice were placed in a dark box and exposed to either light flicker at different frequencies (20, 40, or 80 Hz), random flicker, constant light on (light), or dark for 1 hr. One hour after 1 hr of 40 Hz flicker, we observed that $A\beta_{1-40}$ levels in VC were reduced by 57.96% and $A\beta_{1-42}$ levels by 57.97% compared to dark controls (as measured by Aβ ELISA, **Fig. 4c**). The effect was specific to 40 Hz flicker as neither constant light nor 20 Hz, 80 Hz, or random flicker significantly reduced Aβ levels compared to dark and light controls (**Fig. 4c**). We also found no change in Aβ levels in somatosensory barrel

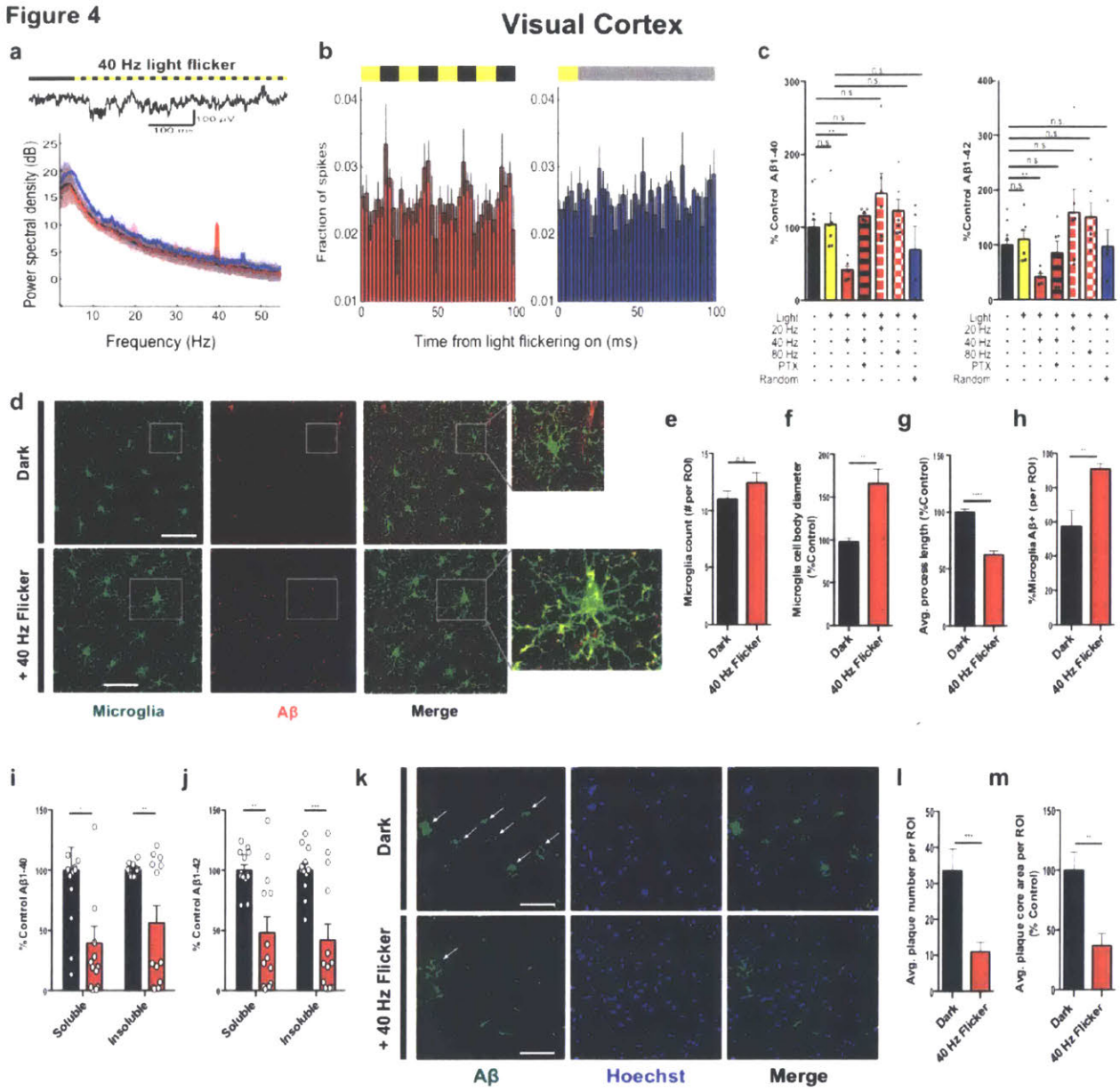

Figure 4: Driving 40 Hz oscillations in VC via light flicker reduces Aβ and amyloid plaques in 5XFAD mice

a) Local field potential trace in VC before and during 40 Hz light flicker (above). Power spectral density mean and standard deviation (below, n=4 5XFAD mice, 5 recording sessions).

b) Fraction of spikes in VC over 4 cycles of 40 Hz flicker (left) or the equivalent time for random flicker (right, n=4 5XFAD mice from 5 recording sessions, mean ± SEM across animals). For random stimulation, spiking was aligned to light turning on, grey indicates additional light-on flickers occurring randomly (Methods).

c) Relative $A\beta_{1-40}$ (left) and $A\beta_{1-42}$ (right) levels normalized to dark, in VC of 5XFAD mice exposed to dark, light, 40 Hz, 20 Hz, 80 Hz, 40 Hz with picrotoxin (PTX), and random conditions (n=12 dark; n=6 light, 40 Hz, 20 Hz, 80 Hz flicker and PTX; n=4 random mice; one-way ANOVA).

d) Immunohistochemistry with anti-Iba1 (019-19741, green) and anti-Aβ(12F4, red) antibodies in VC of 5XFAD mice exposed to dark or 40 Hz flicker. Right: 120X zoom; arrows indicate +Iba1/+Aβsignal in cell body (scale bar=50 μm).

e) Number of Iba1-positive microglia (for ***e-h*** Student's t-test unpaired, n=4 mice per group)

f) Diameter of Iba1-positive microglia cell bodies.

g) Average length of Iba1-positive microglia primary processes.

h) Percent of Iba1-positive microglia cell bodies that are also Aβ-positive.

i) Relative $A\beta_{1-40}$ levels in VC of 6-month-old 5XFAD mice after 7 days of 1 hr/day dark or 40 Hz flicker (Student's t-test unpaired; n=13 mice per group).

j) As in ***i*** for $A\beta_{1-42}$.

k) Immunohistochemistry with anti-Aβ (D5452, green) antibody in 6-month-old VC of 5XFAD mice after 7 days of 1 hr/day dark or 40 Hz flicker showing plaques (white arrows; scale bar=50 μm).

l) Number of Aβ-positive plaques; (for ***l,m*** Student's t-test unpaired, n=8 mice per group).

m) Area of Aβ-positive plaques.

n.s. not significant, * $p<0.05$, ** $p<0.01$, *** $p<0.001$; circles indicate n, mean + SEM in bar graphs.

Extended Data Figure 4

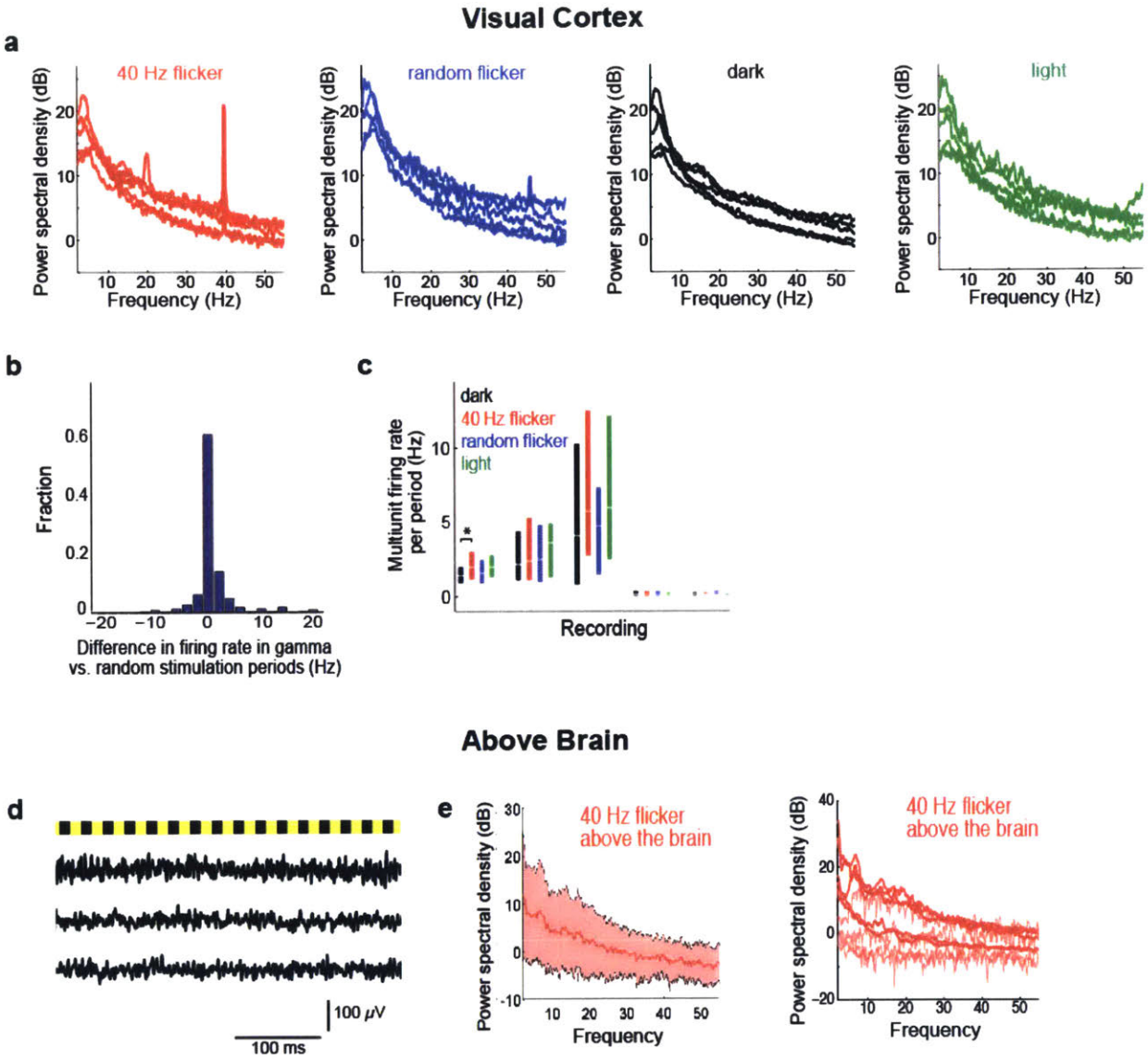

Extended Data Figure 4: 40 Hz light flicker drives 40 Hz oscillations in VC, while random flickering does not

a) Power spectral densities of local field potentials in VC during 40 Hz light flicker (red, far left), random light flicker (blue, center left), dark (black, center right), or light (green, far right) in VC for each recording session for each mouse (n=5 recordings from 4 5XFAD mice with 47, 51, 64, 49, 16 40 Hz flicker, 47, 50, 64, 50, 16 random flicker, 279, 301,

382, 294, 93 dark and 47, 50, 64, 49, 15 light periods). Light flicker at other frequencies increased power in the flicker frequency, as others have found previously[76,77] (data not shown).

b) Histogram of the difference in firing rates between 40 Hz light flicker and random light flicker (n=226 stimulation periods from 5 recording sessions in 4 5XFAD mice).

c) Multiunit firing rates in VC during 40 Hz light flicker (red), random light flicker (blue), dark (black), or light (green) periods. Box plots show median (white lines in box) and quartiles (top and bottom of box). In all animals, firing rates between 40 Hz flicker and random flicker conditions were not significantly different showing that the random stimulation condition serves as a control for spiking activity (ranksum tests for each of 5 recording session from 4 5XFAD mice, p's>0.06, n=47, 51, 64, 49, 16 40 Hz flicker periods and 47, 50, 64, 50, 16 random flicker periods per recording). There were no significant differences in firing rates between 40 Hz flicker and light conditions indicating that 40 Hz light flicker generally did not cause neuronal hyperexcitability (ranksum tests for each of 5 recording session from 4 5XFAD mice, p's > 0.2 for 4 recording sessions, p<0.01 for 1 recording session, which is not significant when corrected for performing multiple comparisons, n=47, 51, 64, 49, 16 40 Hz periods and 47, 50, 64, 49, 16 light periods per recording). In one session, there was more activity in the 40 Hz flicker than in the dark condition.

d) Example traces of LFPs recorded above the brain during light flicker (above, yellow indicates light on, black indicates light off), during three different recording sessions.

e) Power spectral densities of LFPs recorded above the brain during 40 Hz light flicker show no increase in power at 40 Hz. Thus, the effect is not due to photoelectric effects on

recording equipment or electrical noise (n= 4, 2, 1, 1, 17, 42, 36, 55, 53 40 Hz flicker periods from 4 recording sessions in 3 5XFAD mice undergoing VC recordings and from 5 recording sessions in 2 5XFAD and 3 WT mice undergoing hippocampal recordings). Mean (solid line) and standard deviation (shaded area) across recordings are shown on the left and per animal on the right. Recordings with less than 3 flicker periods (light red) resulted in noisier power spectral densities than recordings with more data (dark red) but none showed evidence of peaks at 40 Hz.

cortex and hippocampus following 40 Hz flicker (**Ext. Data Fig. 5a-h**). When we pretreated 5XFAD mice with a low dose $GABA_A$ antagonist (picrotoxin, 0.18 mg/kg [78]), the effects of 40 Hz flicker on Aβ levels were completely abrogated, indicating that GABAergic neurotransmission is necessary for this effect (**Fig. 4c**). To demonstrate that these effects extend beyond the 5XFAD mouse, we examined the effect of 40 Hz flicker in APP/PS1 mice, another well-validated AD model, [79] and found significantly reduced $A\beta_{1-40}$, by 20.80%, and a non-significant trend of reduced $A\beta_{1-42}$ by 37.68% (**Ext. Data Fig. 6a**). Furthermore, in 9-month-old WT mice, we found a 58.2% reduction in endogenous mouse $A\beta_{1-40}$ following 1 hr of 40 Hz flicker (**Ext. Data Fig. 6b**). The reduction of endogenous mouse $A\beta_{1-40}$ in WT animals reveals that these effects are not restricted to transgenic APP expression or mutant APP; rather, they extend to Aβ produced from endogenous APP driven by its endogenous promoter.

Next, we investigated whether 40 Hz flicker alters microglia activity in VC in a similar manner that 40 Hz optogenetic stimulation altered CA1 microglia. While microglia number was unchanged (**Fig. 4d, e**), microglia cell body diameter increased by 165.8% following 40 Hz flicker compared to dark controls (**Fig. 4d, f**). Microglia primary process lengths were reduced by 37.7% after 40 Hz flicker compared to dark controls (**Fig. 4d, g**). Consistent with this morphology, which indicates enhanced engulfment activity,[25] Aβ/Iba1 co-localization in the cell body was increased to 90.8% after 40 Hz flicker from 57.3% in the dark condition, indicating more Aβ-bearing microglia (**Fig. 4d, h**, $p<0.01$). To demonstrate that microglia indeed engulf *A*β in the 5XFAD mouse, we purified microglia from 5XFAD and WT animals using fluorescence-activated cell sorting (FACS, Methods) and analyzed Aβ levels via ELISA. We found that microglia-specific levels of Aβ are significantly higher in 5XFAD animals than in WT controls

Extended Data Figure 5

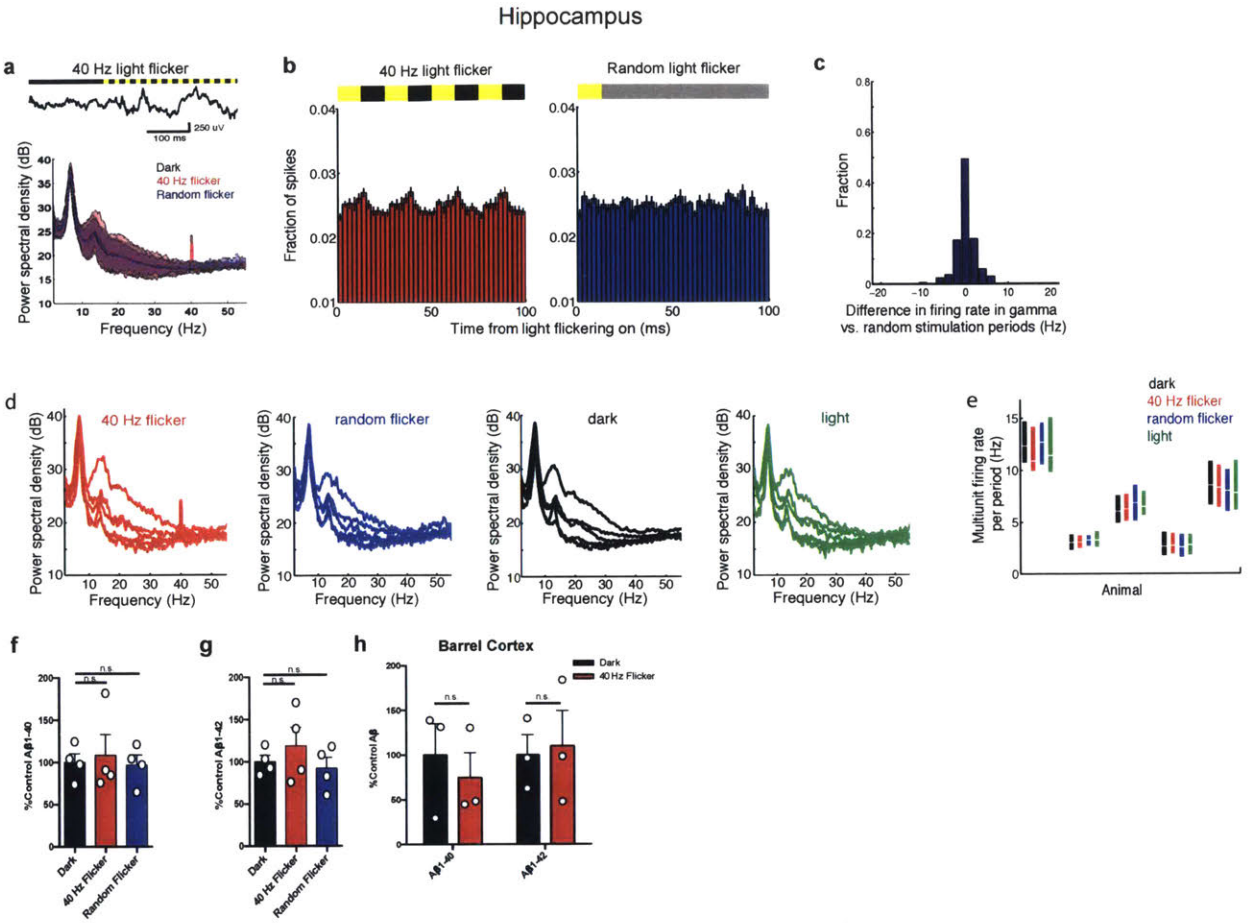

Extended Data Figure 5: 40 Hz light flicker does not affect Aβ levels in hippocampus or barrel cortex

a) Example local field potential trace in hippocampal CA1 before and during 40 Hz light flicker (above). Mean (solid line) and standard deviation (shaded area) of power spectral density during 40 Hz light flicker (red), random light flicker (blue), or dark (black) in CA1 (n=2 5XFAD and 3 WT mice).

b) Histogram of the fraction of spikes in hippocampus as a function of time for 4 cycles of 40 Hz light flicker (left, red) or the equivalent period of time for random light flicker (right, blue, n=2 5XFAD and 3 WT mice, mean ± SEM across animals). Bar above indicates when light was on (yellow) or off (black). For random stimulation, spiking was

aligned to the start of the light turning on, additional periods with light-on occurred at random intervals indicated by grey (Methods).

c) Histogram of the difference in firing rates between 40 Hz light flicker and random light flicker (bottom n=168 stimulation periods from 5 recording sessions in 2 5XFAD and 3 WT mice).

d) Power spectral densities of local field potentials in CA1 during 40 Hz light flicker (red, far left), random light flicker (blue, center left), dark (black, center right), or light (green, far right) for each recording session for each mouse (n=5 recordings from 2 5XFAD and 3 WT mice with 22, 54, 42, 71, 55, 40 Hz flicker, 12, 34, 32, 54, 36 random flicker, 115, 240, 224, 342, 282 dark and 12, 33, 33, 54, 35 light periods).

e) Multiunit firing rates in CA1 during 40 Hz light flicker (red), random light flicker (blue), dark (black), or light (green) periods. Box plots show median (white lines in box) and quartiles (top and bottom of box). In all animals firing rates between 40 Hz flicker and random flicker conditions were not significantly different showing that the random stimulation condition serves as a control for spiking activity (ranksum tests for each of 5 recordings from 2 5XFAD and 3 WT animals, p's>0.2, n=22, 54, 42, 71, 55 40 Hz flicker periods and 12, 34, 32, 54, 36 random flicker periods per recording). There were no significant differences in firing rates between 40 Hz flicker and light conditions indicating that 40 Hz light flicker generally did not cause neuronal hyperexcitability (ranksum tests for each of 5 recordings from 2 5XFAD and 3 WT animals, p's > 0.3, n=22, 54, 42, 71, 55 40 Hz periods and 12, 34, 33, 54, 35 light periods per recording).

f) Bar graphs of relative $A\beta_{1-40}$ levels in VC of 5XFAD mice in dark, 40 Hz flicker, and random flicker conditions, normalized to dark (n=4 mice per group; n.s. indicates not

significant). Bar graphs represent mean + SEM. Circles superimposed on bars in bar graphs indicate individual data points in each group.

g) Bar graphs of relative $A\beta_{1-42}$ levels in VC of 5XFAD mice in dark, 40 Hz flicker, and random flicker conditions, normalized to dark (n=4 mice per group; n.s. indicates not significant). Bar graphs represent mean + SEM. Circles superimposed on bars in bar graphs indicate individual data points in each group.

h) Bar graph of relative $A\beta_{1-40}$ and $A\beta_{1-42}$ levels in barrel cortex of 5XFAD mice in dark and 40 Hz flicker conditions, normalized to dark (n=3 mice per group; n.s. indicates not significant by Student's t-test).

Extended Data Figure 6

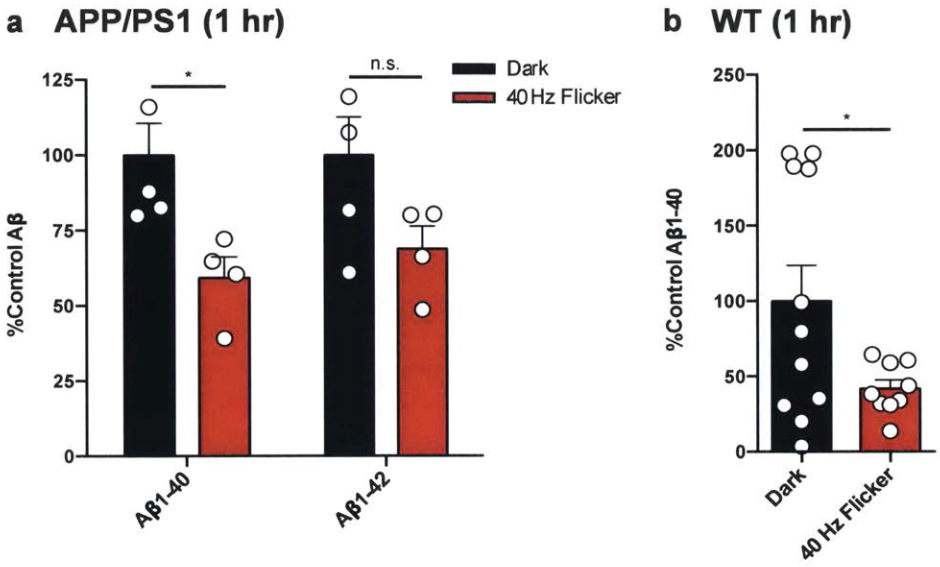

Extended Data Figure 6: Acute reduction in Aβ after light flicker in APP/PS1 and WT mice

a) Bar graph of relative $A\beta_{1\text{-}40}$ and $A\beta_{1\text{-}42}$ levels of APP/PS1 in VC in dark and 40 Hz flicker conditions, normalized to dark (n=4 mice per group; n.s. indicates not significant and * indicates $p<0.05$, by Student's t-test). All bar graphs show mean + SEM throughout this figure. Circles superimposed on bars in bar graphs indicate individual data points in each group.

b) Bar graph of relative mouse $A\beta_{1\text{-}40}$ and $A\beta_{1\text{-}42}$ levels in VC of 9-month-old WT mice in dark and 40 Hz flicker conditions, normalized to dark (n=11 mice per group for dark and n=9 mice per group for 40 Hz flicker conditions; * indicates $p<0.05$, by Student's t-test).

(**Ext. Data Fig. 7a, b**). Synaptophysin levels did not change between dark and 40 Hz flicker conditions, indicating that microglia activation likely did not affect synapse number (**Ext. Data Fig. 7c, d**, n.s. = not significant, n=4 mice). Thus, 40 Hz oscillations induced non-invasively via sensory entrainment reduced Aβ abundance and promoted microglia/Aβ interactions.

Chronic visual stimulation by light flicker decreases plaque load in VC

We next assessed whether 40 Hz flicker was effective to treat animals that have amyloid plaques. Because the effects of 40 Hz flicker on soluble Aβ levels were transient (**Ext. Data Fig. 8a**), we hypothesized that we would need repeated exposure to affect insoluble Aβ. Thus, we treated 6-month-old 5XFAD mice, which have amyloid plaque pathology in many brain regions including VC,[69] for 1 hr daily over 7 days with 40 Hz flicker or dark, and analyzed VC tissue 24 hr later. We found that 7 days of 1 hr 40 Hz flicker reduced both soluble $A\beta_{1-40}$ and $A\beta_{1-42}$ levels, by 60.5% and 51.7% respectively, (**Fig. 4i, j**) and insoluble $A\beta_{1-40}$ and $A\beta_{1-42}$ levels by 43.7% and 57.9% respectively (**Fig. 4i, j**). Immunohistochemical analysis showed that 40 Hz flicker significantly reduced plaque number in VC by 67.2% compared to dark controls (**Fig. 4k, l**) and plaque size by 63.7% (**Fig. 4k, m**). Taken together, these experiments identify a non-invasive treatment with a profound effect on amyloid plaque pathology.

Chronic visual stimulation by light flicker decreases phosphoTau in VC

To determine if 40 Hz flicker improves another key AD-related pathology, we investigated tau phosphorylation using the TauP301S tauopathy mouse model.[80] 4-month-old TauP301S transgenic mice, which show phosphorylated tau localized to the cell body at this age, were treated with either 40 Hz flicker or dark control conditions for 1 hr daily for 7 days. To examine

Extended Data Figure 7

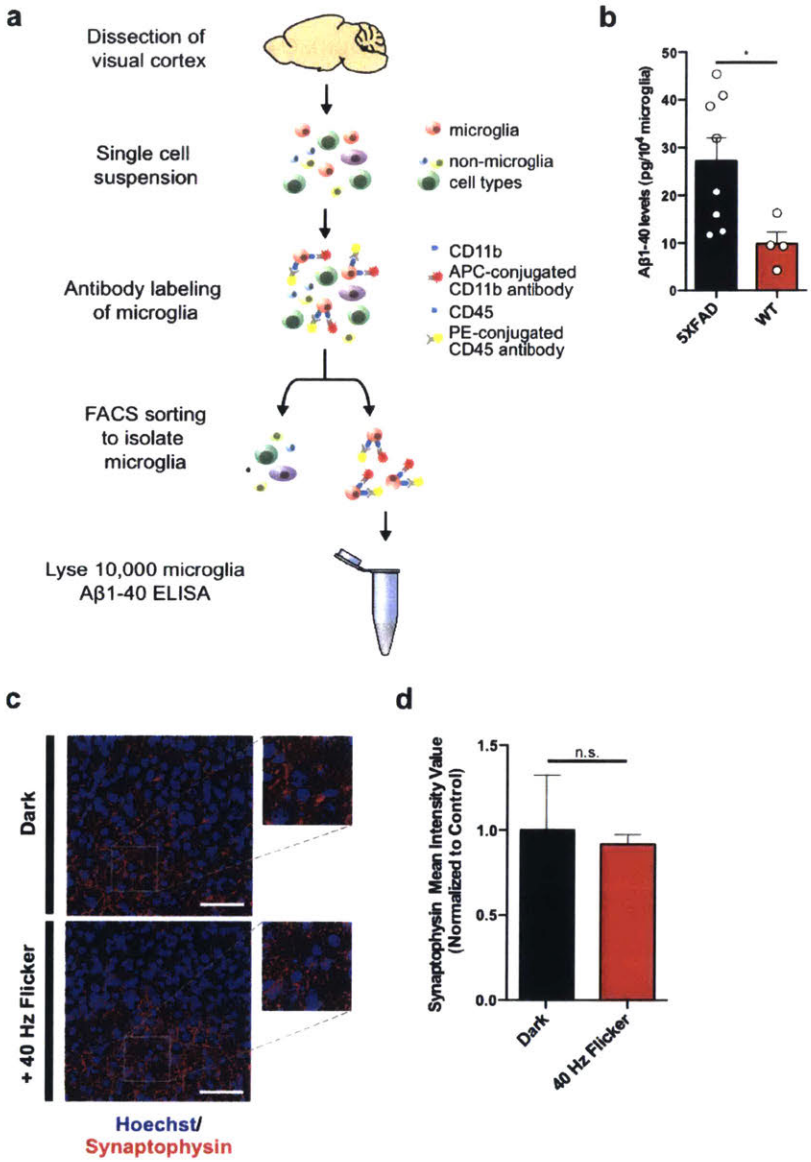

Extended Data Figure 7: 40 Hz light flicker does not decrease synaptic density in VC

a) Schematic depicting isolation of microglia from VC. VC was dissected, then single cells were suspended and labeled with CD11b and CD45 antibodies. Subsequently, cells were sorted via fluorescence-activated cell sorting (FACS) and lysed. $A\beta_{1\text{-}40}$ levels were analyzed by ELISA.

b) Bar graph of $A\beta_{1-40}$ levels in microglia purified using FACS (Methods) from VC of 3-month-old 5XFAD and WT mice (n=8 mice per group for 5XFAD and n=4 mice per group for WT mice; * indicates $p<0.05$ by Student's t-test). Circles superimposed on bars in bar graphs indicate individual data points in each group.

c) Immunohistochemistry with SVP38 (red) antibodies to detect synaptophysin in VC of 3-month-old 5XFAD mice in dark and 40 Hz flicker conditions (Images were taken with 40x objective; scale bar = 50 μm). Right: 100X rendering of dark and 40 Hz flicker conditions.

d) Bar graph of relative SVP38 intensity levels in VC of 5XFAD mice after dark (black) and 40 Hz (red) flicker conditions, normalized to dark (n=4 mice per group; n.s. indicates not significant, by Student's t-test).

Extended Data Figure 8

a Recovery after 1 hr 40 Hz Flicker

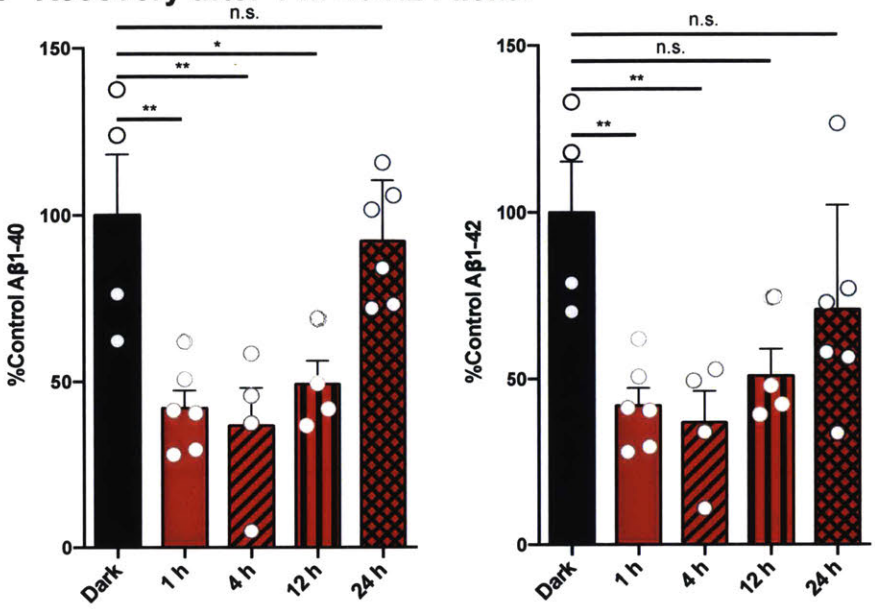

Extended Data Figure 8: Aβ levels in VC return to baseline 24 hr after 1 hr of 40 Hz light flicker

Bar graph of relative $A\beta_{1\text{-}40}$ and $A\beta_{1\text{-}42}$ levels in VC of 5XFAD mice 1, 4, 12, and 24 hours after 1 hour of dark or 40 Hz flicker treatment, normalized to dark (n=4 mice per group for 4 and 12 hr wait, n=6 for 1 and 24 hr wait, n=12 for dark; n.s. indicates not significant, * indicates $p<0.05$ and ** indicates $p<0.01$, by one-way ANOVA).

how 40 Hz flicker altered tau phosphorylation, we performed immunohistochemical characterization of the visual cortex using phosphoTau (pTau) antibodies against three different epitopes of pTau (S202, S396, and S400/T403/S404; 11834S, 9632S, 11837S, see Methods) and dendritic marker MAP2 as a control (**Ext. Data Fig. 9a, b, c**). The results showed that the signal intensity of the pTau(S202) was reduced by 41.2 % and pTau(S400/T403/S404) by 42.3 % in the 40 Hz flicker conditions compared to dark controls (**Ext. Data Fig. 9a, b, f, g**, p's<0.01 by Student's t-test, n = 2 sections from 8 mice per group), while MAP2 levels were unchanged (**Ext. Data Fig. 9a, c**, n.s. – not significant, n = 2 sections from 4 mice per group). Staining with an antibody against pTau (S396) showed a trend in the same direction: 40 Hz flicker reduced pTau (S396) levels by 14.4% compared to dark controls (see **Ext. Data Fig. 9d, e,** n.s. – not significant, n = 2 sections from 8 mice per group). Moreover, we observed less punctate and cell-body localization of pTau signal in response to 40 Hz flicker compared to the dark controls (**Ext. Data Fig. 9a**). Although we see significant changes in tau phosphorylation, we observe no discernable difference in the levels of insoluble tau between 40 Hz flicker treated and dark control groups (Data not shown).

We also evaluated the consequence of 40 Hz flicker on microglia in the TauP301S mouse model. We labeled microglia with an anti-Iba1 antibody in visual cortex sections of the TauP301S mouse following 7 days of 1 hr daily 40 Hz flicker or dark conditions (**Ext. Data Fig. 9h**). We observed a trend towards a 29.50 % increase in microglia number in 40 Hz flicker conditions compared to dark controls (**Ext. Data Fig. 9h, i,** n.s. – not significant, n = 3 mice per group) consistent with observations made in the 5XFAD model (**Fig. 4e**). In addition, the microglia cell body diameter increased by 49.00% following 40 Hz flicker in the visual cortex compared to dark controls (**Ext. Data Fig. 9h, j**, p<0.0001 by Student's t-test, n = 3 mice per

Extended Data Figure 9

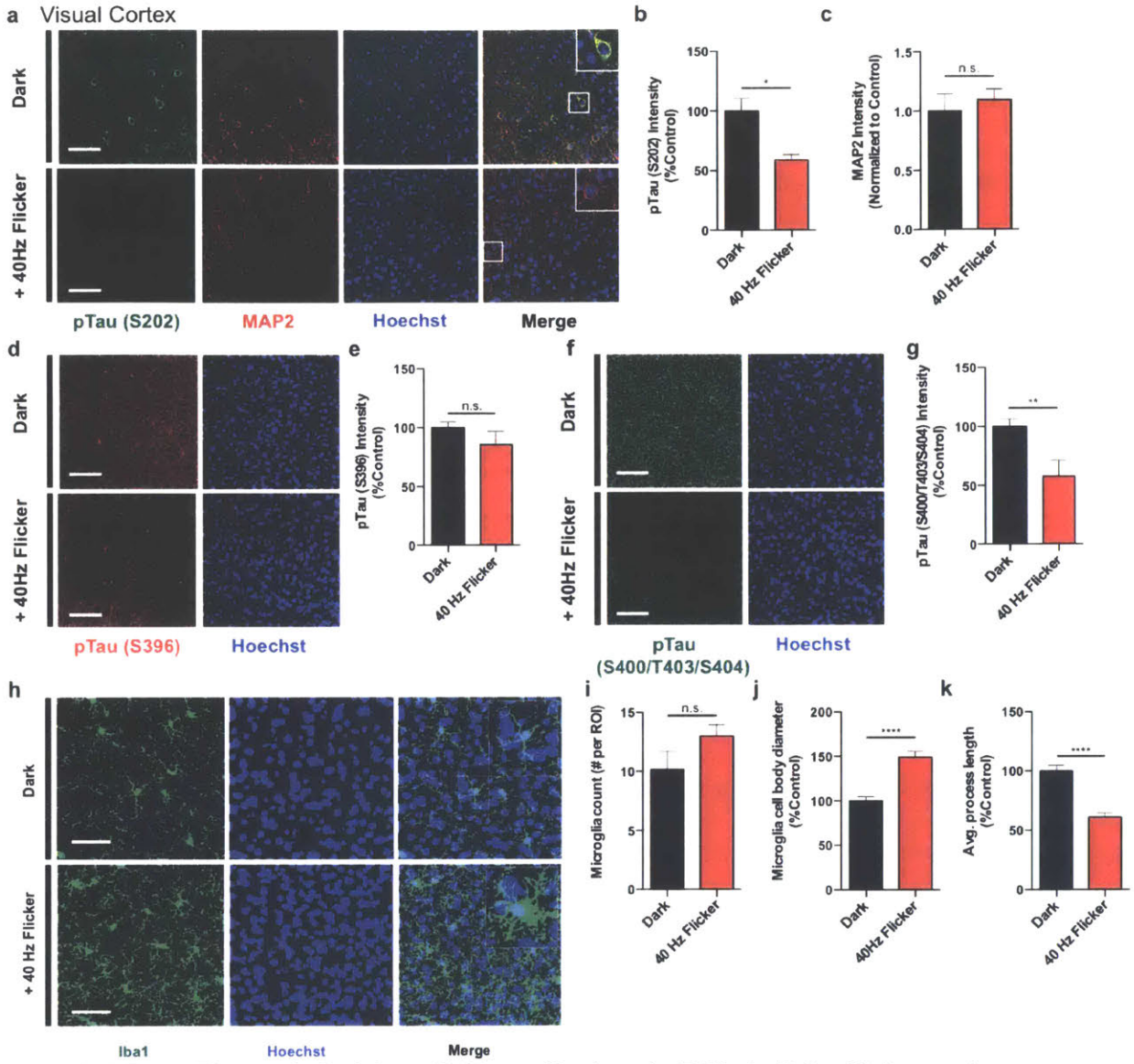

Extended Data Figure 9: Driving 40 Hz oscillations in VC via light flicker reduces phosphorylated tau in a tauopathy mouse model

a) Immunohistochemistry with anti-pTau (S202, green) and anti-MAP2 (red) antibodies in VC of 4-month-old P301S mice after 7 days of 1 hr/day dark or 40 Hz flicker conditions (Images were taken with 40x objective; scale bar = 50 μm). Insets: 100X rendering of representative cell body in dark and 40 Hz flicker conditions. No changes were observed by western blot (**Data not shown**).

b) Bar graph of relative pTau (S202) intensity levels in P301S mice after 7 days of 1 hr/day dark (black) and 40 Hz flicker (red) conditions (n=8 mice per group; * indicates $p<0.05$ by Student's t-test). All bar graphs show mean + SEM throughout this figure.

c) Bar graph of relative MAP2 intensity levels in P301S mice after 7 days of 1 hr/day dark (black) and 40 Hz flicker (red) conditions (n=8 mice per group; n.s. indicates not significant by Student's t-test).

d) Immunohistochemistry with anti-pTau (S396, red) antibodies in P301S mice after 7days of 1 hr/day dark and 40 Hz flicker conditions (scale bar = 50 μm).

e) Bar graph of relative pTau (S396) fluorescence intensity levels in P301S mice after 7 days of 1 hr/day dark (black) and 40 Hz flicker (red) conditions (n=8 mice per group; **** indicates $p<0.0001$ by Student's t-test).

f) Immunohistochemistry with anti-pTau (S404, green) antibodies in P301S mice after 7 days of 1 hr/day dark and 40 Hz flicker conditions (cale bar = 50 μm).

g) Bar graph of relative pTau (S400/T403/S404) fluorescence intensity levels in P301S mice after 7 days of 1 hr/day dark (black) and 40 Hz flicker (red) conditions (n=8 mice per group; ** indicates $p<0.01$ by Student's t-test). Bar graphs show mean + SEM.

h) Immunohistochemistry with anti-Iba1 (019-19741, green) antibodies in 4-month-old P301S mice after 7 days of 1 hr/day dark and 40 Hz flicker conditions (Images were taken with 40x objective; scale bar = 50 μm.) Insets: 100X rendering of representative microglia in EYFP and 40 Hz stimulation conditions.

i) Bar graph of the number of microglia in P301S mice after 7 days of 1 hr/day dark (black) and 40 Hz flicker (red) conditions (n=8 mice per group; n.s. indicates not significant by Student's t-test).

j) Bar graph of the diameter of microglia cell bodies in P301S mice normalized to dark after 7 days of 1 hr/day dark (black) and 40 Hz flicker (red) conditions (n=8 mice per group; **** indicates $p<0.0001$ by Student's t-test).

k) Bar graph of the average length of microglia primary processes in P301S mice normalized to control after 7 days of 1 hr/day dark (black) and 40 Hz flicker (red) conditions (n=8 mice per group; **** indicates $p<0.0001$ by Student's t-test).

group). The length of microglia primary processes was reduced by 39.08% in 40 Hz flicker group compared to dark controls (**Ext. Data Fig. 9h, k**, $p<0.0001$ by Student's t-test, $n = 3$ mice per group). Taken together these data, from multiple models of AD pathology and in WT animals, demonstrate that 40 Hz oscillations mitigate amyloid pathology, as measured by a reduction in Aβ levels, and reduce tau phosphorylation. Furthermore, 40 Hz visual flicker drives a distinct morphological transformation of microglia in both amyloidosis and tauopathy models of AD pathology.

Chapter 4: Conclusions

Summary of the thesis

Gamma oscillations reduce amyloid levels: Gamma oscillations have long been thought to be associated with higher cognitive functions and sensory responses.[27,41,76] We and others have previously shown that driving FS-PV-interneurons using optogenetic methods enhanced LFPs at 40 Hz in mice.[42] Here, we demonstrate that driving 40 Hz oscillations and phase locked spiking, using optogenetics or a non-invasive light flickering treatment in the 5XFAD mouse model, resulted in marked reduction of Aβ peptides in at least two different brain regions. This reduction was not due to decreased spiking activity because Aβ peptide levels were significantly lower in response to 40 Hz stimulation than to a random stimulation condition that produced similar amounts of multi-unit spiking activity without enhancing 40 Hz oscillations. Because our recordings and analysis did not distinguish between pyramidal cells and FS-PV-interneurons, we cannot exclude that pyramidal cell firing rates differed between these conditions but firing of FS-PV-interneurons or other cell types masked this change. However, random optogenetic stimulation of FS-PV-interneurons provided the same amount of direct stimulation of FS-PV-interneurons yet did not reduce amyloid. In fact, optogenetic stochastic stimulation more than tripled amyloid levels while stochastic visual flicker produced no significant change, which may indicate that some aspects of the random stimulation have neurotoxic effects. While random stimulation did not result in increased gamma power, we noticed a trend of small increases in power in a wide range of frequencies, from around 20 Hz to greater than 60 Hz. We also noticed a trend for increased amyloid levels with 20 Hz and 80 Hz light flicker. Taken together, these results suggest that driving activity at some frequencies below or above 40 Hz may increase

amyloid levels. These results point to a need to understand how patterns of spiking activity affect molecular pathways and disease pathology.

Mechanisms that contribute to reduction: The robust reduction of total amyloid levels is likely mediated by both decreased amyloidogenesis, involving reduced EEA1/Rab5-positive early endosomes, and increased endocytosis of amyloid by microglia. Importantly, our GSEA statistical analysis showed that the classical macrophage pro-inflammatory M1 or anti-inflammatory M2 cellular state did not correlate with either up- or down-regulated gene expression profiles following neuronal stimulation by 40 Hz oscillations. Indeed, the expression levels of pro-inflammatory genes *Il6, Il1b, Itgam* and anti-inflammatory gene *Igf1* were not changed after stimulation. Instead, a number of microglia pro-phagocytic genes as well as cell adhesion/migration regulator *Spp1* were activated upon 40 Hz stimulation. Thus, it appears that driving 40 Hz gamma oscillations induces an overall neuroprotective response by recruiting both neurons and microglia. The fact that $GABA_A$ antagonist treatment completely abrogated the effects of 40 Hz stimulation on reducing Aβ levels strongly suggests that GABAergic signaling, most likely involving FS-PV-interneurons, is critical for those effects.

The effect is not limited to a specific mouse model: Furthermore, 40 Hz flicker stimulation reduced Aβ in multiple mouse models including APP/PS1 and WT mice in addition to the 5XFAD mouse. This replication in multiple mouse models shows that these findings are not specific to one animal model and, importantly, extend to situations where APP is expressed by its physiological promoter and Aβ is generated from endogenous APP as in the WT animals. In addition, we found that 40 Hz oscillations reduced pTau in a mouse model of tauopathy, TauP301S, showing that the protective effects of gamma stimulation generalize not only to other mouse models but also to other pathogenic proteins. In summary, the findings reported in this

manuscript uncover previously unknown cellular and molecular processes mediated by gamma oscillations and establish a functional connection between brain gamma rhythms, microglia function, and AD-related pathology. While one must be cautious extending discoveries made in transgenic mice to humans, our findings of deficits in gamma oscillations converge with evidence of gamma deficits in different mouse models of AD (hAPP and apoE4),[26,45] and reports that gamma is altered in humans with AD.[46] By seeking converging evidence from multiple mouse models of AD, including transgenic and knock-in models, we can be assured that these results are not due solely to overexpression of transgenes or to other side effects particular to one model. Together these results from mice and humans show that multiple molecular pathways that contribute to Aβ pathology converge to alter gamma activity in AD.

Therapeutic potential

Our findings hold promise for a novel therapeutic intervention against AD, however further study is needed to determine whether driving gamma oscillations to reduce Aβ will be therapeutic. Broadly, a current prevailing theory of AD pathogenesis points to microglia malfunction, specifically microglia's failure to clear out pathological molecules, as a key mechanism of disease progression.[48] Therefore, interventions that recruit microglia back to an endocytotic state, as 40 Hz stimulation does, have strong therapeutic potential. We also note that driving gamma oscillations optogenetically or via light flicker did not cause neuronal hyperactivity (see **Ext. Data Fig. 1i** and **Ext. Data Fig. 4c**), in contrast to a recent report about immunotherapies that reduce Aβ in AD models.[59] It would also be important to determine how to use this approach to reduce AD pathology in other brain regions, like the hippocampus. Finally, it has yet to be determined if driving these patterns of activity will reduce AD pathology in

humans. And yet, because this approach is fundamentally different from prior AD therapies, we are cautiously optimistic that driving such patterned neural activity to trigger endogenous repair (or PaNThER) could provide a novel therapeutic approach to AD (**Figure 5a**).

Going forward

To extend the effects of gamma entrainment to regions outside VC: Future studies must determine the extent to which gamma entrainment can serve as an AD therapy. To begin, it will be important to determine the reach of 40 Hz sensory stimulation to other brain regions. In the current study, 1 hr of 40 Hz light flicker did not reduce hippocampal $A\beta_{1\text{-}40}$ and $A\beta_{1\text{-}42}$ levels (**Ext. Data Fig. 5f, g**). Because the hippocampus is required for many of the learning and memory tasks impaired in AD patients, any effective therapy will target hippocampus and other memory-associated parahippocampal regions, such as entorhinal cortex and subiculum. One potential strategy to extend the reach of 40 Hz entrainment is to use multi-modal sensory stimulation. It is well established in the literature that the hippocampus integrates sensory information from multiple sources (i.e. visual, auditory, tactile, etc.) in order to create a representation of context.[81,82] Therefore, a potential strategy to increase the range of the gamma entrainment effect on Aβ levels and reach deeper brain areas, such as the hippocampus, is to provide sensory stimulation of multiple modalities.

Elucidating temporal dynamics of the effect: Moreover, a better understanding of the temporal dynamics of the effect of 40 Hz light flicker will be informative in designing a therapy. First, although this study presents a timeline on the scale of hours for the acute effects of 40 Hz light flicker, better temporal precision may provide information on a point of maximal Aβ reduction. Second, although this study examined hippocampal effects after 1 hr of stimulation, it

Figure 5

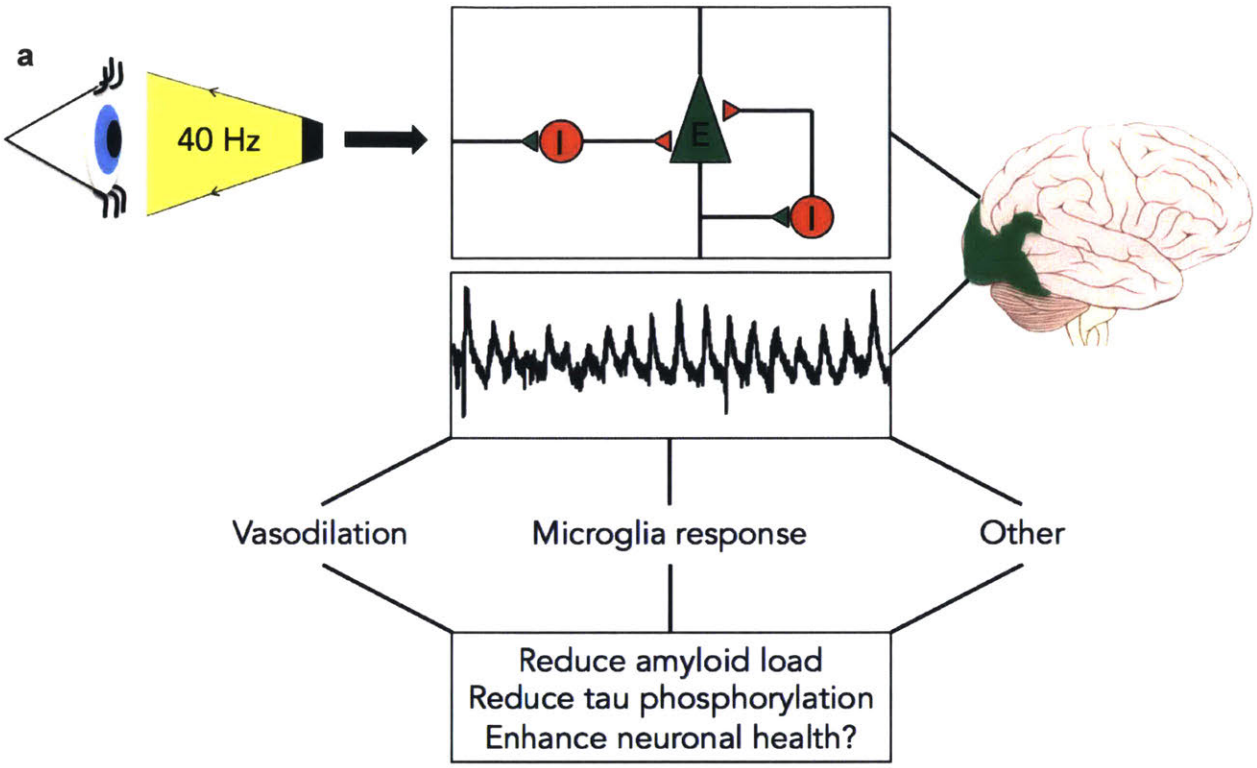

Figure 5: Patterned neural activity triggers endogenous repair (PaNThER)

a) Hypothetical model that shows that exposure to 40 Hz visual flicker engages the FS-PV (I) and excitatory (E) neurons of the visual cortex and drives the circuit at gamma. The gamma entrainment triggers various neural responses.

does not completely rule out the ability of 40 Hz light flicker to alter hippocampal Aβ. For example, perhaps the hippocampus is affected at 30 min but returns to baseline by 1 hr; or after 7 days of 1 hr stimulation, the hippocampus shows reduced Aβ levels. Finally, the ease of compliance with a treatment regimen directly correlates with the ease of adherence.[83] Therefore, if 40 Hz light flicker effectively reduces Aβ levels faster than the rate presented in this thesis (~50% with 1 hr daily treatment over 7 days), we can shorten daily treatment time and increase ease of adherence to the schedule. In short, further study of the temporal dynamics of the effects of gamma entrainment on Aβ levels will be useful to the design of a therapeutic strategy.

Two experimental techniques are available to investigate the timeline of the effect. First, pioneering work from the Holtzman laboratory developed an *in vivo* microdialysis technique to sample Aβ concentrations in the brain interstitial fluid (ISF) in awake mice.[30] Using this technique, we can sample ISF Aβ levels every 30 min for 3 days. Thus, *in vivo* micordialysis will allow us to determine a more temporally precise timescale of the 40 Hz entrainment effect across days. In addition, a new electrochemical tool developed by Yuede et al. at Washington University St. Louis called a microimmunoelectrode (MIE) samples Aβ levels every minute over 3 hr.[84] Using this technique, we can achieve the temporal precision to determine a maximal point of Aβ reduction that may occur faster than after 1 hr.

Investigating other cell types: Another important avenue of research to better understand the effects of gamma entrainment is to investigate effects on other cell types. In the current study, we showed that 1 hr 40 Hz optogenetic stimulation of FS-PV-interneurons and light flicker primed microglia to enter a pro-engulfment state that resulted in increased co-localization with Aβ (**Fig. 3d-h, Fig. 4d-h**). It is quite likely that other cell types that play a role in Aβ clearance are affected by gamma entrainment. For example, there is a wide body of literature that

implicates astrocytes in Aβ clearance. Astrocytes are the primary cell type that produces apolipoprotein E (ApoE), a protein that mediates cholesterol metabolism. In humans, there are three different alleles of *APOE* and the *ε4* allele markedly increases risk for AD. *APOE* is primarily expressed in astrocytes and has been shown to bind Aβ and mediate its entry into the bloodstream for clearance, which represents one method by which the brain removes Aβ. In addition, astrocytic end feet drive the flux of ISF within the glymphatic system, which moves solutes including Aβ out of the brain via brain vasculature.[16] Astrocytes are just one of many cell types likely affected by 40 Hz stimulation and that contribute to gamma's effect on Aβ levels.

To experimentally address these questions, we can combine FACS, sequencing, and confocal imaging techniques. First, we can purify neurons, astrocytes, microglia, oligodendrocytes, and endothelial cells from 5XFAD animals using FACS (Methods) following 1 hr of 40 Hz light flicker or dark control conditions and submit samples for RNA-seq. Next, using information provide from genome-wide gene expression analysis we can target specific genes and proteins affected by gamma entrainment to investigate the effects across all cell types. For example, we hypothesize that 40 Hz light flicker drives astrocytes of VC to promote ISF flow into enlarged vasculature via the glymphatic system and contribute to Aβ clearance; sequencing analysis will inform this hypothesis. Subsequent, immunohistochemical labeling and confocal imaging of astrocytes and affected vasculature will further explore this hypothesis on the protein and cellular levels. In short, future studies can build from the current study to fully elucidate gamma's molecular and cellular effects on the brain.

Final thoughts

The work presented in this study represents the beginning of a hopeful and exciting avenue of exploration. For years, investigation of AD was limited to the cellular and molecular realm. Recent endeavors to understand circuit level dysfunction associated with disease have been limited in scope; they do not connect traditional pathology, such as amyloid load, to the circuit effects observed. Here, we do just that: we modulate neural activity and observe the cellular and molecular outcome, revealing previously undiscovered connections between circuits and pathology. It is our hope that this work serves as a jumping off point, and that with open minds, we will continue to develop novel strategies to eventually prevent, halt, and cure AD.

Chapter 5: Methods

Animals. All animal work was approved by the Committee for Animal Care of the Division of Comparative Medicine at the Massachusetts Institute of Technology. Adult (3-month-old) male double transgenic 5XFAD Cre mice were produced by crossing 5XFAD transgenic mice with the transgenic PV or CW2 promoter driven Cre line. Adult (5-month-old) male and female APP/PS1 mice were gifted from the Tonegawa Laboratory. Adult (4-month-old) male TauP301S mice were obtained from the Jackson Laboratory. 9-month-old WT mice (C57Bl/6) were obtained from the Jackson Laboratory. Mice were housed in groups of 3-5 on a standard 12 hr light / 12 hr dark cycle, and all experiments were performed during the light cycle. Food and water were provided *ad libitum* unless otherwise noted. Littermates were randomly assigned to each condition by the experimenter. Experimenter was blind to animal genotypes during tissue processing and electrophysiological recording and analysis. No animals were excluded from analysis.

AAV vectors. Adeno-associated viral particles of serotype 5 were obtained from the Vector Core Facility at The University of North Carolina at Chapel Hill. The AAV5 virus contained a channelrhodopsin-2 (ChR2) fused to enhanced yellow fluorescent protein (EYFP) in a double-floxed, inverted, open-reading-frame (DIO) driven by the EF1α promoter (**Ext. Data Fig. 2a**). An AAV-DIO-EYFP construct was used as a control.

Surgical procedures. 3-month-old 5XFAD/PV-Cre or CW2 mice were anesthetized with an intraperitoneal (i.p.) injection of a mixture of ketamine (1.1 mg kg^{-1}) and xylazine (0.16 mg kg^{-1}). A small craniotomy was made 2.0 mm posterior to bregma and 1.8 mm lateral to the midline on

the left side. Virus was delivered through a small durotomy by a glass micropipette attached to a Quintessential Stereotaxic Injector (Stoelting). The glass micropipette was lowered to 1.2 mm below the brain surface. A bolus of 1 μL of virus (AAV-DIO-ChR2-EYFP or AAV-DIO-EYFP; 2 X 10^{12} viral molecules per ml) was injected into the CA1 region of hippocampus at 0.075 μL min^{-1}. The pipette remained in place for 5 min following the injection before being retracted from the brain. A unilateral optical fiber implant (300 μm core diameter; Thor Labs) was lowered to 0.9 mm below the brain surface about the injection site. Two small screws anchored at the anterior and posterior edges of the surgical site were bound with dental glue to secure the implant in place.

For electrophysiological recordings adult (3-month-old) male 5XFAD/PV-Cre and 5XFAD negative littermates (for CA1 recordings), or 5XFAD and their wild type littermates (for VC recordings) mice were anesthetized using isoflurane and placed in a stereotactic frame. The scalp was shaved, ophthalmic ointment (Puralube Vet Ointment, Dechra) was applied to the eyes, and Betadine and 70% ethanol were used to sterilize the surgical area. For CA1 recordings, a craniotomy (in mm, from bregma: -2 A/P, 1.8 M/L) was opened to deliver 1 μL of virus to CA1 (as described above). The target craniotomy site for LFP recordings was marked on the skull (in mm, from bregma: -3.23 A/P, 0.98 M/L for CA1 and 2.8 A/P, 2.5 M/L for VC), three self-tapping screws (F000CE094, Morris Precision Screws and Parts) were attached to the skull, and a custom stainless steel headplate was affixed using dental cement (C&B Metabond, Parkell). On the day of the first recording session, a dental drill was used to open the LFP craniotomies (300-400 μm diameter) by first thinning the skull until ~100 μm thick, and then using a 30 gauge needle to make a small aperture. The craniotomy was then sealed with a sterile silicone elastomer (Kwik-Sil WPI) until recording that day and in between recording sessions.

Optogenetic stimulation protocol. Two to four weeks following virus injection and implant placement (which provides time for the mice to recover and undergo behavior training for animals used for electrophysiology) and the virus to express in the neurons, CA1 neurons were optogenetically manipulated. A 200 mW 4793 nm DPSS laser was connected to a patch cord with a fiber channel/physical contact connector at each end. During the experiment, 1 mW (measured from the end of the fiber) of optical stimulation was delivered for 1 hr. For molecular and biochemical analyses, each animal received one of three stimulation protocols: 8 Hz, 40 Hz, or random stimulation (light pulses were delivered with a random interval determined by a Poisson process with an average frequency of 40 Hz). EYFP control animals received 40 Hz stimulation. For electrophysiological recordings each animal received all stimulation conditions interleaved during recordings.

Visual stimulation protocol. 15 minutes prior to the experiment 5XFAD mice were treated with saline (Control) or picrotoxin (0.18 mg/kg).[78] For molecular and biochemical analyses mice were then placed in a dark chamber illuminated by a light emitting diode (LED) bulb and exposed to one of five stimulation conditions: dark, light, 20 Hz, 40 Hz, 80 Hz flicker (12.5 ms light on, 12.5 ms light off, 60 W) for 1h . For electrophysiological recordings each animal received dark, light, 40 Hz flicker, or random (light pulses were delivered with a random interval determined by a Poisson process with an average interval of 40 Hz) stimulation conditions interleaved in 10 s blocks during recordings.

Behavior training and virtual reality environment (VR) for electrophysiology. For CA1 recordings, headfixed animals ran on an 8" spherical treadmill supported by an air cushion through a virtual reality environment, as described in Harvey et al.[85] The motion of the spherical treadmill was measured by an optical mouse and fed into virtual reality software[86], running in MATLAB (version 2013b, Mathworks). The virtual environment consisted of a linear track with two small enclosures at the ends where the animal could turn (**Ext. Data Fig. 1a**). Animals were rewarded with sweetened condensed milk (diluted 1:2 in water) at each end of the track for alternating visits to each end of the track.

Animals learned to run on the virtual linear track over approximately one week. The animals were left to recover from the surgery for one week, and habituated to handling for one to two days before behavioral training began. To learn to maneuver on the treadmill and get comfortable in the testing environment, on the first two days of training the animals were placed on the spherical treadmill with the virtual reality system off and were rewarded with undiluted sweetened condensed milk. On the second day of training on the spherical treadmill, animals' food was restricted to motivate them to run. Animals were restricted to no more than 85% of their baseline weight and typically weighed over 88% of their baseline weight. From the third day until the end of training (typically 5-7 days) the animals were placed on the treadmill for increasing amounts of time (30 min to 2 hr) running in the VR linear track. Animals were rewarded with diluted (1:2) sweetened condensed milk at the end of the linear track after traversing the length of the track. Between recording sessions, animals were given refresher training sessions to maintain behavioral performance.

For VC recordings, animals ran on the spherical treadmill while exposed to dark, light, or light flickering conditions (described below in data acquisition). Prior to recordings animals

learned to maneuver on the treadmill and get comfortable in the testing environment by being placed on the spherical treadmill (with the virtual reality system off) and receiving reward of undiluted sweetened condensed milk.

Electrophysiology data acquisition. For optogenetic stimulation of CA1 during recording, a 300 μm core optical fiber was advanced through the craniotomy used to deliver virus to CA1 to a depth of 900 μm into the brain. Light pulses that were 1 ms and 1 mW (measured from the end of the fiber) were delivered via a 473 nm DPSS (diode pumped solid state) laser (as described above).

To avoid photoelectric artifacts, neural activity was recorded with glass electrodes. LFP electrodes were pulled from borosilicate glass pipettes (Warner) on a filament-based micropipette puller (Flaming-Brown P97, Sutter Instruments), to a fine tip, which was then manually broken back to a diameter of ~10-20 μm and then filled with sterile saline. For CA1 recordings the LFP electrode was advanced through the LFP recording craniotomy at an angle 60 degrees posterior to the coronal plane and 45 degrees inferior to the horizontal plane until clear electrophysiological signatures of the hippocampal *stratum pyramidale* layer were observed (~600-1000 μV theta waves while the animal was running, clearly distinguishable sharp-wave ripples during immobility, and multiple spikes greater than 150 μV, **Ext. Data Fig. 1b**). For VC recordings the LFP electrode was advanced vertically through the LFP recording craniotomy to a depth of 600-900 μm and multiple spikes greater than 150 μV were observed.

Data was acquired with a sampling rate of 20 kHz and bandpass filtered 1 Hz-1 kHz. Animals ran on the spherical treadmill or rested for prolonged periods. For optogenetic simulation sessions, data was recorded for 30 minutes before any stimulation began. Then

stimulation was delivered at gamma (40 Hz), random (as described under *optogenetic stimulation protocol*), or theta (8 Hz) frequency for 10 s periods interleaved with 10 s baseline periods (no stimulation). In two animals, stimulation of each type or baseline was delivered for 5 min periods instead of 10 s periods. Each 30 minutes of stimulation recordings were followed by 5-30 minutes of recording with no stimulation. For visual light flicker simulation sessions, LED strip lights surrounding the animal lights were flickered at gamma (40 Hz), random (described above in *Visual stimulation protocol*), theta (8 Hz), or 20 Hz frequency for 10 s periods, or were on continuously for 10 s periods, interleaved with 10 s periods with lights off. A few recordings were made above the brain surface during light flicker to ensure that the lights did not create electrical or photoelectric noise during recording. Recording sessions were terminated after approximately 3-5 hr. Animals were 3-4 months old at the time of recording.

Analysis of electrophysiology recordings

Spike detection: Spikes were detected by thresholding the 300-6000 Hz bandpassed signal. Threshold was the median of the filtered signal plus five times a robust estimator of the standard deviation of the filtered signal (median/0.675) to avoid contamination of the standard deviation measure by spikes.[87]

Local field potential (LFP): Recorded traces were downsampled to 2 kHz and then bandpass filtered between 1 to 300 Hz.

Theta and SWR detection: Activity across the hippocampal network changes markedly when animals run or sit quietly and these changes are often referred to as different network states. These network states are clearly distinguishable by the presence or absence of LFP oscillations in different frequency bands[27,71]. When animals ran, we observed large theta (4-12 Hz) oscillations

in CA1 as others have shown (**Ext. Data Fig. 1b**, *left*)[71,85,88,89]. When animals sat quietly, theta oscillations were no longer visible and we recorded sharp wave ripples (SWRs), high frequency oscillations of 150-250 Hz that last around 50-100 ms and are associated with bursts of population activity, as others have observed (**Ext. Data Fig. 1b**, *right*)[37,38].

SWRs were detected (**Fig. 1a, b, c, d, Ext. Data Fig. 1d, e, f, g, h, i**) when the envelope amplitude of the filtered trace was greater than four standard deviations above the mean for at least 15 ms. The envelope amplitude was calculated by taking the absolute value of the Hilbert transform of the filtered LFP. We also confirmed our results held when using a higher threshold for SWR detection, 6 standard deviations above the mean, which detects larger SWRs (**Ext. Data Fig 1j, k**). To detect theta (**Ext. Data Fig. 1c, d**), the LFP was bandpass filtered for theta (4-12 Hz), delta (1-4 Hz), and beta (12-30 Hz) using an FIR equiripple filter. The ratio of theta to delta and beta ("theta ratio") was computed as the theta envelope amplitude divided by the sum of the delta and beta envelope amplitudes. Theta periods were classified as such when the theta ratio was greater than one standard deviation above mean for at least two seconds and the ratio reached a peak of at least two standard deviations above mean. Non-theta periods were classified as such when the theta ratio was less than one for at least two seconds. Sharp wave ripples, theta periods, and non-theta periods were visually inspected to ensure that these criteria accurately detected sharp wave ripple, theta periods, and non-theta periods, respectively.

Power spectrum: Spectral analysis was performing using multitaper methods (Chronux toolbox, time-bandwidth product = 3, number of tapers = 5). For examining power spectra without stimulation (**Ext. Data Fig. 1c, d**), only theta periods were included: theta periods greater than 5 s long were divided into 5 s trials and the average power spectral density was computed for each animal over these trials. For examining power spectra during optogenetic (**Fig. 1e, Ext. Data**

Fig. 1l) and visual stimulation (**Fig. 4a**, **Ext. Data Fig. 4a**), data was divided into 10 s trials of each stimulation condition or baseline periods, and the average power spectral density was computed for each animal over these trials.

Gamma during SWRs: Spectrograms were computed using multitaper methods (Chronux toolbox). The spectrogram was computed for each SWR including a window of 400 ms before and after the peak of the SWR. Then a z-scored spectrogram was computed in each frequency band using the mean and standard deviation of the spectrogram computed across the entire recording session to create a normalized measure of power in units of standard deviation (**Fig. 1a**, **Ext. Data Fig. 1e**). Instantaneous frequency of gamma during SWRs was computed by bandpass filtering the LFP for 10-50 Hz, taking the Hilbert transform, then taking the reciprocal of the difference in peaks of the transformed signal (**Fig. 1b**, **Ext. Data Fig. 1f**). Gamma power before, during, and after SWRs was computed by filtering the LFP for low gamma (20-50 Hz) and taking the amplitude of the envelope of the Hilbert transform to get the mean gamma power in 100 ms bins centered on the SWR peak. This was normalized by the mean and standard deviation of the amplitude of the envelope for the entire recording session to get z-scored gamma power for each bin around each SWR (**Fig. 1c, Ext. Data Fig. 1g, j**). Phase modulation by gamma during SWRs was computed by bandpass filtering the LFP for gamma (20-50 Hz), taking the Hilbert transform, and determining the phase of the resulting signal for each spike that occurred during SWRs (**Ext. Data Fig. 1h**). To measure differences in phase modulation between 5XFAD and WT animals, we used resampling with replacement: a subset of 100 spikes from each recording was randomly selected to create a phase modulation distribution and this was repeated 500 times for each recording (**Fig. 1d, Ext. Data Fig. 1k**). We then measured the depth of modulation for the spike-gamma phase distribution by computing the difference

between the peak and trough divided by the sum of the peak and trough for each distribution (**Fig. 1d, Ext. Data Fig. 1k**).

Differences in firing during stimulation: To plot stimulus-evoked multiunit firing histograms, spikes were binned in 2.5 ms bins for 100 ms after the start of each light on pulse and the fraction of spikes in each bin was computed. Mean and standard error was then computed across all light-on periods. To compute differences in multi-unit firing rate between conditions, firing rates were computed for each 10 s period of stimulation or baseline (total number of spikes divided by duration of period). Differences in firing rate were taken between nearby periods of the relevant type of stimulation (firing rate in gamma stimulation period minus baseline or random periods for optogenetic stimulation, firing rate in gamma stimulation period minus baseline, continuous on, or random periods for light flicker stimulation). Differences from all animals were plotted in histograms (**Ext. Data Fig. 1m**, **4c**) and the median and quartiles of the multiunit firing rates per 40 Hz stimulation, random stimulation, and no stimulation period for each animal were plotted in box plots (**Ext. Data Fig. 1o**, **4d**).

Immunohistochemistry. Mice were perfused with 4% paraformaldehyde under deep anesthesia, and the brains were post-fixed overnight in 4% paraformaldehyde. Brains were sectioned at 40 μm using a vibratome (Leica). Sections were permeabilized and blocked in PBS containing 0.2% Triton X-100 and 10% normal donkey serum at room temperature for 1 hr. Sections were incubated overnight at 4 °C in primary antibody in PBS with 0.2% Triton X-100 and 10% normal donkey serum. Primary antibodies were anti-EEA1 (BD Transduction Laboratories; 641057), anti-β-amyloid (Cell Signaling Technology; D54D2), anti-Iba1 (Wako Chemicals; 019-19741), anti-parvalbumin (Abcam; ab32895), anti-Rab5 (Enzo Life Sciences; ADI-KAP-GP006-

E). To confirm ELISA experiments, the anti-Aβ antibody D54D2 was used because it allowed for co-labeling with EEA1 and the anti A β antibody 12F4 was used because it does not react with APP allowing us to determine if our labeling was specific to Aβ. For co-labeling experiments, the anti-Aβ antibody 12F4 (Biolegend; 805501) was used. Primary antibodies were visualized with Alexa-Fluor 488 and Alex-Fluor 647 secondary antibodies (Molecular Probes), and cell nuclei visualized with Hoechst 33342 (Sigma-Aldrich; 94403). Images were acquired using a confocal microscope (LSM 710; Zeiss) with a 40X objective at identical settings for all conditions. Images were quantified using ImageJ 1.42q by an experimenter blind to treatment groups. For each experimental condition, 2 coronal sections from at least 3 animals were used for quantification. Scale bars are 50 μm. For CA1 imaging, the analysis was restricted to the pyramidal cell layer, except in the case of Iba1+ cells analysis, where the whole field of view was required to image an adequate number of cells. ImageJ was used to measure the diameter of Iba1+ cell bodies and to trace the processes for length measurement. In addition, the Coloc2 plugin was used to measure co-localization of Iba1 and Aβ. Imarisx64 8.1.2 (Bitplane, Zurich, Switzerland) was used for 3D rendering. For counting the "plaque number," deposits ≥ 10 μm were included.

Western blot. CA1 whole cell lysates were prepared using tissue from 3-month-old male 5XFAD/PV-Cre mice. Tissue was homogenized in 1 ml RIPA (50 mM Tris HCl pH 8.0, 150 mM NaCl, 1% NP-40, 0.5% sodium deoxycholate, 0.1% SDS) buffer with a hand homogenizer (Sigma), incubated on ice for 15 min, and rotated at 4 °C for 30 min. Cell debris was isolated and discarded by centrifugation at 14,000 rpm for 10 minutes. Lysates were quantitated using a nanodrop and 25 μg protein was loaded on a 10% acrylamide gels. Protein was transferred from

acrylamide gels to PVDF membranes (Invitrogen) at 100 V for 120 min. Membranes were blocked using bovine serum albumin (5% w/v) diluted in TBS:Tween. Membranes were incubated in primary antibodies overnight at 4 °C and secondary antibodies at room temperature for 90 minutes. Primary antibodies were anti-APP (Invitrogen; PAD CT695), anti-APP (Sigma; A8967), anti-β-actin (Abcam; ab9485). Secondary antibodies were horseradish peroxidase-linked (GE Healthcare). Signal intensities were quantified using ImageJ 1.46a and normalized to values of β-actin. We examined tau protein solubility using sequential protein extraction as described in Yoshiyama et al., 2007.[80] We then probed the detergent insoluble tau fraction using an antibody against Tau5 (Thermo Fisher Scientific; AHB0042).

ELISA. CA1 or VC was isolated from male mice, lysed with PBS or 5M Guanidine HCl, and subjected to Aβ measurement with the use of mouse (for WT experiments) or human (for all other experiments) $A\beta_{1\text{-}40}$ or $A\beta_{1\text{-}42}$ ELISA kit (Invitrogen) according to the manufacturer's instructions. We lysed the tissue in phosphate-buffered saline (PBS) to extract the PBS soluble Aβ fraction. The soluble Aβ fraction likely contained monomeric and oligomeric Aβ. Tissue was further treated with guanidine HCl to extract the insoluble Aβ fraction. $A\beta_{1\text{-}42}$ was below detectable levels for both flicker and control groups in WT VC and microglia-specific samples.

Genome-Wide RNA Sequencing. Total RNA was extracted from CA1 isolates using the RNeasy kit (Qiagen). Purified mRNA was used for RNA-seq library preparation using the BIOO NEXTflex™ kit (BIOO# 5138-08) per the manufacturer's instructions. Briefly, 1 μg of total mRNA was subject to a sequential workflow of poly-A purification, fragmentation, 1st flex

strand and 2nd strand synthesis, DNA end-adenylation, and adapter ligation. The libraries were enriched by 15 cycles of PCR reactions and cleaned with Agencourt AMPure XP magnetic beads (Beckman Coulter). The quality of the libraries was assessed using an Advanced Analytical-fragment Analyzer. The bar-coded libraries were equally mixed for sequencing in a single lane on the Illumina HiSeq 2000 platform at the MIT BioMicro Center. The raw fastq data of 50-bp single-end sequencing reads were aligned to the mouse mm9 reference genome using TopHat2.0. The mapped reads were processed by Cufflinks 2.2 with UCSC mm9 reference gene annotation to estimate transcript abundances, and test for differential expression. An average of 26,518,345 sequencing reads was obtained from 3 stimulated and 3 non-stimulated mice. Relative abundance of transcript was measured by Fragments Per Kilobase of exon per Million fragments mapped (FPKM). Gene differential expression test between treated and untreated groups was performed using Cuffdiff module with an adjusted p-value<0.05 for statistical significance (GEO accession: GSE77471).

To understand the cellular and molecular mechanisms from our RNA-seq data, 14 of publicly available RNA-seq datasets[90] were processed for cell-type specific analysis. Additionally, 60 publicly available neuron-, microglia-, and macrophage- specific RNA-seq datasets under different chemical and genetic perturbations[91–96] were downloaded and processed using TopHat/Cufflinks pipeline for gene set enrichment (GSEA) statistical analysis. GSEA was used to determine whether a defined gene set from our RNA-seq data is significantly enriched at either direction of a ranked gene list from a particular perturbation study. Genes detected in the public RNA-seq datasets were ranked by log2 values of fold change (case versus control), from positive to negative values. A defined gene set (in our case, up- or down-regulated genes upon gamma treatment) was considered significantly correlated with a perturbation-induced

transcriptomic change (either up- or down-regulation), when both nominal p-value and false discovery rate (FDR) q-value were less than 0.05. The sign of the calculated normalized enrichment score (NES) indicates whether the gene set is enriched at the top or the bottom of the ranked list. The heatmap for differentially expressed genes was generated using a custom R script, and z-score values across all libraries for each gene were calculated based on the gene FPKM values. The box plots for cell-type specificity analysis were also generated by R program, based on gene FPKM values.

Quantitative RT-PCR. The CA1 subregion was isolated from hippocampus of 3-month-old male 5XFAD/PV-Cre mice. Tissue was rapidly frozen using liquid nitrogen and stored at -80 °C, and RNA extracted using the RNeasy kit according to the manufacturer's protocol (Qiagen). RNA (3 μg) was treated with DNase I (4 U, Worthington Biochemical Corporation), purified using RNA Clean and Concentrator-5 Kit (Zymo Research) according to manufacturers' instructions and eluted with 14 μL DEPC-treated water. For each sample, 1 μg RNA was reverse transcribed in a 20 μL reaction volume containing random hexamer mix and Superscript III reverse transcriptase (50 U, Invitrogen) at 50 °C for 1 hr. First strand cDNAs were diluted 1:10 and 1 μL were used for RT-qPCR amplification in a 20 μL reaction (SsoFast EvaGreen Supermix, Bio-Rad) containing primers (0.2 μM). Relative changes in gene expression were assessed using the $2^{-\Delta\Delta Ct}$ method.

Isolation of microglia from VC. The primary visual cortex (V1 region) was rapidly dissected and placed in ice cold Hanks' Balanced Salt Solution (HBSS) (Gibco by Life Technologies, Catalog number 14175-095). The tissue was then enzymatically digested using the Neural Tissue

Dissociation Kit (P) (Miltenyi Biotec, Catalog number 130-092-628) according to the manufacturer's protocol, with minor modifications. Specifically, the tissue was enzymatically digested at 37 °C for 15 minutes instead of 35 minutes and the resulting cell suspension was passed through a 40 mm cell strainer (Falcon Cell Strainers, Sterile, Corning, Product #352340) instead of a MACS SmartStrainer, 70 mm. The resulting cell suspension was then stained using allophycocyanin (APC)-conjugated CD11b mouse clone M1/70.15.11.5 (Miltenyi Biotec, 130-098-088) and phycoerythrin (PE)-conjugated CD45 antibody (BD Pharmingen, 553081) according to the manufacturer's (Miltenyi Biotec) recommendations. Fluorescence-activated cell sorting (FACS) was then used to purify CD11b and CD45 positive microglial cells. The cells were sorted directly into 1XPBS (**Ext. Data Fig. 6a**).

Statistics. For electrophysiological data that was not normally distributed, results are presented as medians and quartiles unless otherwise noted. Two-sided Wilcoxon rank sum tests for equal medians were performed to determine if distributions were significantly different, and Wilcoxon signed rank tests were performed to determine if distributions were significantly different from zero as these do not assume data is normally distributed. Variability was similar between the groups that were statistically compared. The Bonferroni method was used to correct for multiple comparisons. No statistical method was used to estimate sample size, but it is consistent with previous publications.

Molecular and biochemical results are presented as mean + SEM. Percentages stated in manuscript are group means. All statistical analysis was performed using Prism GraphPad software. Normality was determined using the D'Agostino & Pearson omnibus normality test. Variability was similar between the groups that were statistically compared. Comparison data for

normally distributed data consisting of two groups was analyzed by two-tailed unpaired *t* tests. Comparison of data for normally distributed data consisting of three or more groups was analyzed by one-way ANOVA followed by Tukey's multiple comparisons test. Comparison data for non-normally distributed data was carried out using Mann Whitney tests. The statistical test, exact P values, and sample size (n) for each experiment is specified in the figure legend. For optogenetic ELISA data, two-sided unpaired Student's t-tests were performed to compare mice from the same litter that received different conditions. No statistical method was used to estimate sample size, but is consistent with previous publications. Molecular and biochemical analysis was performed using a minimum of three biological replicates per condition.

Chapter 6: Contributors to the thesis, References, and Extended Data Table 1

Contributions to the thesis

Hannah F. Iaccarino, Annabelle C. Singer, Emery N. Brown, Edward S. Boyden, and Li-Huei Tsai designed the experiments. Hannah F. Iaccarino and Fan Gao performed the whole-genome RNA sequencing experiments. Hannah F. Iaccarino and Annabelle C. Singer performed the electrophysiology experiments. Annabelle C. Singer analyzed the electrophysiology data. Hannah F. Iaccarino performed the optogenetics experiments. Hannah F. Iaccarino performed and analyzed the ELISA experiments. Tyler Z. Gillingham, Jinsoo Seo, and Oleg Kritskiy performed the western blots. Hannah F. Iaccarino, Andrii Rudenko, Fatema Abdurrob, Richard Rueda, and Rebecca G. Canter performed and analyzed the imaging experiments. Fan Gao analyzed the whole-genome RNA sequencing data. Hannah F. Iaccarino, Anthony J. Martorell, and Chinna Adaikkan performed the visual stimulation experiments. Hansruedi Mathys performed FACS experiments. Hannah F. Iaccarino, Annabelle C. Singer, Andrii Rudenko, Emery N. Brown, Edward S. Boyden, Li-Huei Tsai, Ram Madabhushi, Adam Bero, Jennie Young, Jay Penney, Christopher A. Deister, and Christopher I. Moore made significant intellectual contributions to the thesis.

References

1. Alzheimer's Association. Alzheimer's disease facts and figures. *Alzheimers Dement.* **10**, 1–80 (2014).

2. LaFerla, F. M. & Green, K. N. Animal models of Alzheimer disease. *Cold Spring Harb. Perspect. Med.* **2,** (2012).

3. Van Cauwenberghe, C., Van Broeckhoven, C. & Sleegers, K. The genetic landscape of Alzheimer disease: clinical implications and perspectives. *Genet. Med.* **18,** 421–430 (2016).

4. Hardy, J. & Selkoe, D. J. The Amyloid Hypothesis of Alzheimer's Disease: Progress and Problems on the Road to Therapeutics. *Science* **297,** 353–356 (2002).

5. Deane, R. *et al.* ApoE isoform-specific disruption of amyloid beta peptide clearance from mouse brain. *J. Clin. Invest.* **118,** 4002–4013 (2008).

6. Harold, D. *et al.* Genome-wide association study identifies variants at CLU and PICALM associated with Alzheimer's disease. *Nat. Genet.* **41,** 1088–1093 (2009).

7. Canter, R. G., Penney, J. & Tsai, L.-H. The road to restoring neural circuits for the treatment of Alzheimer's disease. *Nature* **539**, 187–196 (2016).

8. Huang, Y. & Mucke, L. Alzheimer Mechanisms and Therapeutic Strategies. *Cell* **148,** 1204–1222 (2012).

9. Iqbal, K., Liu, F., Gong, C.-X. & Grundke-Iqbal, I. Tau in Alzheimer disease and related tauopathies. *Curr. Alzheimer Res.* **7,** 656–664 (2010).

10. Min, S.-W. *et al.* Acetylation of tau inhibits its degradation and contributes to tauopathy. *Neuron* **67,** 953–966 (2010).

11. Cohen, T. J. *et al.* The acetylation of tau inhibits its function and promotes pathological tau aggregation. *Nat. Commun.* **2,** 252 (2011).

12. Braak, H. & Braak, E. Staging of Alzheimer's disease-related neurofibrillary changes. *Neurobiol. Aging* **16,** 271–278 (1995).

13. Hyman, B. T., Van Hoesen, G. W., Kromer, L. J. & Damasio, A. R. Perforant pathway changes and the memory impairment of Alzheimer's disease. *Ann. Neurol.* **20,** 472–481 (1986).

14. Mikkonen, M., Soininen, H., Tapiola, T., Alafuzoff, I. & Miettinen, R. Hippocampal plasticity in Alzheimer's disease: changes in highly polysialylated NCAM immunoreactivity in the hippocampal formation. *Eur. J. Neurosci.* **11,** 1754–1764 (1999).

15. Selkoe, D. J. *et al.* The role of APP processing and trafficking pathways in the formation of amyloid beta-protein. *Ann. N. Y. Acad. Sci.* **777,** 57–64 (1996).

16. Iliff, J. J. *et al.* A paravascular pathway facilitates CSF flow through the brain parenchyma and the clearance of interstitial solutes, including amyloid. *Sci. Transl. Med.* **4,** 1-11 (2012).

17. Hoover, B. R. *et al.* Tau mislocalization to dendritic spines mediates synaptic dysfunction independently of neurodegeneration. *Neuron* **68,** 1067-1081.

18. Zempel, H., Thies, E., Mandelkow, E. & Mandelkow, E.-M. Aβ oligomers cause localized Ca2+ elevation, missorting of endogenous tau into dendrites, tau phosphorylation, and destruction of microtubules and spines. *J. Neurosci.* **30,** (2010).

19. Morris, M., Maeda, S., Vossel, K. & Mucke, L. The many faces of tau. *Neuron* **70,** 410–426 (2011).

20. Tsai L. -H., Harlow E., Meyerson M. Isolation of the human cdk2 gene that encodes the cyclin A- and adenovirus E1A-associated p33 kinase. *Nature* **353,** 174–177 (1991).

21. Lee, M. *et al.* Neurotoxicity induces cleavage of p35 to p25 by calpain. *Nature* **405,** 360–364 (2000).

22. Otth, C. *et al.* AbetaPP induces cdk5-dependent tau hyperphosphorylation in transgenic mice Tg2576. *J. Alzheimer's Dis.* **4,** 417–430 (2002).

23. Cruz, J. C., Tseng, H.-C., Goldman, J. A., Shih, H. & Tsai, L.-H. Aberrant cdk5 activation by p25 triggers pathological events leading to neurodegeneration and neurofibrillary tangles. *Neuron* **40,** 471–483 (2003).

24. Heppner, F. L., Ransohoff, R. M. & Becher, B. Immune attack: the role of inflammation in Alzheimer disease. *Nat Rev Neurosci* **16,** 358–372 (2015).

25. Wang, Y. *et al.* TREM2 lipid sensing sustains the microglial response in an Alzheimer's disease model. *Cell* **160,** 1061–1071 (2015).

26. Verret, L. *et al.* Inhibitory interneuron deficit links altered network activity and cognitive dysfunction in Alzheimer model. *Cell* **149,** 708–721 (2012).

27. Buzsáki, G. *Rhythms of the brain.* (Oxford University Press, 2006).

28. Buckner, R. L. Molecular, structural, and functional characterization of Alzheimer's disease: evidence for a relationship between default activity, amyloid, and memory. *J Neurosci* **25,** 7709–7717 (2005).

29. Bero, A. W. *et al.* Neuronal activity regulates the regional vulnerability to amyloid-β deposition. *Nat. Neurosci.* **14,** 750–756 (2011).

30. Cirrito, J. R. *et al.* In vivo assessment of brain interstitial fluid with microdialysis reveals plaque-associated changes in amyloid-beta metabolism and half-life. *J. Neurosci.* **23,** 8844–8853 (2003).

31. Yamada, K. *et al.* In vivo microdialysis reveals age-dependent decrease of brain interstitial fluid tau levels in P301S human tau transgenic mice. *J. Neurosci.* **31,** 13110–13117 (2011).

32. Buzsáki, G., Logothetis, N. & Singer, W. Scaling brain size, keeping timing: evolutionary preservation of brain rhythms. *Neuron* **80,** 751–764 (2013).

33. Colgin, L. L. Rhythms of the hippocampal network. *Nat. Rev. Neurosci.* **17,** 239–249 (2016).

34. Markram, H., Gerstner, W. & Sjöström, P. J. A history of spike-timing-dependent plasticity. *Front. Synaptic Neurosci.* **3,** 4 (2011).

35. Belluscio, M. A., Mizuseki, K., Schmidt, R. & Kempter, R. Cross-rrequency phase – phase coupling between theta and gamma oscillations in the hippocampus. *Cell* **32,** 423–435 (2012).

36. Ylinen, A. *et al.* Sharp wave-associated high-frequency oscillation (200 Hz) in the intact hippocampus: network and intracellular mechanisms. *J. Neurosci.* **15,** 30–46 (1995).

37. Foster, D. J. & Wilson, M. A. Reverse replay of behavioural sequences in hippocampal place cells during the awake state. *Nature* **440,** 680–683 (2006).

38. Carr, M. F., Jadhav, S. P. & Frank, L. M. Hippocampal replay in the awake state: a potential substrate for memory consolidation and retrieval. *Nat. Neurosci.* **14,** 147–153 (2011).

39. Palop, J. J. *et al.* Aberrant excitatory neuronal activity and compensatory remodeling of inhibitory hippocampal circuits in mouse models of Alzheimer's disease. *Neuron* **55,** 697–711 (2007).

40. Bartos, M., Vida, I. & Jonas, P. Synaptic mechanisms of synchronized gamma oscillations in inhibitory interneuron networks. *Nat. Rev. Neurosci.* **8,** 45–56 (2007).

41. Fries, P., Nikolić, D. & Singer, W. The gamma cycle. *Trends Neurosci.* **30,** 309–16 (2007).

42. Cardin, J. A. *et al.* Driving fast-spiking cells induces gamma rhythm and controls sensory responses. *Nature* **459,** 663–7 (2009).

43. Sohal, V. S., Zhang, F., Yizhar, O. & Deisseroth, K. Parvalbumin neurons and gamma rhythms enhance cortical circuit performance. *Nature* **459,** 698–702 (2009).

44. Carr, M. F. F., Karlsson, M. P. P. & Frank, L. M. M. Transient slow gamma synchrony underlies hippocampal memory replay. *Neuron* **75,** 700–713 (2012).

45. Gillespie, A. K. *et al.* Apolipoprotein E4 causes age-dependent disruption of slow gamma oscillations during hippocampal sharp-wave ripples. *Neuron* 1–12 (2016).

46. Stam, C. J. *et al.* Generalized synchronization of MEG recordings in Alzheimer's disease: evidence for involvement of the gamma band. *J. Clin. Neurophysiol.* **19,** 562–574 (2002).

47. Prinz, M. & Priller, J. Microglia and brain macrophages in the molecular age: from origin to neuropsychiatric disease. *Nat. Rev. Neurosci.* **15,** 300–12 (2014).

48. Heneka, M. T., Kummer, M. P. & Latz, E. Innate immune activation in neurodegenerative disease. *Nat. Rev. Immunol.* **14,** 463–477 (2014).

49. Chitu, V. & Stanley, E. R. Colony-stimulating factor-1 in immunity and inflammation. *Curr. Opin. Immunol.* **18,** 39–48 (2006).

50. Boissonneault, V. *et al.* Powerful beneficial effects of macrophage colony-stimulating factor on -amyloid deposition and cognitive impairment in Alzheimer's disease. *Brain* **132,** 1078–1092 (2008).

51. Luo, J. *et al.* Colony-stimulating factor 1 receptor (CSF1R) signaling in injured neurons facilitates protection and survival. *J. Exp. Med.* **210,** 157–172 (2013).

52. Francis, P. T., Palmer, A. M., Snape, M. & Wilcock, G. K. The cholinergic hypothesis of Alzheimer's disease: a review of progress. *J. Neurol. Neurosurg. Psychiatry* **66,** 137–147 (1999).

53. Folch, J. *et al.* Current research therapeutic strategies for Alzheimer's disease treatment. *Neural Plast.* **2016,** 1–15 (2016).

54. Castello, M. A. *et al.* Moving beyond anti-amyloid therapy for the prevention and treatment of Alzheimer's disease. *BMC Neurol.* **14,** 169 (2014).

55. Imbimbo, B. P. *et al.* γ-secretase inhibitors and modulators for the treatment of Alzheimer's disease: disappointments and hopes. *Curr. Top. Med. Chem.* **11,** 1555–1570 (2011).

56. Wolfe, M. S. γ-secretase as a target for Alzheimer's disease. *Adv Pharmacol.* **64,** 127–153 (2012).

57. Doody, R. S. *et al.* A phase 3 trial of semagacestat for treatment of Alzheimer's disease. *N. Engl. J. Med.* **369,** 341–350 (2013).

58. Coric, V. *et al.* Safety and tolerability of the γ-Secretase inhibitor avagacestat in a phase 2 study of mild to moderate Alzheimer disease. *Arch. Neurol.* **69,** 1430–1440 (2012).

59. Busche, M. A. *et al.* Decreased amyloid-β and increased neuronal hyperactivity by immunotherapy in Alzheimer's models. *Nat. Neurosci.* **18,** 1725–1727 (2015).

60. Fuentes, P. & Catalan, J. A clinical perspective: anti tau's treatment in Alzheimer's disease. *Curr Alzheimer Res.* **8,** 686–688 (2011).

61. Wisniewski, T. *et al.* Immunotherapeutic approaches for Alzheimer's disease. *Neuron* **85,** 1162–1176 (2015).

62. Kanekiyo, T., Xu, H. & Bu, G. ApoE and Aβ in Alzheimer's disease: accidental encounters or partners? *Neuron* **81,** 740–754 (2014).

63. Liu, C.-C., Kanekiyo, T., Xu, H. & Bu, G. Apolipoprotein E and Alzheimer disease: risk, mechanisms, and therapy. *Nat Rev Neurol.* **9,** (2013).

64. Castellano, J. M. *et al.* Human apoE isoforms differentially regulate brain amyloid-β peptide clearance. *Sci. Transl. Med.* **3,** (2011).

65. Riddell, D. R. *et al.* The LXR agonist TO901317 selectively lowers hippocampal Aβ42 and improves memory in the Tg2576 mouse model of Alzheimer's disease. *Mol Cell Neurosci.* **34,** 621–628 (2007).

66. Chen, H.-K. *et al.* Small molecule structure correctors abolish detrimental effects of apolipoprotein E4 in cultured neurons. *J. Biol. Chem.* **287,** 5253–5266 (2012).

67. Butchart, J. *et al.* Etanercept in Alzheimer disease: a randomized, placebo-controlled, double-blind, phase 2 trial. *Neurology* **84,** 2161–2168 (2015).

68. Alzheimer's Association. Alzheimer's disease facts and figures. *Alzheimers Dement.* **12,** 1–84 (2016).

69. Oakley, H. *et al.* Intraneuronal β-amyloid aggregates, neurodegeneration, and neuron loss in transgenic mice with five familial Alzheimer's disease mutations: potential factors in amyloid plaque formation. *J. Neurosci.* **26,** 10129–10140 (2006).

70. Colgin, L. L. *et al.* Frequency of gamma oscillations routes flow of information in the hippocampus. *Nature* **462,** 353–357 (2009).

71. Buzsáki, G. *et al.* Hippocampal network patterns of activity in the mouse. *Neuroscience* **116,** 201–211 (2003).

72. Helwig, M. *et al.* The neuroendocrine protein 7B2 suppresses the aggregation of neurodegenerative disease-related proteins. *J. Biol. Chem.* **288,** 1114–1124 (2013).

73. Das, U. *et al.* Activity-induced convergence of APP and BACE-1 in acidic microdomains via an endocytosis-dependent pathway. *Neuron* **79,** 447–460 (2013).

74. Cataldo, A. M. *et al.* Endocytic pathway abnormalities precede amyloid beta deposition in sporadic Alzheimer's disease and Down syndrome: differential effects of APOE genotype and presenilin mutations. *Am. J. Pathol.* **157,** 277–286 (2000).

75. Gjoneska, E. *et al.* Conserved epigenomic signals in mice and humans reveal immune basis of Alzheimer's disease. *Nature* **518,** 365–369 (2015).

76. Gray, C. M., König, P., Engel, A. K. & Singer, W. Oscillatory responses in cat visual cortex exhibit inter-columnar synchronization which reflects global stimulus properties. *Nature* **338,** 334–337 (1989).

77. Eckhorn, R. *et al.* Coherent oscillations: A mechanism of feature linking in the visual cortex? *Biol. Cybern.* **60,** 121–130 (1988).

78. Pericic, D. & Bujas, M. Sex differences in the response to GABA antagonists depend on the route of drug administration. *Exp. Brain Res.* **25,** 187–190 (1997).

79. Jankowsky, J. L. *et al.* Mutant presenilins specifically elevate the levels of the 42 residue β-amyloid peptide in vivo: evidence for augmentation of a 42-specific β secretase. *Hum. Mol. Genet.* **13,** 159–170 (2004).

80. Yoshiyama, Y. *et al.* Synapse loss and microglial activation precede tangles in a P301S tauopathy mouse model. *Neuron* **53,** 337–351 (2007).

81. O'Keefe, J. & Dostrovsky, J. The hippocampus as a spatial map. Preliminary evidence from unit activity in the freely-moving rat. *Brain Res.* **34,** 171–175 (1971).

82. Frank, L. M., Brown, E. N. & Wilson, M. Trajectory encoding in the hippocampus and entorhinal cortex. *Neuron* **27,** 169–78 (2000).

83. Martin, L. R., Williams, S. L., Haskard, K. B. & Dimatteo, M. R. The challenge of patient adherence. *Ther. Clin. Risk Manag.* **1,** 189–199 (2005).

84. Yuede, C. M. *et al.* Rapid in vivo measurement of β-amyloid reveals biphasic clearance kinetics in an Alzheimer's mouse model. *J. Exp. Med.* **213,** 677–685 (2016).

85. Harvey, C. D., Collman, F., Dombeck, D. A. & Tank, D. W. Intracellular dynamics of hippocampal place cells during virtual navigation. *Nature* **461,** 941–946 (2009).

86. Aronov, D. & Tank, D. W. Engagement of neural circuits underlying 2D spatial navigation in a rodent virtual reality system. *Neuron* **84,** 442–456 (2014).

87. Rossant, C. *et al.* Spike sorting for large, dense electrode arrays. *Nat Neurosci* **19,** 634–641 (2016).

88. Buzsaki, G. Theta oscillations in the hippocampus. *Neuron* **33,** 325–340 (2002).

89. Ravassard, P. *et al.* Multisensory control of hippocampal spatiotemporal selectivity. *Science* **340,** 1342–1346 (2013).

90. Zhang, Y. *et al.* An RNA-sequencing transcriptome and splicing database of glia, neurons, and vascular cells of the cerebral cortex. *J. Neurosci.* **34,** 11929–11947 (2014).

91. Crotti, A. *et al.* Mutant Huntingtin promotes autonomous microglia activation via myeloid lineage-determining factors. *Nat. Neurosci.* **17,** 513–21 (2014).

92. Erny, D. *et al.* Host microbiota constantly control maturation and function of microglia in the CNS. *Nat. Neurosci.* **18,** 965–977 (2015).

93. Chiu, I. M. *et al.* A neurodegeneration-specific gene-expression signature of acutely isolated microglia from an amyotrophic lateral sclerosis mouse model. *Cell Rep.* **4,** 385–401 (2013).

94. Gosselin, D. *et al.* Environment drives selection and function of enhancers controlling tissue-specific macrophage identities. *Cell* **159,** 1327–1340 (2014).

95. Huang, S. C.-C. *et al.* Cell-intrinsic lysosomal lipolysis is essential for alternative activation of macrophages. *Nat. Immunol.* **15,** 846–855 (2014).

96. Yu, H. *et al.* Tet3 regulates synaptic transmission and homeostatic plasticity via DNA oxidation and repair. *Nat. Neurosci.* **18,** 836–43 (2015).

Extended Data Table 1

Treatment	Dilution Factor	Average $A\beta_{1-40}$ Concentration (pg/ml)	Average $A\beta_{1-42}$ Concentration (pg/ml)
Optogenetics			
PV-Cre EYFP	1:2	100.01, 61.598, 65.462, 82.509, 69.023, 70.831, 82.152, 74.314	58.777, 54.546, 30.585
PV-Cre 40 Hz	1:2	46.604, 31.041, 26.639, 55.612, 69.326, 17.711, 3.9951	27.271, 41.950, 18.790, 18.262
PV-Cre 8 Hz	1:2	101.268, 54.283, 90.190, 151.690	50.699, 122.85, 35.507
PV-Cre Random	1:2	235.68, 89.962, 157.37, 323.902, 451.78, 241.63	54.029, 137.78, 144.63
αCaMKII-Cre EYFP	1:2	45.813, 59.069, 40.404, 66.810	72.052, 36.573, 67.243, 59.295
αCaMKII-Cre 40 Hz	1:2	55.942, 44.270, 57.498, 47.382, 115.08, 75.673	70.847, 79.683, 61.429
αCaMKII-Cre 8 Hz	1:2	52.829, 46.604, 57.720	95.939, 21.640, 102.987
αCaMKII-Cre Random	1:2	218.00, 191.72, 159.07	66.203, 168.867, 176.404
Light flicker			
Dark 1 hr VC	1:2	343.8, 245.3, 210.6, 343.8, 588.4, 394.9, 123.3, 336.3, 328.2, 579.1, 420.0, 339.2	449.5, 320.7, 275.2, 449.5, 769.2, 516.2, 449.4, 320.6, 275.2, 449.4, 769.1, 516.1
Light 1 hr VC	1:2	366.9, 632.4, 378.2, 314.1, 266.9, 264.1	616.4, 592.3, 802.9, 394.5, 330.7, 337.8
20 Hz 1 hr VC	1:2	944.4, 313.2, 595.9, 530.0, 456.5, 289.9	1624, 302.4, 816.0, 687.2, 676.6, 343.0
40 Hz 1 hr VC	1:2	146.4, 143.6, 104.9, 99.6, 179.7, 219.8	191.4, 187.7, 137.2, 130.2, 234.9, 287.3
80 Hz 1 hr VC	1:2	332.5, 328.7, 363.5, 390.6, 530.0, 673.3	558.3, 418.9, 510.7, 609.5, 1186, 921.9
40 Hz + PTX 1 hr VC	1:2	367.2, 431.4, 445.2, 392.4, 386.7, 445.2	396.6, 540.5, 532.7, 705.0, 104.5, 104.5
Random 1 hr VC	1:2	461.8, 100.2, 9.819, 416.6	423.9, 157.9, 389.9, 841.5
Dark 1 hr HPC	1:2	97.949, 107.33, 119.92, 139.33	499.30, 355.13, 469.53, 598.03
40 Hz 1 hr HPC	1:2	88.136, 104.78, 161.52, 197.36	364.53, 408.41, 436.62, 873.83
Random 1 hr HPC	1:2	95.816, 136.77, 70.004, 125.47	466.39, 500.87, 311.26, 582.355
Dark 7 days soluble	1:50	1216.9, 1181.3, 1173.4, 1199.5, 134.73, 151.34, 113.26, 145.14, 127.91, 127.48, 143.02, 127.48, 141.07	5217.2, 8057.9, 9051.3, 6773.7, 244.11, 236.96, 235.38, 240.62, 286.19, 8.382, 11.21, 14.03, 13.56
Dark 7 days insoluble	1:100	1173.2, 1208.2, 1205.3, 1214.6, 994.86, 1059.2, 1176.6, 1065.4, 1002.9, 306.16, 690.70, 3442.7, 152.73	8572.7, 9127.1, 6349.3, 10138, 6852.2, 7056.7, 7039.7, 7094.2, 7289.0, 748.21, 1117.1, 1055.5, 504.95
40 Hz 7 days soluble	1:50	476.71, 283.83, 336.87, 237.22, 7.0175, 4.1480, 4.0580, 1.5205, 91.864, 152.73, 148.84, 141.07, 162.44	419.7, 248.1, 242.7, 90.974, 95.626, 56.936, 67.577, 47.586, 200.87, 13.56, 9.794, 15.44, 3.677
40 Hz 7 days insoluble	1:100	281.97, 270.37, 86.199, 239.71, 23.557, 15.166, 22.714, 1038.9, 1099.8, 1760.8, 1558.8, 187.69, 22.64	202.96, 130.71, 195.73, 193.70, 1646.89, 1579.1, 503.44, 1400.0, 7536.62, 955.23, 1208.8, 694.57, 784.91
Dark 1 hr BC	1:2	81.874, 18.343, 86.554	391.95, 883.69, 604.97
40 Hz 1 hr BC	1:2	81.307, 27.986, 30.113	300.34, 1152.5, 616.92
40 Hz 1 hr wait 4 hr	1:2	91.06, 141.8, 111.2, 12.30	108.0, 168.1, 157.3, 35.158
40 Hz 1 hr wait 12 hr	1:2	167.2, 101.6, 89.31, 119.9	236.1, 134.6, 124.8, 152.4
40 Hz 1 hr wait 24 hr	1:2	246.7, 177.6, 281.2, 175.0, 257.3, 204.2	231.8, 107.0, 402.7, 184.6, 245.1, 179.7
Dark APP/PS1	1:2	1050.16, 1085.25, 1522.45, 1153.69, 1750.77	19.22, 30.68, 28.08, 14.25, 25.30
40 Hz APP/PS1	1:2	512.42, 947.80, 850.45, 793.63	18.85, 15.58, 18.92, 11.44
Dark WT	1:1	0.038, 0.813, 2.016, 1.913, 0.313, 4.11, 7.23, 20.2, 40.4, 38.7, 11.9	N/A

Extended Data Table 1: Raw $A\beta_{1-40}$ and $A\beta_{1-42}$ concentrations

Table displaying raw $A\beta_{1-40}$ and $A\beta_{1-42}$ levels with ELISA dilution ratios for each experimental group. Equal tissue masses were compared for each ELISA experiment. For 7-day experiments, values were normalized to within litter controls such that raw values 1-4 in each condition were normalized to the mean of "Dark" values 1-4; raw values 5-9 in each condition were normalized to the mean of "Dark" values 5-9; raw values 10-13 in each condition were normalized to the mean of "Dark" values 10-13.

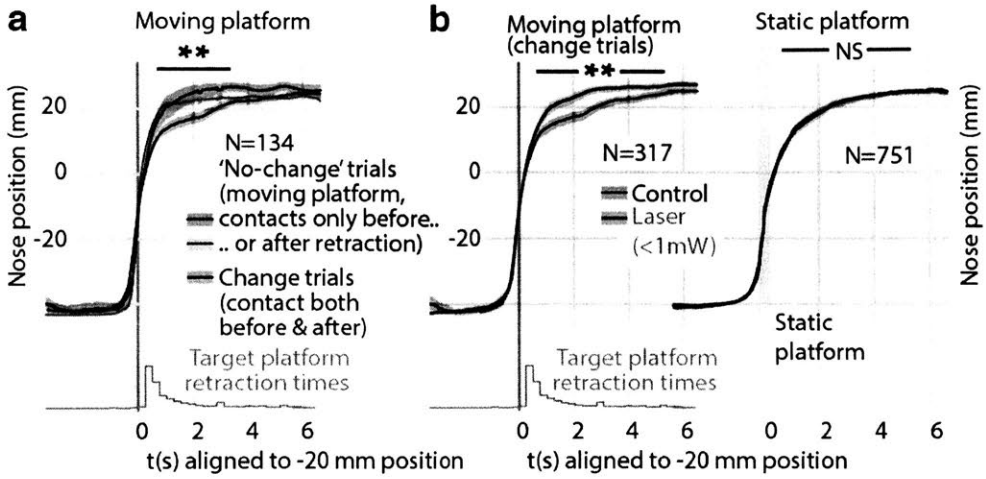

Figure 4-8: **Weak L6 drive selectively removes behavioural effect of small stimulus changes in free sensory behaviour. a**, When mice contacted the target before and after the retraction, they slowed their approach relative to trials in which they only contacted the target either only before or only after the platform retraction, presumably to re-locate the target more precisely after the change. **b**, Weak L6 drive abolishes this deceleration (left), but had no effect when the platform was static (right).

We tested if visible light stimulation itself would produce a significant effect by performing a series of sham controlexperiments in which light was directed not into the implanted ferrule, but directly onto the head of the mice. The experiments were run at ~10mW ensuring a significant higher degree of visible light than in the actual experiment. We found no significant effect of the sham stimulation in the retractying platfomr condition, and even observed a small decrease in crossing speed in the return direction Fig.4-9.

4.3.6 Effect of sensory gain modulation on change perception

We next examined whether the disruption of change detection was specific to the disruption of stimulus encoding in L6 and change encoding in L2/3 induced by weak L6 CT drive, or if any manipulation that disrupted stimulus encoding would also preferentially affect change detection.

In order to test the effect of moderate disruptions in stimulus encoding, we tested mice on the gap-crossing task under moderate L6 CT activation (>2mW power). As already outlined before, this optogenetic drive of L6 CT cells that moderately increases their firing rates is expected to lead to gain modulation throughout other layers via translaminar inhibition (Fig.3-2) (Olsen et al., 2012; Bortone et al., 2014). We first tested whether we could induce gain modulation similar to what was reposred in V1 (Olsen et al., 2012) in acute laminar recordings (see methods and Fig.3-2). In isoflurane anesthetized mice, laser powers of >1mW applied to the dura (leading to comparable spatial extent of ctivaiton, but corresponding to at least >2mW in the chronic setting where dura regrowth is expected

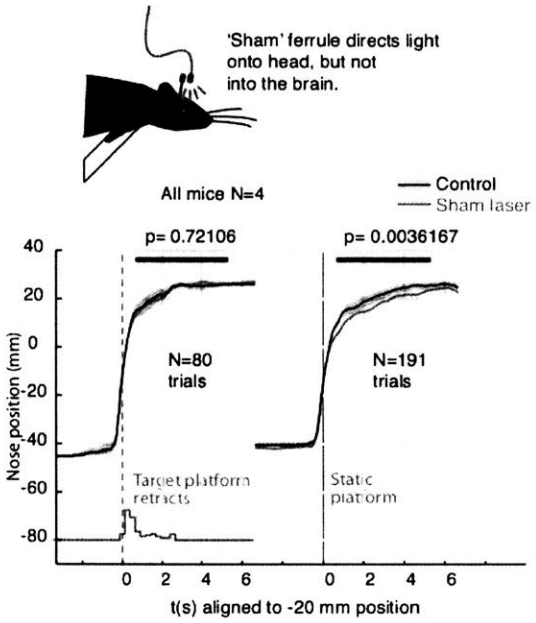

Figure 4-9: **Sham stimulation control.** Same as main gap-crossing experiment, but for sham-laser condition. Mice (N = 4) were tested as usual, but a 'sham' ferrule directed the laser light diffusely over the entire head of the animal instead of coupling it into the implanted ferrule. These control experiments were run with higher laser powers of ~10 mW to ensure that the light was always brighter and more visible to the animals than in the main experiment.

after 2 weeks) resulted in gain modulation, but did not completely remove sensory responses (Fig.4-10).

We then tested corresponding laser powers (~2-4mW) in the gap crossing task (N=4, subset of mice used in the gap crossing task) and first evaluated whether they resulted in a disruption of the basic sensory behaviour of the mice. We did not find any effect on the whisking pattern of the mice during free behaviour (Fig.4-11), suggesting that this manipulation was not significant enough to affect basic sensorimotor function.

However, we observed mild but non-specific sensory deficits as a result of this reduction in sensory gain, evident as a reduction of the overall likelihood of successful gap-crossing (defined as crossing after 5 sec after gap exploration, when whisker contact to the target platform occurred) from ~75% of successful attempts to ~ 50% ($P<0.01$, Fig.4-10). Importantly, the mice were still able to cross in half the trials, indicating that this manipulation led only to a relatively mild disruption of the sensory information available to the mice, as a complete removal of vibrissa information would have reduced the crossing probability to near zero (Hutson and Masterton, 1986; Celikel and Sakmann, 2007). In contrast, the weak L6 drive employed throughout the study led to selective failures to react to stimulus deviations, and to a slight increase in the crossing probability (Fig.4-10f, left).

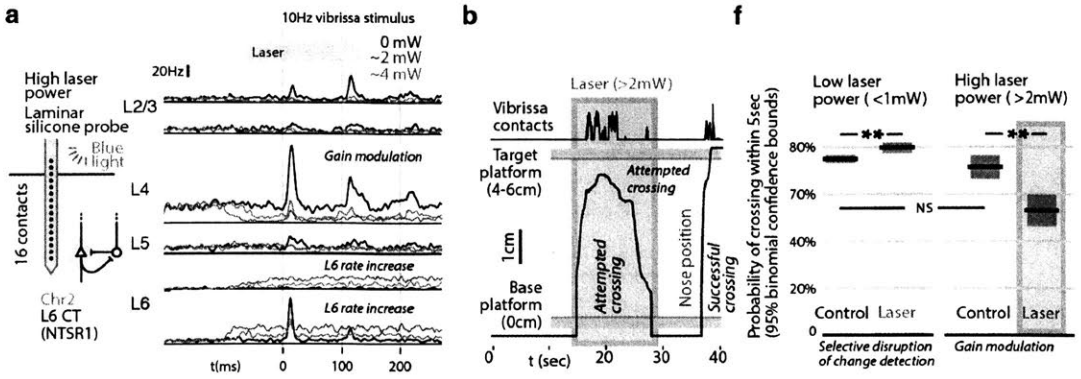

Figure 4-10: **Moderate gain-modulation impairs sensory behaviour. a**, In contrast to the weak L6 drive, stronger L6 stimulation drove L6 to higher rates, and reduced sensory gain in superficial layers, as in visual cortex (Olsen et al., 2012). Laser powers are shown for anesthetized acute experiments where an optical fiber was placed directly on the pia. **b**, During behavior, (N=514 trials) strong optogenetic drive non-specifically disrupted sensory behavior, **c**, making mice less likely to cross between the platforms (right). Weak L6 drive (as used throughout the rest of the study) did not have this nonspecific effect (left)

To conclude, I found that weak L6 CT drive that maintains firing rates but reduces the stimulus information carried in L6 and removes change encoding in L2/3 has no effect on performance in a basic stimulus detection task. The manipulation did however make it harder for mice to detect stimuli containing direcitonal deviants, which otherwise make stiuli more detectable. In a free, untrained sensory decision making behaviour, the weak L6 drive selectively abolished detection of sudden, small stimulus changes but did not affect behaviour in a static environment. These findings suggest a specific role of the stiulus encoding in L6 CT cells of primary sensory cotices in the perception of small sudden stimulus changes.

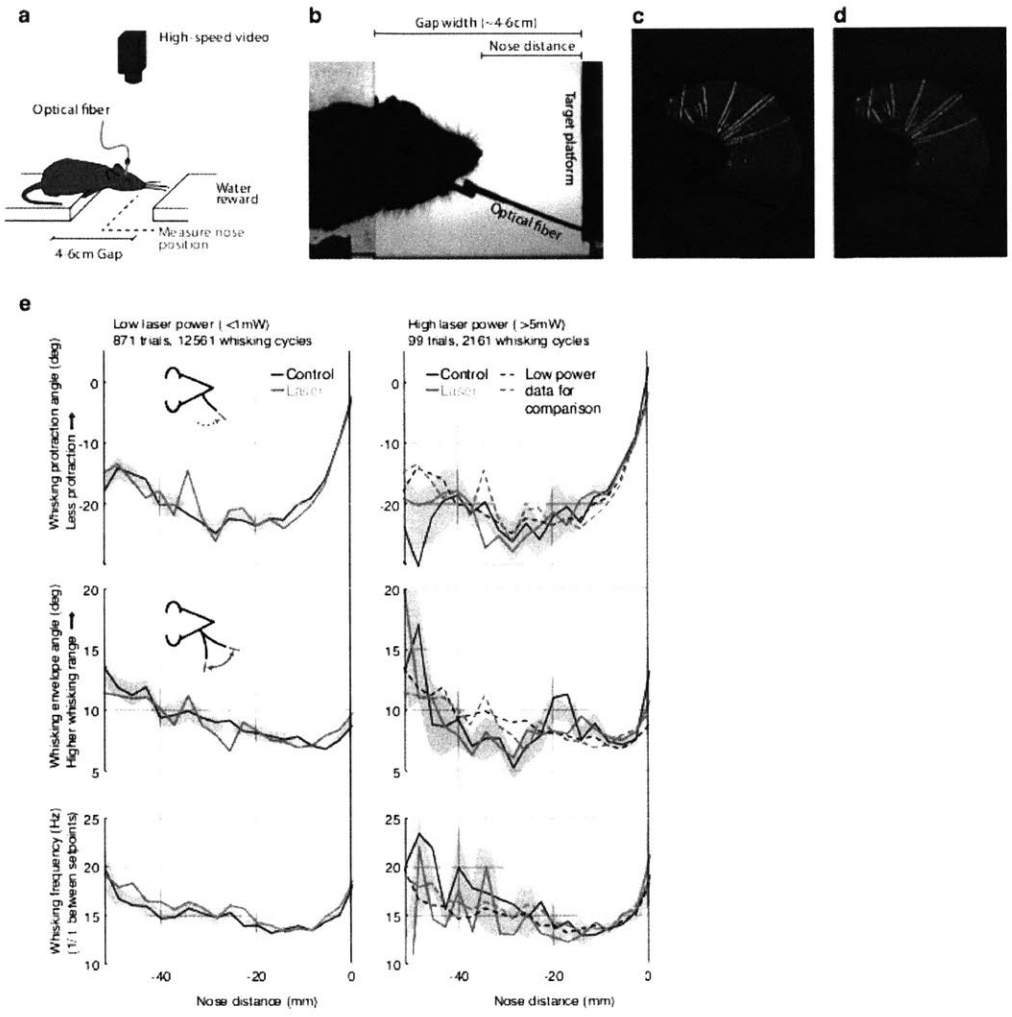

Figure 4-11: **Whisking pattern kinematics in the gap-crossing task are not impacted by laser stimulation.** Neither the low-power (< 1 mW) nor the high-power (> 5 mW) optogenetic L6 CT drive caused significant disruption of the sensorimotor whisking pattern in the gap-crossing task. **a**, Overview of setup for gap-crossing (Hutson and Masterton, 1986; Celikel and Sakmann, 2007; Voigts et al., 2008, 2015). **b**, Example raw image from gap-crossing experiment. **c**, Output of the convolutional neural network / vibrissa-identification stage of the vibrissa tracker . **d**, Same as panel c, but individual vibrissa segments are identified with a Hough transform. **e**, Vibrissa kinematics, resolved by nose-target platform distance (N = 4 mice with vibrissa tracking, 970 trials total) for the low-power ($< 1mW$ ChR2 drive) and high power (> 5mW) conditions. All plots are median and 95% confidence bounds for the median via bootstrapping. The low-power medians (left) are re-plotted as dotted lines in the high power condition (right). Top row: maximum protracted angle per vibrissa protraction cycle. Values closer to 0 correspond to smaller vibrissal protractions. Middle: Whisking pattern envelope amplitude (Hilbert-transform on 8–20 Hz filtered median whisker angle). Bottom: Whisking frequency computed from time between whisking pro/retraction setpoints. Data points above 30 Hz were excluded.

Bibliography

Antunes, F. M. and Malmierca, M. S. (2013). An Overview of Stimulus-Specific Adaptation in the Auditory Thalamus. *Brain Topography*, 27(4):480–499.

Bortone, D. S., Olsen, S. R., and Scanziani, M. (2014). Translaminar Inhibitory Cells Recruited by Layer 6 Corticothalamic Neurons Suppress Visual Cortex. *Neuron*, 82(2):474–485.

Celikel, T. and Sakmann, B. (2007). Sensory integration across space and in time for decision making in the somatosensory system of rodents. *Proceedings of the National Academy of Sciences*, 104(4):1395–1400.

Clack, N. G., O'Connor, D. H., Huber, D., Petreanu, L., Hires, A., Peron, S., Svoboda, K., and Myers, E. W. (2012). Automated Tracking of Whiskers in Videos of Head Fixed Rodents. *PLOS Comput Biol*, 8(7):e1002591.

Ferrington, D. G., Nail, B. S., and Rowe, M. (1977). Human tactile detection thresholds: Modification by inputs from specific tactile receptor classes. *The Journal of Physiology*, 272(2):415–433.

Goble, A. K. and Hollins, M. (1993). Vibrotactile adaptation enhances amplitude discrimination. *The Journal of the Acoustical Society of America*, 93(1):418–424.

Gyory, G., Berezovskii, V., Gordon, G., Perkon, I., Mitchinson, B., Grant, R., and Prescott, T. (2010). An algorithm for automatic tracking of rat whiskers. In *Proceedings of International Workshop on Visual Observation and Analysis of Animal and Insect Behavior (VAIB)*, volume 1-4, Istanbul.

Hollins, M. and Favorov, O. (1994). The Tactile Movement Aftereffect. *Somatosensory & Motor Research*, 11(2):153–162.

Hutson, K. A. and Masterton, R. B. (1986). The sensory contribution of a single vibrissa's cortical barrel. *Journal of Neurophysiology*, 56(4):1196–1223.

Jacobs, G. H., Fenwick, J. C., Calderone, J. B., and Deeb, S. S. (1999). Human cone pigment expressed in transgenic mice yields altered vision. *The Journal of Neuroscience: The Official Journal of the Society for Neuroscience*, 19(8):3258–3265.

Khatri, V. and Simons, D. J. (2007). Angularly nonspecific response suppression in rat barrel cortex. *Cerebral Cortex (New York, N.Y.: 1991)*, 17(3):599–609.

Knutsen, P. M., Derdikman, D., and Ahissar, E. (2005). Tracking whisker and head movements in unrestrained behaving rodents. *Journal of Neurophysiology*, 93(4):2294–2301.

Krauskopf, J. (1980). Discrimination and detection of changes in luminance. *Vision Research*, 20(8):671–677.

Krizhevsky, A., Sutskever, I., and Hinton, G. E. (2012). ImageNet Classification with Deep Convolutional Neural Networks. In Pereira, F., Burges, C. J. C., Bottou, L., and Weinberger, K. Q., editors, *Advances in Neural Information Processing Systems 25*, pages 1097–1105. Curran Associates, Inc.

Miyashita, T. and Feldman, D. E. (2013). Behavioral Detection of Passive Whisker Stimuli Requires Somatosensory Cortex. *Cerebral Cortex*, 23(7):1655–1662.

Müller, J. R., Metha, A. B., Krauskopf, J., and Lennie, P. (1999). Rapid adaptation in visual cortex to the structure of images. *Science (New York, N.Y.)*, 285(5432):1405–1408.

Musall, S., von der Behrens, W., Mayrhofer, J. M., Weber, B., Helmchen, F., and Haiss, F. (2014). Tactile frequency discrimination is enhanced by circumventing neocortical adaptation. *Nature Neuroscience*, 17(11):1567–1573.

Niemi, P. and Näätänen, R. (1981). Foreperiod and simple reaction time. *Psychological Bulletin*, 89(1):133.

O'Connor, D. H., Peron, S. P., Huber, D., and Svoboda, K. (2010). Neural Activity in Barrel Cortex Underlying Vibrissa-Based Object Localization in Mice. *Neuron*, 67(6):1048–1061.

Olsen, S. R., Bortone, D. S., Adesnik, H., and Scanziani, M. (2012). Gain control by layer six in cortical circuits of vision. *Nature*, 483(7387):47–52.

Sachidhanandam, S., Sreenivasan, V., Kyriakatos, A., Kremer, Y., and Petersen, C. C. H. (2013). Membrane potential correlates of sensory perception in mouse barrel cortex. *Nature Neuroscience*, 16(11):1671–1677.

Siegle, J. H., Pritchett, D. L., and Moore, C. I. (2014). Gamma-range synchronization of fast-spiking interneurons can enhance detection of tactile stimuli. *Nature Neuroscience*, 17(10):1371–1379.

Stüttgen, M. C. and Schwarz, C. (2008). Psychophysical and neurometric detection performance under stimulus uncertainty. *Nature Neuroscience*, 11(9):1091–1099.

Voigts, J., Herman, D. H., and Celikel, T. (2015). Tactile object localization by anticipatory whisker motion. *Journal of neurophysiology*, 113(2):620–632.

Voigts, J., Sakmann, B., and Celikel, T. (2008). Unsupervised whisker tracking in unrestrained behaving animals. *Journal of neurophysiology*, 100(1):504–515.

Wickelgren, W. A. (1977). Speed-accuracy tradeoff and information processing dynamics. *Acta psychologica*, 41(1):67–85.

Zhaoping, L. and Jingling, L. (2008). Filling-In and Suppression of Visual Perception from Context: A Bayesian Account of Perceptual Biases by Contextual Influences. *PLoS Computational Biology*, 4(2).

Chapter 5

Conclusions

5.1 Summary

Here we found that altering the sparse stimulus encoding in L6 CT with weak optogenetic drive disrupts encoding of stimulus deviants in L2/3 and selectively impairs perception of stimulus changes, without affecting overall firing rates or baseline sensory sensitivity. This suggests that sparse stimulus encoding in L6 is involved in the encoding and perception of unexpected stimuli in the laminar cortical circuit.

In Chapter 2, I described an improved implant design for large scale chronic tetrode recordings. Using this method, we found a clear laminar difference between the encoding of stimulus changes in Layers 4 and 2/3, allowing us to study the laminar emergence of stimulus history and change encoding. Using 2-photon imaging in L6 we found that even though L6 CT cells are very sparsely active, they encode stimulus content and could therefore play a role in the observed stimulus change encoding in superficial layers.

In Chapter 3, I described the finding that weak optogenetic drive of L6 CT cells results in re-weighting of neural activity in L6, where a subset of cells are driven, while others are suppressed, most likely due to the recruitment of FS interneurons in L6. This manipulation does not change overall firing rates in L6, but reduces the amount of stimulus information encoded by these cells. In L2/3, the manipulation selectively removes the encoding of stimulus deviations and history, making these cells instead represent the current stimuli with a faithful encoding that more closely mirrors their thalamic input.

In Chapter 4, I described two independent behavioural experiments that show that the manipulation of L6 encoding results in specific perceptual and behavioural deficits: in a head-fixed threshold stimulus detection task the weak L6 drive removed the benefit of small stimulus deviations, without affecting detection rates of non-changing stimuli. Analogously, in a gap-crossing task that tests unrestrained sensory decision making behavior, the manipulation selectively impaired perception of small, sudden stimulus changes, without affecting basic sensory performance. I also showed that induction of sensory gain reduction with stronger L6 drive impaired tactile sensitivity.

5.2 What do these findings teach us about the role of L6

This thesis provides evidence that the specific stimulus encoding in L6 CT cells, not just the maintenance of stimulus driven firing rates, plays a causal role in the emergence of tempo-spatial receptive fields (RFs) in L2/3 RS cells from more faithful RFs in L4 and thalamus, and that this encoding of stimulus changes is behaviourally relevant in the perception of sudden small stimulus changes. I studied the adaptation of neocortical circuits to specific inputs, and the subsequent explicit representation of deviations, at the level of the basic laminar neocortical circuit. I used the encoding and perception of of very simple stimulus changes as as tool to probe the implementation of this basic computation, specifically the role of stimulus encoding by cortical layer 6 CT cells, in the context of simple sensory behaviours in mice. L6 CT cells and their role on the encoding of changes in the local laminar circuit are particularly interesting from a computational perspective because in addition to local dynamics, L6 provides a substrate for integration of long-range inputs (cortico-cortical and other) with local information.

Our results on the sparsity of vibrissa stimulus driven L6 CT cells fits nicely with results of highly specific direction tuning in these cells in V1 (Vélez-Fort et al., 2014), suggesting that part of the sparsity of the responses in our study could be due to the choice of one set of stimulus parameters. If for instance the same finding of higher specificity of direction tuning of L6 CT cells relative to other layers in V1 applies to S1, then our choice of one deflection direction and variation in amplitude would explain the sparse responses we observed for these cells. However, our finding that direction tuning in L6 CT cells seems not to be very specific (even though this finding is limited due to the sparsity of L6 firing and our use of only 2 deflection directions) suggests that the V1 results can not be mapped to S1 completely analogously, as is expected from the relatively lower prevalence of clear direction tuning in mouse S1 (Clancy et al., 2015; Andermann and Moore, 2006; Peron et al., 2015) opposed to V1 (Niell and Stryker, 2008). It remains to be seen if possibly a higher percentage of L6 CT cells could be driven by well chosen stimuli if wider space of stimuli is investigated, especially if stimuli with a stronger center-surround structure, which are implied in L6 function (Bolz and Gilbert, 1986), are utilized. Similarly, it seems reasonable that L6 CT encoding would be modulated substantially by the whisking pattern of the mouse, because this whisking pattern is correlated with both stimulus history, as well as stimulus expectation (Voigts et al., 2015) (as described in the next section). In sum, even though our simple vibrissa stimuli were able to elicit an interpretable stimulus response in L6 CT cells that is in line with previous results, we would expect a more thorough engagement of these neurons in tasks and stimuli that involve stronger statistical dependencies between neighboring and/or preceding inputs.

The key manipulation used in this thesis, weak optogenetic drive of L6 CT cells with ChR2 in the NTSR1 cre line (Gong et al., 2007) can be contrasted with a superficially similar manipulation used in a series of studies in cortical gain modulation: In these studies, significantly stronger drive of L6 CT cells, using the same cre line as used in this thesis, drives increased L6 firing rates and reduces sensory gain in superficial layers (Olsen et al., 2012), predominantly due to recruitment of trans-laminar inhibition from FS inhibitory neurons in L6 that inhibit neurons throughout the entire cortical column (Bortone et al., 2014).

Here, we found that similarly strong (albeit likely still somewhat weaker, ~5mW sus-

tained total power at pia) drive of L6 CT cells with Chr2 in the NTSR1 line results in comparable gain modulation of vibrissal responses in S1 of lightly anesthetized mice (Fig.4-10). This provides some indirect evidence that the overall circuit mechanism surrounding L6 that we observe in S1 are at least roughly preserved in V1. We further verified that this modulation (even when applied in relatively moderate amplitudes that should retain substantial sensory responses) affects sensory performance in the gap-crossing task (Fig.4-10), without altering sensorimotor function enough to affect the whisking pattern (Fig.4-11). This finding provides a good verification that the gain modulation previously reported in (Olsen et al., 2012) is behaviourally relevant, and also provides evidence that per-trial disruptions of the tactile information in the gap-crossing task lead to immediate behavioural deficits, underlying the notion that mice integrate tactile information in this task and make decisions as soon as they have accumulated enough evidence to locate the target. This is contrasted by the finding that chronic (~days) degradation of the sensory information available to mice by vibrissa-trimming reduces only the speed of their decision making process, but not the success rate (Celikel and Sakmann, 2007). It might be interesting to investigate if more chronic gain manipulation could similarly be behaviourally compensated by mice.

More importantly than recapitulating prior findings in V1, the gain modulation experiments in this study provide a control condition that allowed us to test whether any manipulation that disrupted stimulus encoding in S1 would preferentially affect change detection, or whether the observed shuffling of L6 encoding is required to achieve a change-specific behavioural effect that does not impair sensory processing of stimuli that do not contain unexpected outliers.

Another line of evidence for the specificity of the role of L6 comes from a recent study, also in in mouse S1, where a similar optogenetic strategy, albeit *hyper*-polarization via ArchT of apical dendrites was used in L5 pyramidal cells (Nattar Ranganatha et al., 2014) was examined: In this study, silencing of L5 apical dendrites disrupted mices' ability to modulate their whisking pattern which would be expected to significantly impair their ability to perform complex sensory tasks such as gap-crossing. The observation of no such impairment for weak L6 activation in this study shows a clear difference of the functional roles of L5 and L6 cells using subtle disruptions in their firing patterns. Similarly, our findigs show a clear contrast to the modulation of baseline sensory performance by weak drive of FS cells (Siegle et al., 2014; Sachidhanandam et al., 2016). These differences suggest that L6 plays a distinct role in processing stimulus changes, and that the same specificity of disrupting only the processing of changing stimuli can likely not be achieved by disruption of stimulus encoding in other cortical layers or cell types.

One of the key mechanisms that we observed in this study was that weak drive of L6 CT cells did not affect overall L6 firing rates (Fig.3-3,3-4). This finding is consistent with the very low baseline, as well as surprisingly stable stimulus evoked firing rates in L6 over a variety of stimulus conditions (Vélez-Fort et al., 2014; Thomson, 2010; Marx and Feldmeyer, 2013). This finding supports the idea that the recurrent, high fan-out connectivity of L6 CT pyramidal cells to their local inhibitory network (a feature that is not shared by their CC counterparts) (Mercer et al., 2005; West et al., 2006) implements a mechanism that keeps overall L6 rates constant regardless of the overall afferent drive. This idea is supported by the significantly stronger FS than CT activation that we observed in L6 under weak CT drive (Fig.3-3) and the immediate, strong activation of L6 FS cells by pulsed CT activation,

even in the absence of significant CT activation (Fig.3-1).

Another aspect of the weak L6 drive employed here that is worth discussing separately is that the weak superficial activation of deep neurons has the potential to not only bias the activity of the neural ensemble on a per-neuron level, but could also bias the relative contribution of different dendritic compartments within individual neurons: If the loss of light power in deeper tissue causes superficial dendrites of neurons to be preferentially subjected to the optogenetically driven depolarization, this could affect the susceptibility of this neuron to specific inputs but not others, and change the response properties of that neuron way beyond simple firing rate changes, including disruption of coincidence detection mechanisms (Larkum et al., 1999; Xu et al., 2012). This dendritic coincidence detection mechanism has recently been shown to underly the sensorimotor computations in mouse S1 (Xu et al., 2012; Harnett et al., 2013), and could be selectively disrupted using a similar, predominantly superficial optogenetic hyperpolarization via Archaerhodopsin-T (Nattar Ranganatha et al., 2014). However, the approach taken in this study can likely not be mapped directly to the one used here, even though the light fall-off from superficial broad light delivery is likely similar. Our observation of increases L6 CT firing rates after weak Chr2 drive, and recruitment of some L6 FS activity suggests that at least a small number of L6 CT were directly activated by our manipulation. It is however entirely possible that the observed changes in the responses of L6 CT to sensory stimuli (Chapter 3.4) are accompanied by a change in the input-output response of individual L6 CT cells driven by a preferential depolarization of the more superficial dendrites of these cells.

At first glance, the stimulus change encoding in L2/3 appears relatively sparse and non-informative. How much information do we expect the animal to be able to extract from the spiking of these cells? The observed encoding in L2/3 corresponds to a median difference of spike counts of at least $\sim$0.03 spikes per deflection between small increases and small decreases in stimulus amplitude (which were chosen to be within a relatively realistic range occurring in natural behaviour (Voigts et al., 2008)). For a 700ms stimulus at 10Hz (as used here, and similar to naturally occurring whisking frequencies) this corresponds to $\sim$70 spikes per vibrissa, or 250–1000 spikes extrapolated across a typical bout of whisking in sensory decision making ((Celikel and Sakmann, 2007), Fig.5-1). This consideration shows that the code in L2/3, though sparse and stochastic at the level of individual cells and at individual vibrissa deflections, is robust in terms of being behaviourally relevant.

How could L6 CT cells affect the stimulus encoding in superficial layers and how do our findings relate to current models of the relationship between L6 activity and stimulus encoding? Individual components of the L6 circuit have been identified - local inhibition within L6 (Zhang and Deschênes, 1997) that regulates L6 firing rates in response to our optogenetic drive of CT neurons, as well as translaminar-projecting FS neurons (Bortone et al., 2014) that can cause significant gain modulation throughout superficial layers, as well as corticothalamic mechanisms (Thomson, 2010) of L6-mediated modulation of sensory responses are known. However, the specific mechanisms by which the stimulus encoding in L6 influences state or stimulus encoding in superficial layers are still largely unknown at a level of description that would allow us to relate it to the findings described in this thesis. The relative contributions of the large range of direct efferents from L6 to superficial layers (Wiser and Callaway, 1996, 1997; Callaway, 1998) is especially hard to interpret in the context of very sparse sensory activity in L6. Further, the findings that modulation

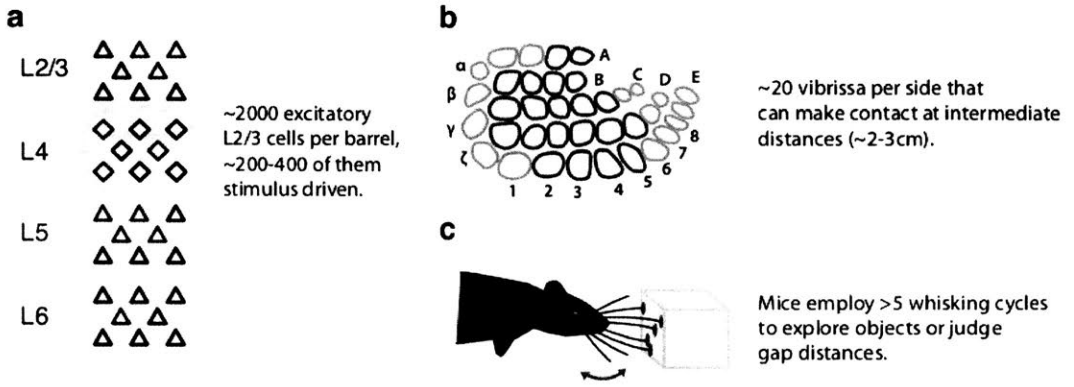

Figure 5-1: **Estimated impact of sparse encoding of stimulus details on behavioral detectability.** Neurons in L2/3 represent stimulus changes with changes in their spiking probability, termed (Fig.2-12). Individual neurons had values of < 0.1 mean difference in spikes per deflection, for the small range of stimulus deviants (around $\pm 10 - 15\%$ relative to baseline) used in this study. This small range of deviants was chosen to replicate the naturally occurring range of stimulus deviations that a mouse would experience when lightly touching a tactile scene (Ritt et al., 2008; Voigts et al., 2008; Grant et al., 2009; Sherman et al., 2013). **a**, There are $\sim$2000 L2/3 neurons in each S1 barrel (Lefort et al., 2009), around 15% of which are stimulus driven (Peron et al., 2015; Crochet et al., 2011), or $\sim$300. A conservative mean spike count difference between deviants of $\sim$0.03 spikes per neuron per whisker per deflection (seen in the interquartile range of the change coefficients across the population, Fig.2-12), will lead to $\sim$10 excess or deficient spikes across L2/3 per barrel per deflection, a difference within a behaviorally relevant range of neural activity (Houweling and Brecht, 2008). **b**, In free behavior, mice make contact with objects using 5–20 principal vibrissae, resulting in an estimate of 50–200 spikes mean difference between stimuli in unilateral S1. **c**, During free whisking, mice contact objects over > 5 whisking cycles across both sides of their face before making a decision (Celikel and Sakmann, 2007), which gives an estimate of a total integrated difference of 250–1000 spikes between baseline and deviant stimuli for one typical decision making process, or twice that assuming bilateral vibrissa contact, assuming a spike count difference/change coefficient of 0.03 per stimulus driven cell per deflection. This estimate seems reasonable given the distribution of change coefficients in L2/3 (Fig.2-12). This argument depends on what neurally encoded information is actually used by animals, but we believe that the encoding that we observed should be qualitatively similar to that used by freely behaving mice.

of thalamic transmission by L6 across distant cortical areas can have a significant effect on stimulus encoding in sensory areas (Lee et al., 2008) complicates the interpretation of correlative findings in the context of circuitry. Our findings therefore can not currently be interpreted in the context of a specific circuit mechanism that directly links the sensory representations in L6 to those in L2/3, and future studies are required to determine the circuit, synaptic and cellular mechanisms by which L6 affects neural encoding and behavior.

Even though the majority of experiments described here were carried out with amplitude deviations that elicit a clearly cortically emerging (present in L2/3, not in L4) change encoding, we observed a similar removal of change encoding by L6 drive for directional deviants (Fig.3-13). This shows that even though the directional novelty encoding could arise from partially thalamic, or thalamocortical stimulus-specific adaptation mechanisms (Movshon and Lennie, 1979; Khatri and Simons, 2007), the weak L6 drive at least partially suppresses the effect of this adaptation at the level of the L4>L2/3 synapses.

In sum, our findings are consistent with previous findings about the function of L6 in awake behaving animals, but suggest that the previously reported, highly selective sensory encoding by L6 CT cells plays a specific role in the generation of explicit change encoding in L2/3, and in the perception of stimulus changes.

5.3 Implications for models of canonical cortical computation

The findings described in this thesis allow us to draw a few specific conclusions about the role of stimulus encoding in L6 for general properties of cortical computation.

Even though weak L6 CT drive did not affect stimulus driven firing rates, it changed which L6 CT neurons were sensory driven (Fig.3-4, Fig.3-5). This finding indicates that a sparse set of active neurons in L6, with specific connectivity, is required for deviance encoding (Fig.5-2). There are two basic mechanisms by which this manipulation could lead to the observed disruption of change encoding in L2/3. The population of L6 cells active in the laser condition is different from the one active in the control condition. This shuffling alone could lead to a disruption of stimulus representation in L2/3 because the activity of the active L6 population are now decoded differently by their recipient layers. Additionally, we found that the population of L6 CT cells that is active in the laser condition carries less stimulus information than the population that is active in the control condition (Fig.3-6, Fig.3-8), so any decoding of stimulus information from L6 is expected to be impaired.

We found that the weak L6 drive employed here had no effect on RS firing rates in L6 and in superficial layers (Fig.3-3). The manipulation also had no effect on threshold level stimulus detection (Fig.4-3), or unrestrained sensory behavior (Fig.4-8) as long as no sudden small stimulus changes were presented. In contrast, moderate L6 drive that led to suppressive gain modulation disrupted sensory behavior non-specifically (Fig.4-10). This suggests that the specific stimulus encoding in L6 CT cells is required for encoding and detection of stimulus changes. This is consistent with the finding that small changes of sensory evoked firing rates in other cortical layers induced via drive of PV+ interneurons

(Siegle et al., 2014; Lee et al., 2012; Sachidhanandam et al., 2013) lead to non-specific changes of stimulus encoding and affect detection behavior on all stimuli.

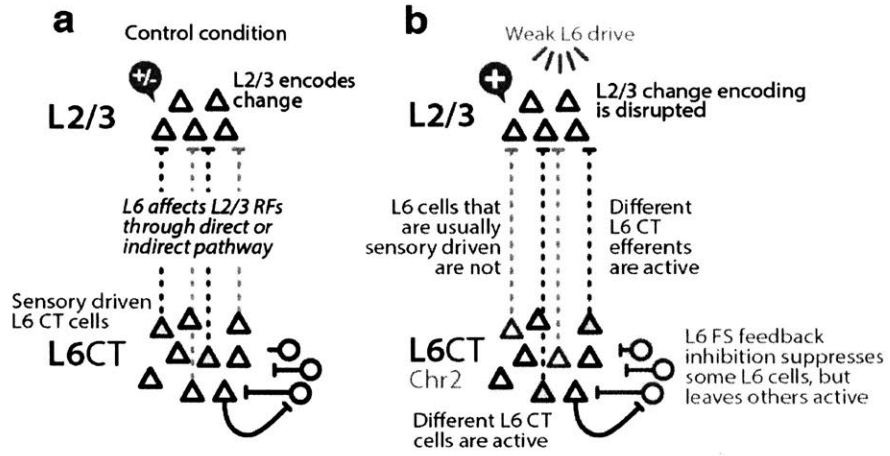

Figure 5-2: **A mechanism for how stimulus encoding in L6 CT cells can lead to the observed change representation in L2/3 and how weak optogenetic drive of L6 CT cells disrupted this encoding.** **a**, During normal sensory function, a small subset of L6 CT cells are sensory driven. Through several potential pathways, this specific ensemble of L6 CT comes to have a specific impact on the emergence of heterogeneous change encoding in L2/3 RS. **b**, Under weak optogenetic drive of L6 CT, the exact ensemble of L6 CT activated by sensory drive is changed, with the emergence of new neurons and the suppression of previously activated cells. This transformation is likely in part mediated by later inhibition through L6 FS cells (Olsen et al., 2012; Bortone et al., 2014; Zhang and Deschênes, 1997) (Fig.2-23). While the overall output of L6 CT during stimulus drive is sustained, the precise relay of stimulus information from L6 CT to L2/3 RS is altered, and there is a loss of stimulus information carried by the L6 CT population (Fig.3-7). There is therefore loss of information relayed to specific downstream L2/3 receiving from L6 CT, and they no longer express heterogeneous deviant (history) dependent representations.

The encoding of small stimulus changes in L2/3 RS that we observed, specifically their history dependence, is analogous to the emergence of complex tempo-spatial receptive fields in upper layers of visual cortex (Martin and Whitteridge, 1984; Gilbert, 1977). The diversity in L2/3 responses that we observed could reflect neuron types defined by biophysical characteristics (Jouhanneau et al., 2014) or projection targets, such as targeting to higher somatosensory or motor cortices (Sato and Svoboda, 2010; Chen et al., 2013), or emerge from afferent connectivity, or synaptic weights.

The sparse but overall faithful (in contrast to L2/3) stimulus encoding in L6 CT that we observed (Fig.2-23) could represent either an explicit deviant encoding, as in L4 (Fig.2-12), or a delayed stimulus or expectation encoding that, in mouse S1, emerges over timescales over 100 ms. The sparsity of L6 CT cell activity, and their targeting by long-range cortico-cortical afferents (Vélez-Fort et al., 2014) suggests that they might encode, or are significantly modulated by a top-down stimulus expectation, rather than being predominantly thalamically driven, but the stimulus design used in this study (with the exception of the gap-crossing experiments) does not allow discrimination between a delayed stimulus encod-

ing and an anticipatory/extrapolation encoding. The present study does therefore not allow us to directly test whether the L6 encoding is driven by top-down inputs, or represents a simpler, strictly local change encoding, but clearly establishes the role of stimulus encoding in L6, showing its potential role as a substrate of cortico-cortical comparisons of expectations and data.

We observed significantly higher latencies of vibrissa stimulus evoked firing in L6 than in other layers (using extracellular electrophysiology, Fig.2-15, which is at odds with the fast L6 activation by direct thalamic stimulation (Beierlein and Connors, 2002). This finding suggests that L6 driving in our experimental conditions is not predominantly thalamically driven, supporting the idea of cortico-cortical input as a main determinant of L6 firing, but a much more robust examination of L6 firing, with higher data quality than is possible with sparse tetrode recordings or slow calcium imaging, in naturalistic stimulus conditions is needed to answer this question.

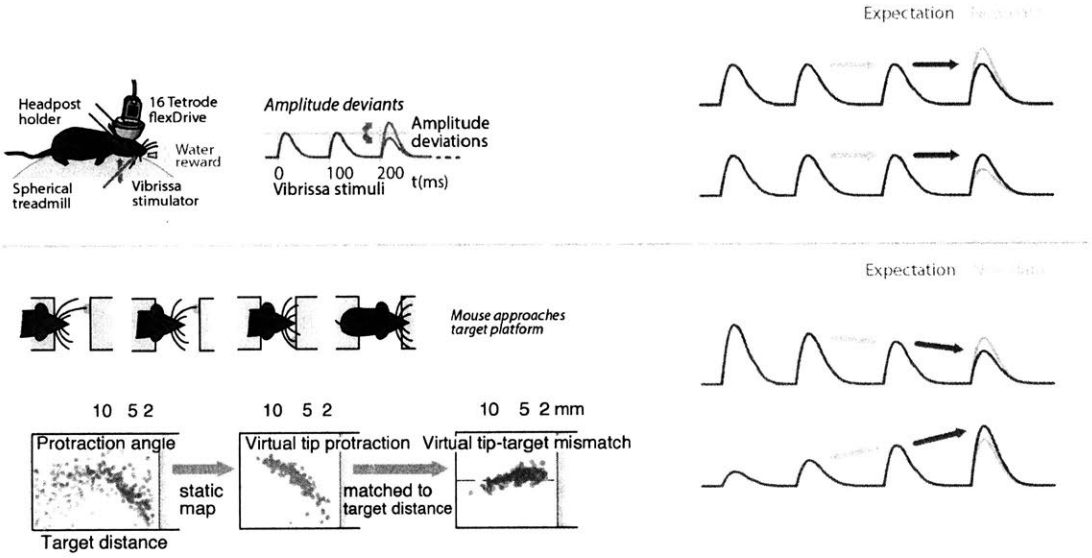

Figure 5-3: **The gap-crossing experiment provides some evidence that the observed change-specific effects of L6 disruption apply when epectations are not static. Top**, In the head-fixed experiments using electrophysiology and 2-photon imaging, stimulus deviants were applied after repetitions of the same deflection amplitude, deviant-detection could therefore rely on comparison between a static expectation and a deviating sensory input. **Bottom**, Figure adapted from (Voigts et al., 2015). In gap-crossing, sensory parameters as well as the motor pattern change continuously as mice approach the target. In this scenario, the expectation for sensory input in any whisking cycle differs form the sensory data received in the prior cycle.

Are the observed effects expected to replicate for changing stimuli, where a stimulus expectation relied on extrapolation, as in the framework of (top-down) predictive coding, or are they restricted to simple stimuli where expectations are set by mere repetition of a stimulus? The replication of the specific disruption of the perception of stimulus changes, without effects on gap-crossing performance on stationary platforms (Fig.4-8), where sen-

sory stimuli and motor patterns change significantly as the mouse approaches and palpates the target (Voigts et al., 2008, 2015) provides some evidence that the same mechanism is engaged when stimuli are non-static over the time scale of the decision making process, but instead are specific to the comparison between a (changing) sensory input and a (changing) expectation. It is however possible that the modulation of the whisking pattern (reduction of whisker protraction angles, asymmetric whisker protractions etc.) serve to stabilize specific aspects of the tactile sensory input, so that this representation can stay constant even as the mouse navigates its environment, and change only if the environment changes (Voigts et al., 2015; Ahissar and Assa, 2016; Mitchinson, 2016; Schroeder and Ritt, 2016).

The replication of the sparsity of sensory responses (Fig.3-3,2-23) and the overall gain modulation effects by moderate increases of L6 drive (Fig.3-2,4-10), suggests that the same overall circuitry that was observed in mouse V1 (Olsen et al., 2012; Bortone et al., 2014) exists in S1, and that the effects we observed here should apply similarly to change encoding in v1. This prediction is supported by L6 mediated modulation of visual receptive fields by stimulus context (Bolz and Gilbert, 1986; Grieve and Sillito, 1991) and by preferential involvement of deep cortical layers in top-down sensory processing (Kok et al., 2016),

A further important aspect of the stimulus coding by L6 CT cells is the nature of their output connectivity: In stark contrast to almost all other classes of cortical pyramidal cells whose synapses exhibit depression in repeated activation (Thomson et al., 1993; Thomson, 1997; Thomson and Bannister, 1999), CT neurons form facilitating synapses (Beierlein and Connors, 2002; West et al., 2006). This implies that the sparse and not well phasically time-locked encoding of stimuli that we observed in L6 CT cells (Fig.2-23), and L6 in general (Fig.3-3) are in line with the idea that the L6 output to its cortical column might not match the same timescale as the bottom-up thalamic input received by the circuit, as would be expected for predominantly top-down input.

The high number of L6 CT cells relative to pyramidal cells in more superficial layers (Narayanan et al., 2015) poses another question on what information is transmitted by L6 cells to their targets within the same column: the small number of L6 cells that we observed to be stimulus driven for any given experiment ($\sim$ around 10%), and their low firing rates, show that different ensembles of L6 CT cells are active in different contexts. If the input to L6 from other cortical areas is carrying a top-down expectation of the input to their local cortical column, and if the local columnar circuitry is performing a comparison between the top-down and bottom-up inputs, then one potential role of the population of L6 neurons could be to translate this (likely more abstract, sparse and invariant) representation to the representation that the expected stimulus would elicit in the local (lower) sensory area. This hypothesis makes some specific, but experimentally hard to test predictions. For instance, different top-down contexts, elicited by sensory input, that are expected to have the same computational effect in lower sensory areas, for example vestibular input suggesting a translation of the visual field in V1, or translation of the visual periphery suggesting the same translation on the local, recorded, column of V1, should result in activaiton of two distinct populations in L6 that have the same downstream effect on superficial cells in their column.

5.4 Rodent S1 specific computations

Parts of this section were previously published in Voigts J., Herman D.H., Celikel T. Tactile Object Localization by Anticipatory Whisker Motion. (2014) *Journal of neurophysiology* 22:jn.00241.2014. doi: 10.1152/jn.00241.2014.

Even though there is, as outlined above, evidence that suggests that the circuit mechanism described in this thesis should be applicable to other cortical areas, there are aspects of this study that could be specific to rodent barrel cortex, or at least deserve a dedicated discussion in the context of this model system.

The rodent vibrissa system is particularly interesting from a point of view of anticipatory coding because vibrissae in rodents are typically used in an 'active' manner - whiskers are active sensory organs that are swept through space in order to sense the environment (Vincent, 1912; Welker, 1964; Woolsey and Van der Loos, 1970; Hutson and Masterton, 1986; Carvell and Simons, 1990; Deschenes et al., 2003; Kleinfeld et al., 2006; Brecht, 2007; Mehta et al., 2007; Ahissar and Knutsen, 2008; Voigts et al., 2008; Jadhav and Feldman, 2010; O'Connor et al., 2013). This whisking pattern is not stereotyped, but depends on the sensory input and the animal's movement through its environment in multiple ways. Contacts with objects typically lead to an immediate reduction in the whisker protraction amplitude (Carvell and Simons, 1990; Mitchinson et al., 2007). This reduction can be as rapid as within the same protraction cycle, manifesting in fast touch induced retractions, so called 'pump' motions (Deutsch et al., 2012; Sherman et al., 2013). This reduction in whisking amplitude leads to an overall tendency of whiskers to only lightly touch the environment, minimizing the amplitude of whisker deflection, and with it the force that acts on whiskers during contacts as well as whisker vibrations, deflection angle etc.

In addition, rats quickly modulate whisking amplitude as well as the spread between their whiskers following contact with an unexpected object, in order to maximize the number of whiskers touching the object while maintaining only light contacts (Grant et al., 2009), suggesting that the whisking pattern is modulated with the aim of maximizing information content of whisker contacts, or to stabilize the order of contacts across whiskers (Desîlets-Roy et al., 2002). Protractions are also modulated asymmetrically to compensate for lateral object contacts, so that whisker deflection strength is stabilized across both sides (Sachdev et al., 2003; Towal and Hartmann, 2008). This lateral adaptation of the whisking pattern to the environment anticipates exploratory head motion (Towal and Hartmann, 2006), indicating that it is actively driven by the exploratory behaviour rather than a reaction to sensory inputs.

In a mobile tactile organ like this, whose position is highly variable, the position of the sensory organ has to be integrated with the sensory input (time and force etc. of contacts with the environment) in order to decode information about the environment (Kleinfeld et al., 2006; Knutsen and Ahissar, 2009; Saraf-Sinik et al., 2015). In rodent S1, this integration is fairly well delineated from a point of view of neural circuits because it involves touch events that are, in the case of distance encoding, mainly determined by their timing but can be somewhat stereotyped in their other properties (O'Connor et al., 2013), with motor information that can be measured readily using videography (Knutsen et al., 2005; Voigts et al., 2008) and manipulated (Schroeder et al., 2013; Schroeder and Ritt, 2013).

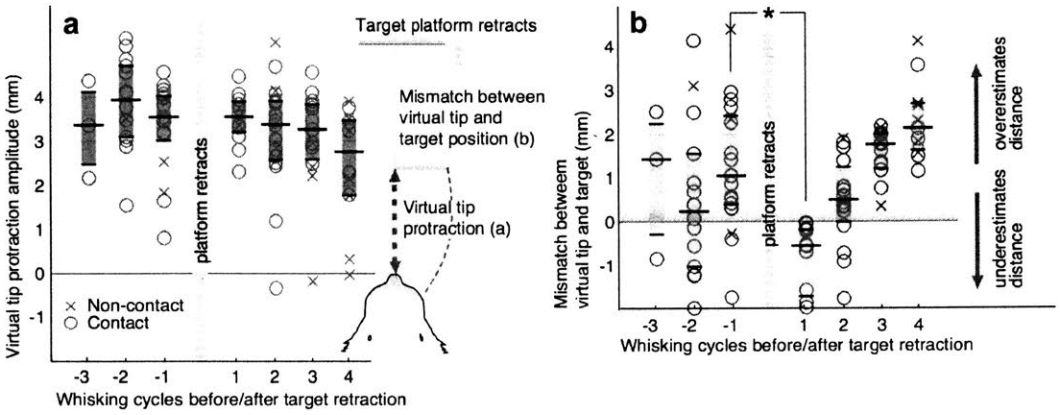

Figure 5-4: **Changed sensory input does not immediately alter whisking pattern.** Figure adapted from (Voigts et al., 2015). Data is organized into protractions leading up to and following a sudden retraction of the target platform by 4.88 ± 0.41mm. Box plots indicate median, 50% and 75% quantiles. Only whisker protractions leading to or following contacts by < 100 ms were included in the analysis. Data during platform retraction were excluded. Circles indicate protractions that led to whisker contact, crosses indicate misses. **a**, Maximum virtual tip protraction amplitude per cycle (derived from whisker base angle, see (Voigts et al., 2015)). **b**, Mismatch between virtual whisker tip protraction and target position (same as the blue arrow in inset). Yellow line: approximate mismatch across all datasets (~1mm). The mouse continues to approach the target platform between the two measurements, this results in an increase of the prediction error of only ~2mm even though the platform is retracted by ~5mm. Further approach motion by the mouse then further rises the mismatch values without significant change in whisker protraction angles.

This makes the rodent, and specifically mouse vibrissa system a good model system for studying non-linear integration of different information streams.

In my own undergrad work (Voigts et al., 2015), I found that in the context of gap-crossing, where mice have to estimate the distance to a platform in order to step onto it (Hutson and Masterton, 1986), this modulation of the whisking pattern is not a direct reaction to the sensory input (even though this type of fast feedback control is clearly involved for unexpected, or faster contacts (Deutsch et al., 2012; Grant et al., 2009; Sherman et al., 2013)). Instead, whisker protractions seem to be matched to the distance at which mice expect the target, based on previous whisking cycles (~60-120ms prior to the current contact event). Using the same general approach of retracting a target platform mid-exploration as in this thesis (Fig.4-5), but with a larger change in platform position (5mm vs. 2mm), we found that this sudden increase in distance to the target did not immediately result in an increase in whisker protraction amplitude (Fig.5-4). The same mechanism of an anticipatory whisking pattern extends to lateralized object localization during goal-oriented localization behaviour (Schroeder and Ritt, 2016).

This motor strategy has implications for the decoding of sensory information: If whiskers are protracted to expected object positions, then the timing (and force etc.) of contacts

with the actual object doesnt simply encode the distance to that object, but instead encodes a prediction error. If mouse S1 expects to see such a physically pre-computed error signal, this likely has implications to how we need to look at all cortical computation in this system.

In the context of this thesis, this view implies that the encoding in L6 should not only encode a stimulus expectation or history, as observed here in the case of stimulus trains delivered to awake but non-whisking mice, but instead likely encodes a correlate of the animal's current hypothesis about its tactile environment (Voigts et al., 2015). This implies that the stimulus encoding in L6 might be directly modulated by inputs from vM1 (Kleinfeld and Deschenes, 2011; Friedman et al., 2012; Hill et al., 2011), or that L6 could mediate a context dependent gating of whisking motor signals through thalamus (Lee et al., 2008). This exact kind of sensorimotor coincidence detection was recently observed (Xu et al., 2012) and shown to be required for active tactile stimulus processing (Nattar Ranganatha et al., 2014) for L5 pyramidal neurons in S1 of whisking mice.

The obvious caveat here is that in this thesis, all neural recordings were performed in stationary awake animals that, due to the need for whisker attached stimulators, did not whisk. Examining L6 encoding in a gap-crossing paradigm could resolve this question, though the sparsity of L6 responses coupled with the effort required to obtain high numbers of trials in the gap-crossing task would make this a challenging experiment.

5.5 Conclusions and future directions

In sum, we found that specific encoding of stimulus features by L6 CT cells is required for the encoding of changes along these feature dimensions in L2/3 and for change detection behavior, and may be fundamental to general encoding of higher order stimulus features, stimulus context, or expectations reliant on top-down signaling, in agreement with L6 CT targeting by long range cortico-cortical inputs (Vélez-Fort et al., 2014; Zhang et al., 2014).

There are a range of open questions that are raised by the work presented in this thesis: what information is actually encoded by the L6 population? What are the cellular and circuit mechanisms that implement the observed change encoding in superficial layers, and what are the higher level behavioral and computational properties of local cortical computations?

The present findings differentiate the effect of the weak L6 drive on stimulus changes versus a lack of effect on non-changing stimuli in a few relatively simple cases where stimulus expectations are formed by simple repetition of the same stimulus. One notable exception is the gap-crossing tasks, where even though the target platform remains stable, the sensory input during both non-changing and changing trials is highly variable between whisk cycles (Voigts et al., 2008, 2015). It remains to be seen if the same L6 manipulation has the same specific effect in cases where the stimulus expectation is driven by either a static model that performs some non-trivial extrapolation of sensory data, or pattern learning.

Simple extrapolation and anticipatory coding effects in visual cortex, such as the flash-lag effect (Nijhawan, 2002) or extra-classical RF properties such as end-stopping (Bolz and

Gilbert, 1986; Rao and Ballard, 1999; Grieve and Sillito, 1991) could be exploited for this question. Such a study would be able to differentiate between a role of L6 in comparing stimulus-history to current stimuli, and a role in true predictive coding, though there are multiple lines of evidence in animal (Bolz and Gilbert, 1986) and human studies (Kok et al., 2016) suggesting the latter.

Another related fundamental question is if the same effect would be observed not just for expectations formed by extrapolation of sensory input, but by expectations relayed from other brain areas. The connectivity of L6 CT cells suggests that they receive far reaching cortico-cortical input (Vélez-Fort et al., 2014), suggesting that expectations arising from higher order representations should be associated with sensory input through L6. There are some tractable approaches to testing this hypothesis about the role of top-down input through L6 that rely on the ability to manipulate this input independently from the bottom-up sensory input.

One of the key challenges that needs to be confronted by studies of cortical computation is that the computational input-output relationship of the circuit under study is typically not known. In this thesis, I was able to use the stimulus change encoding in L2/3 as a partial read-out of whether changes were explicitly encoded by the cortical circuit. Further, the behavioural findings allowed me to compare the effect of the L6 manipulation on change detection versus the detection and processing of non-changing stimuli. However, in neither case was I able to control the information content of the top-down signal, and make inferences about its expected relationship to the stimulus encoding.

There are possible follow-up experiments that could exploit computational relationships between sensory inputs and their interpretations that are known a-priori to overcome this limitation. If a relationship between multiple accessible inputs to a cortical region exists outside of the experimental setup, and is known, then it can be reasonably expected that the cortical area combines the inputs, and can be used to study the implementation of the computation. For example, rotation of the head, transduced by the vestibular system, typically results in a predictable visual flow that should be encoded in V1 (DeAngelis and Angelaki, 2012; Rancz et al., 2015). Similarly, motor input into S1, signaling the position of a whisker, should affect the encoding of whisker deflections (Wallach et al., 2016; Curtis and Kleinfeld, 2009). Crucially from a practical point of view, such relationships do not need to be specifically trained, and can be verified with relative ease in naive animals. This approach would allow direct manipulation of multiple inputs into the cortical circuit, and allow a clearer study of the relative encoding of expectation versus sensory input across different neural populations.

Bibliography

Ahissar, E. and Assa, E. (2016). Perception as a closed-loop convergence process. *eLife*, 5:e12830.

Ahissar, E. and Knutsen, P. M. (2008). Object localization with whiskers. *Biological Cybernetics*, 98(6):449–458. WOS:000256079900002.

Andermann, M. L. and Moore, C. I. (2006). A somatotopic map of vibrissa motion direction within a barrel column. *Nature Neuroscience*, 9(4):543–551.

Beierlein, M. and Connors, B. W. (2002). Short-term dynamics of thalamocortical and intracortical synapses onto layer 6 neurons in neocortex. *Journal of Neurophysiology*, 88(4):1924–1932.

Bolz, J. and Gilbert, C. D. (1986). Generation of end-inhibition in the visual cortex via interlaminar connections. *Nature*, 320(6060):362–365.

Bortone, D. S., Olsen, S. R., and Scanziani, M. (2014). Translaminar Inhibitory Cells Recruited by Layer 6 Corticothalamic Neurons Suppress Visual Cortex. *Neuron*, 82(2):474–485.

Brecht, M. (2007). Barrel cortex and whisker-mediated behaviors. *Current Opinion in Neurobiology*, 17(4):408–416. WOS:000250666200004.

Callaway, E. M. (1998). Local Circuits in Primary Visual Cortex of the Macaque Monkey. *Annual Review of Neuroscience*, 21(1):47–74.

Carvell, G. and Simons, D. (1990). Biometric Analyses of Vibrissal Tactile Discrimination in the Rat. *Journal of Neuroscience*, 10(8):2638–2648. WOS:A1990DW22100012.

Celikel, T. and Sakmann, B. (2007). Sensory integration across space and in time for decision making in the somatosensory system of rodents. *Proceedings of the National Academy of Sciences*, 104(4):1395–1400.

Chen, T.-W., Wardill, T. J., Sun, Y., Pulver, S. R., Renninger, S. L., Baohan, A., Schreiter, E. R., Kerr, R. A., Orger, M. B., Jayaraman, V., Looger, L. L., Svoboda, K., and Kim, D. S. (2013). Ultrasensitive fluorescent proteins for imaging neuronal activity. *Nature*, 499(7458):295–300.

Clancy, K. B., Schnepel, P., Rao, A. T., and Feldman, D. E. (2015). Structure of a Single Whisker Representation in Layer 2 of Mouse Somatosensory Cortex. *The Journal of Neuroscience*, 35(9):3946–3958.

Crochet, S., Poulet, J. F. A., Kremer, Y., and Petersen, C. C. H. (2011). Synaptic mechanisms underlying sparse coding of active touch. *Neuron*, 69(6):1160–1175.

Curtis, J. C. and Kleinfeld, D. (2009). Phase-to-rate transformations encode touch in cortical neurons of a scanning sensorimotor system. *Nature Neuroscience*, 12(4):492–501. WOS:000264563100024.

DeAngelis, G. C. and Angelaki, D. E. (2012). Visual–Vestibular Integration for Self-Motion Perception. In Murray, M. M. and Wallace, M. T., editors, *The Neural Bases of Multisensory Processes*, Frontiers in Neuroscience. CRC Press/Taylor & Francis, Boca Raton (FL).

Deschenes, M., Timofeeva, E., and Lavallee, P. (2003). The relay of high-frequency sensory signals in the whisker-to-barreloid pathway. *Journal of Neuroscience*, 23(17):6778–6787. WOS:000184469200013.

Desîlets-Roy, B., Varga, C., Lavallée, P., and Deschênes, M. (2002). Substrate for Cross-Talk Inhibition between Thalamic Barreloids. *The Journal of Neuroscience*, 22(9):RC218–RC218.

Deutsch, D., Pietr, M., Knutsen, P. M., Ahissar, E., and Schneidman, E. (2012). Fast Feedback in Active Sensing: Touch-Induced Changes to Whisker-Object Interaction. *PLOS ONE*, 7(9):e44272.

Friedman, W. A., Zeigler, H. P., and Keller, A. (2012). Vibrissae motor cortex unit activity during whisking. *Journal of Neurophysiology*, 107(2):551–563.

Gilbert, C. D. (1977). Laminar differences in receptive field properties of cells in cat primary visual cortex. *The Journal of Physiology*, 268(2):391–421.

Gong, S., Doughty, M., Harbaugh, C. R., Cummins, A., Hatten, M. E., Heintz, N., and Gerfen, C. R. (2007). Targeting Cre Recombinase to Specific Neuron Populations with Bacterial Artificial Chromosome Constructs. *The Journal of Neuroscience*, 27(37):9817–9823.

Grant, R. A., Mitchinson, B., Fox, C. W., and Prescott, T. J. (2009). Active Touch Sensing in the Rat: Anticipatory and Regulatory Control of Whisker Movements During Surface Exploration. *Journal of Neurophysiology*, 101(2):862–874. WOS:000263120300033.

Grieve, K. L. and Sillito, A. M. (1991). A re-appraisal of the role of layer VI of the visual cortex in the generation of cortical end inhibition. *Experimental Brain Research*, 87(3):521–529.

Harnett, M. T., Xu, N.-L., Magee, J. C., and Williams, S. R. (2013). Potassium Channels Control the Interaction between Active Dendritic Integration Compartments in Layer 5 Cortical Pyramidal Neurons. *Neuron*, 79(3):516–529.

Hill, D. N., Curtis, J. C., Moore, J. D., and Kleinfeld, D. (2011). Primary motor cortex reports efferent control of vibrissa motion on multiple timescales. *Neuron*, 72(2):344–356.

Houweling, A. R. and Brecht, M. (2008). Behavioural report of single neuron stimulation in somatosensory cortex. *Nature*, 451(7174):65–68.

Hutson, K. A. and Masterton, R. B. (1986). The sensory contribution of a single vibrissa's cortical barrel. *Journal of Neurophysiology*, 56(4):1196–1223.

Jadhav, S. P. and Feldman, D. E. (2010). Texture coding in the whisker system. *Current Opinion in Neurobiology*, 20(3):313–318. WOS:000279364800007.

Jouhanneau, J.-S., Ferrarese, L., Estebanez, L., Audette, N. J., Brecht, M., Barth, A. L., and Poulet, J. F. A. (2014). Cortical fosGFP Expression Reveals Broad Receptive Field Excitatory Neurons Targeted by POm. *Neuron*, 84(5):1065–1078.

Khatri, V. and Simons, D. J. (2007). Angularly nonspecific response suppression in rat barrel cortex. *Cerebral Cortex (New York, N.Y.: 1991)*, 17(3):599–609.

Kleinfeld, D., Ahissar, E., and Diamond, M. E. (2006). Active sensation: Insights from the rodent vibrissa sensorimotor system. *Current Opinion in Neurobiology*, 16(4):435–444. WOS:000240277900012.

Kleinfeld, D. and Deschenes, M. (2011). Neuronal Basis for Object Location in the Vibrissa Scanning Sensorimotor System. *Neuron*, 72(3):455–468. WOS:000296826000004.

Knutsen, P. M. and Ahissar, E. (2009). Orthogonal coding of object location. *Trends in Neurosciences*, 32(2):101–109.

Knutsen, P. M., Derdikman, D., and Ahissar, E. (2005). Tracking whisker and head movements in unrestrained behaving rodents. *Journal of Neurophysiology*, 93(4):2294–2301.

Kok, P., Bains, L. J., van Mourik, T., Norris, D. G., and de Lange, F. P. (2016). Selective Activation of the Deep Layers of the Human Primary Visual Cortex by Top-Down Feedback. *Current Biology*, 26(3):371–376.

Larkum, M. E., Zhu, J. J., and Sakmann, B. (1999). A new cellular mechanism for coupling inputs arriving at different cortical layers. *Nature*, 398(6725):338–341.

Lee, S., Carvell, G. E., and Simons, D. J. (2008). Motor modulation of afferent somatosensory circuits. *Nature Neuroscience*, 11(12):1430–1438.

Lee, S.-H., Kwan, A. C., Zhang, S., Phoumthipphavong, V., Flannery, J. G., Masmanidis, S. C., Taniguchi, H., Huang, Z. J., Zhang, F., Boyden, E. S., Deisseroth, K., and Dan, Y. (2012). Activation of specific interneurons improves V1 feature selectivity and visual perception. *Nature*, 488(7411):379–383.

Lefort, S., Tomm, C., Floyd Sarria, J.-C., and Petersen, C. C. H. (2009). The excitatory neuronal network of the C2 barrel column in mouse primary somatosensory cortex. *Neuron*, 61(2):301–316.

Martin, K. A. and Whitteridge, D. (1984). Form, function and intracortical projections of spiny neurones in the striate visual cortex of the cat. *The Journal of Physiology*, 353:463–504.

Marx, M. and Feldmeyer, D. (2013). Morphology and physiology of excitatory neurons in layer 6b of the somatosensory rat barrel cortex. *Cerebral Cortex (New York, N.Y.: 1991)*, 23(12):2803–2817.

Mehta, S. B., Whitmer, D., Figueroa, R., Williams, B. A., and Kleinfeld, D. (2007). Active Spatial Perception in the Vibrissa Scanning Sensorimotor System. *PLOS Biol*, 5(2):e15.

Mercer, A., West, D. C., Morris, O. T., Kirchhecker, S., Kerkhoff, J. E., and Thomson, A. M. (2005). Excitatory connections made by presynaptic cortico-cortical pyramidal cells in layer 6 of the neocortex. *Cerebral Cortex (New York, N.Y.: 1991)*, 15(10):1485–1496.

Mitchinson, B. (2016). Tactile Attention in the Vibrissal System. In Prescott, T., Ahissar, E., and Izhikevich, E., editors, *Scholarpedia of Touch*, Scholarpedia, pages 771–779. Atlantis Press.

Mitchinson, B., Martin, C. J., Grant, R. A., and Prescott, T. J. (2007). Feedback control in active sensing: Rat exploratory whisking is modulated by environmental contact. *Proceedings. Biological Sciences / The Royal Society*, 274(1613):1035–1041.

Movshon, J. A. and Lennie, P. (1979). Pattern-selective adaptation in visual cortical neurones. *Nature*, 278(5707):850–852.

Narayanan, R. T., Egger, R., Johnson, A. S., Mansvelder, H. D., Sakmann, B., de Kock, C. P. J., and Oberlaender, M. (2015). Beyond Columnar Organization: Cell Type- and Target Layer-Specific Principles of Horizontal Axon Projection Patterns in Rat Vibrissal Cortex. *Cerebral Cortex*, 25(11):4450–4468.

Nattar Ranganatha, G., Xu, N.-L., and Magee, J. C. (2014). Active dendritic integration in L5 pyramidal neurons contributes to sensorimotor learning. *Society for Neuroscience Meeting 2014 DC*.

Niell, C. M. and Stryker, M. P. (2008). Highly Selective Receptive Fields in Mouse Visual Cortex. *The Journal of neuroscience : the official journal of the Society for Neuroscience*, 28(30):7520–7536.

Nijhawan, R. (2002). Neural delays, visual motion and the flash-lag effect. *Trends in Cognitive Sciences*, 6(9):387–393.

O'Connor, D. H., Hires, S. A., Guo, Z. V., Li, N., Yu, J., Sun, Q.-Q., Huber, D., and Svoboda, K. (2013). Neural coding during active somatosensation revealed using illusory touch. *Nature Neuroscience*, 16(7):958–965.

Olsen, S. R., Bortone, D. S., Adesnik, H., and Scanziani, M. (2012). Gain control by layer six in cortical circuits of vision. *Nature*, 483(7387):47–52.

Peron, S. P., Freeman, J., Iyer, V., Guo, C., and Svoboda, K. (2015). A Cellular Resolution Map of Barrel Cortex Activity during Tactile Behavior. *Neuron*, 86(3):783–799.

Rancz, E. A., Moya, J., Drawitsch, F., Brichta, A. M., Canals, S., and Margrie, T. W. (2015). Widespread Vestibular Activation of the Rodent Cortex. *The Journal of Neuroscience*, 35(15):5926–5934.

Rao, R. P. N. and Ballard, D. H. (1999). Predictive coding in the visual cortex: A functional interpretation of some extra-classical receptive-field effects. *Nature Neuroscience*, 2(1):79–87.

Ritt, J. T., Andermann, M. L., and Moore, C. I. (2008). Embodied information processing: Vibrissa mechanics and texture features shape micromotions in actively sensing rats. *Neuron*, 57(4):599–613.

Sachdev, R. N. S., Berg, R. W., Champney, G., Kleinfeld, D., and Ebner, F. F. (2003). Unilateral vibrissa contact: Changes in amplitude but not timing of rhythmic whisking. *Somatosensory & Motor Research*, 20(2):163–169.

Sachidhanandam, S., Sermet, B. S., and Petersen, C. C. H. (2016). Parvalbumin-Expressing GABAergic Neurons in Mouse Barrel Cortex Contribute to Gating a Goal-Directed Sensorimotor Transformation. *Cell Reports*.

Sachidhanandam, S., Sreenivasan, V., Kyriakatos, A., Kremer, Y., and Petersen, C. C. H. (2013). Membrane potential correlates of sensory perception in mouse barrel cortex. *Nature Neuroscience*, 16(11):1671–1677.

Saraf-Sinik, I., Assa, E., and Ahissar, E. (2015). Motion Makes Sense: An Adaptive Motor-Sensory Strategy Underlies the Perception of Object Location in Rats. *The Journal of Neuroscience*, 35(23):8777–8789.

Sato, T. R. and Svoboda, K. (2010). The Functional Properties of Barrel Cortex Neurons Projecting to the Primary Motor Cortex. *The Journal of Neuroscience*, 30(12):4256–4260.

Schroeder, J. B., Mariano, V. J., Telian, G. I., and Ritt, J. T. (2013). Stimulation of somatosensory cortex locked to whisker motions in a mouse model of active sensing. In *2013 6th International IEEE/EMBS Conference on Neural Engineering (NER)*, pages 637–640.

Schroeder, J. B. and Ritt, J. T. (2013). Extraction of intended palpation times from facial EMGs in a mouse model of active sensing. In *2013 35th Annual International Conference of the IEEE Engineering in Medicine and Biology Society (EMBC)*, pages 2016–2019.

Schroeder, J. B. and Ritt, J. T. (2016). Selection of head and whisker coordination strategies during goal-oriented active touch. *Journal of Neurophysiology*, 115(4):1797–1809.

Sherman, D., Oram, T., Deutsch, D., Gordon, G., Ahissar, E., and Harel, D. (2013). Tactile Modulation of Whisking via the Brainstem Loop: Statechart Modeling and Experimental Validation. *PLOS ONE*, 8(11):e79831.

Siegle, J. H., Pritchett, D. L., and Moore, C. I. (2014). Gamma-range synchronization of fast-spiking interneurons can enhance detection of tactile stimuli. *Nature Neuroscience*, 17(10):1371–1379.

Thomson, A. M. (1997). Activity-dependent properties of synaptic transmission at two classes of connections made by rat neocortical pyramidal axons in vitro. *The Journal of Physiology*, 502 (Pt 1):131–147.

Thomson, A. M. (2010). Neocortical Layer 6, A Review. *Frontiers in Neuroanatomy*, 4.

Thomson, A. M. and Bannister, A. P. (1999). Release-independent depression at pyramidal inputs onto specific cell targets: Dual recordings in slices of rat cortex. *The Journal of Physiology*, 519 Pt 1:57–70.

Thomson, A. M., Deuchars, J., and West, D. C. (1993). Large, deep layer pyramid-pyramid single axon EPSPs in slices of rat motor cortex display paired pulse and frequency-dependent depression, mediated presynaptically and self-facilitation, mediated postsynaptically. *Journal of Neurophysiology*, 70(6):2354–2369.

Towal, R. B. and Hartmann, M. J. (2006). Right-left asymmetries in the whisking behavior of rats anticipate head movements. *Journal of Neuroscience*, 26(34):8838–8846. WOS:000240006200022.

Towal, R. B. and Hartmann, M. J. Z. (2008). Variability in velocity profiles during free-air whisking behavior of unrestrained rats. *Journal of Neurophysiology*, 100(2):740–752. WOS:000258394500021.

Vélez-Fort, M., Rousseau, C. V., Niedworok, C. J., Wickersham, I. R., Rancz, E. A., Brown, A. P. Y., Strom, M., and Margrie, T. W. (2014). The Stimulus Selectivity and Connectivity of Layer Six Principal Cells Reveals Cortical Microcircuits Underlying Visual Processing. *Neuron*, 83(6):1431–1443.

Vincent, S. B. (1912). *The Functions of the Vibrissae in the Behavior of the White Rat ...* University of Chicago.

Voigts, J., Herman, D. H., and Celikel, T. (2015). Tactile object localization by anticipatory whisker motion. *Journal of neurophysiology*, 113(2):620–632.

Voigts, J., Sakmann, B., and Celikel, T. (2008). Unsupervised whisker tracking in unrestrained behaving animals. *Journal of neurophysiology*, 100(1):504–515.

Wallach, A., Bagdasarian, K., and Ahissar, E. (2016). On-going computation of whisking phase by mechanoreceptors. *Nature Neuroscience*, 19(3):487–493.

Welker, W. I. (1964). Analysis of Sniffing of the Albino Rat. *Behaviour*, 22(3/4):223–244.

West, D. C., Mercer, A., Kirchhecker, S., Morris, O. T., and Thomson, A. M. (2006). Layer 6 cortico-thalamic pyramidal cells preferentially innervate interneurons and generate facilitating EPSPs. *Cerebral Cortex (New York, N.Y.: 1991)*, 16(2):200–211.

Wiser, A. K. and Callaway, E. M. (1996). Contributions of individual layer 6 pyramidal neurons to local circuitry in macaque primary visual cortex. *The Journal of Neuroscience: The Official Journal of the Society for Neuroscience*, 16(8):2724–2739.

Wiser, A. K. and Callaway, E. M. (1997). Ocular dominance columns and local projections of layer 6 pyramidal neurons in macaque primary visual cortex. *Visual Neuroscience*, 14(2):241–251.

Woolsey, T. A. and Van der Loos, H. (1970). The structural organization of layer IV in the somatosensory region (SI) of mouse cerebral cortex. The description of a cortical field composed of discrete cytoarchitectonic units. *Brain Research*, 17(2):205–242.

Xu, N.-l., Harnett, M. T., Williams, S. R., Huber, D., O'Connor, D. H., Svoboda, K., and Magee, J. C. (2012). Nonlinear dendritic integration of sensory and motor input during an active sensing task. *Nature*, 492(7428):247–251.

Zhang, S., Xu, M., Kamigaki, T., Do, J. P. H., Chang, W.-C., Jenvay, S., Miyamichi, K., Luo, L., and Dan, Y. (2014). Long-range and local circuits for top-down modulation of visual cortex processing. *Science*, 345(6197):660–665.

Zhang, Z.-w. and Deschênes, M. (1997). Intracortical axonal projections of lamina VI cells of the primary somatosensory cortex in the rat: A single-cell labeling study. *J Neurosci*, pages 6365–6379.

Appendices

Appendix A

Open source tools for neuroscience

Parts of this chapter were previously published in Siegle, J. H., Hale, G. J., Newman, J. P., and Voigts, J. (2015). Neural ensemble communities: open-source approaches to hardware for large-scale electrophysiology. Current *Opinion in Neurobiology*, 32:5359.

Experiments in systems neuroscience, almost always require non-trivial amounts of engineering and tool development. This is in part due to advances in technology that require integration of new methods into experimental preparations, as is the case in this thesis for electrode technology (Voigts et al., 2013), behavioural testing in behaving (Voigts et al., 2008, 2015) and head-fixed (Dombeck et al., 2007) mice, and 2-photon imaging (Denk et al., 1990). However, a large part of the development effort for individual experiments is often due to the requirements of integrating different methods into a single experimental setup, and most importantly, in the effort it takes to implement an method in a new setting. Even for relatively simple and mainstream methods like tetrode recordings, the gap between knowledge of the protocols in the existing literature and the ability to perform the experiments is quite large.

In around 2010, Josh Siegle, who was working in Chris Moore's and Matt Wilson's labs at the time, and myself started working on what would eventually become *open ephys*, a non-profit organization that facilitates the development and distribution of open-source hardware and software, with the ultimate goal of increasing scientific productivity.

When we started working on an open-source alternative to existing commercial amplifier systems for tetrode recordings in 2010, we decided to base the system on a chip developed by Reid Harrison at intan technology (`intantech.com`) that provided 32 analog amplifiers equivalent to existing electrophysiology systems on a single low cost chip (Harrison, 2007). Even though there already were well designed open-source multichannel data acquisition systems in use at the time (Wagenaar et al., 2005), we decided to build a system around these, then relatively new, integrated circuits because they promised to make the system simpler and more scalable than previous technology. We initially aimed for the simplest possible system with reasonably high channel counts (> 64) at low implant weights (< 2g) and relatively low closed-loop latency ($\sim$10ms). We chose to build a simple interface between this chip and a data acquisition PC based on existing, relatively easy to use FPGA modules `opalkelly.com` that spared us the task of developing a USB interface from scratch, and based the software on an industry-standard architecture for audio recording software

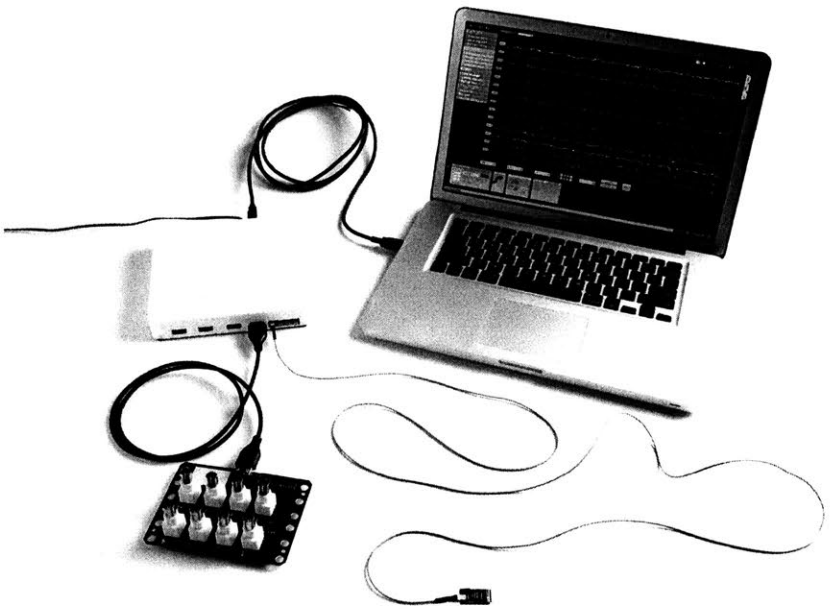

Figure A-1: **The Open Ephys data acquisition hardware.** Open Ephys is a complete open-source toolkit for high-channel-count electrophysiology, which includes headstages for digitizing neural signals, an acquisition board for interfacing with a computer, an I/O board for synchronizing with auxiliary devices, and a graphical user interface (GUI) for visualizing, analyzing, and recording data.

(`www.juce.com`) that took care of handling buffers of sampled data. Through the support of our advisors Chris Moore and Matt Wilson, and with generous backing from D. Meletis, M.Carlen, J. Goldberg, M. Jazayeri, O. Yizhar, D. Huber, D. Moorman, and especially with invaluable advice and support from Reid Harrison, we managed to fund and distribute the resulting hardware and software to an intial round of beta-tester labs, and successfully encouraged many labs to contribute their development efforts to open ephys. Since then, open ephys has grown with the support of many other students, post docs and PIs and as of spring 2016 provides labs in over 22 countries with hardware and software tools.

In addition to developing data acquisition systems and software, open ephys also showcases and facilitates distribution of other neuroscience-associated tools. In contrast to as little as 10 years ago, the increasing standardization of file formats and proliferation of collaborative platforms for version control has made it significantly easier to outsource the manufacturing of electronic devices. Companies like CircuitHub (`circuithub.com`, San Jose) or Seeedstudio (`seeedstudio.com`, Shenzhen) can now take standardized design documents for printed circuit boards and cases and produce anything from 10 to many hundreds or more devices easily and without excessive up-front charges or manufacturing delays. This means that given sufficient documentation and community driven quality-control and sup-

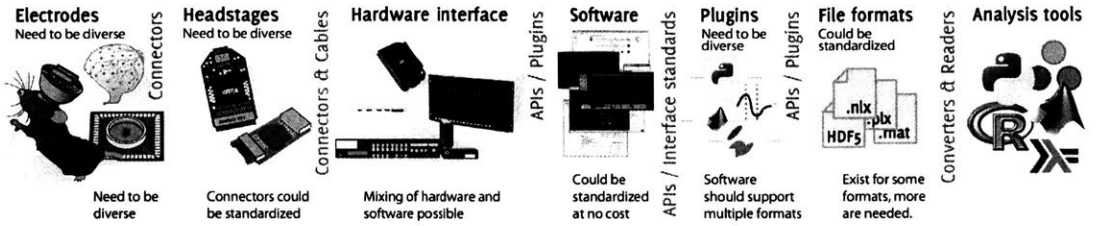

Figure A-2: **Key interfaces within multichannel electrophysiology platforms.** Adapted from Siegle et al. (2015). Overview of the main components and interfaces in multichannel electrophysiology systems. Some components and interfaces need to be incompatible in order to comply with different requirements, such as electrodes and their connectors. Others, such as interfaces for software plug-ins or the interfaces between recording hardware and software, could be standardized with little additional development cost. The vertical text describes the interfaces that we recommend standardizing to improve the overall efficiency of our field.

port, many of the manufacturing roles that are classically fulfiled by separate companies could now be decentralized and handled more directly by the researchers that design the tools in the first place.

A great example of this is the cyclops LED driver designed by Jon Newman (`www.open-ephys.org/cyclops`) for his work on closed-loop optogenetic control of firing rates (Newman et al., 2013) (the high speed and precision of this LED driver made the experiments outlined in Fig.3-4a possible). By providing initial funding for production and distribution, open ephys made it easier to get cyclops drivers into the hands of more labs quicker, and integrating the driver with our software will make it easier for researchers to integrate optogenetic stimulation into existing or new closed-loop experiments.

The increasing use of online forums, version control, and bug-tracking by neurosientists is another reason that open source tools have become more productive than their commercial counterparts. Classically, problem solving and technical support has been the role of companies that made individual pieces of equipment, but increasingly online communities of researchers are able to provide better advice and solve problems more quickly, simply by sharing existing expertise and existing solutions that they generated in their own work. Crucially, this makes it possible for the ongoing problem solving to keep pace with the simultaneous development of new methods. Often, only researchers that have already tried using a method in a new context, for instance by integrating methods in a novel way or performing new kinds of experiments, can and will solve problems that arise form this new use of existing tools. By using online version control systems, and open standards, these solutions are immediately applicable to other researchers.

Besides the lower price, the main feature that made open ephys attractive to new users are the open source nature of the system, and the accompanying adherence to open standards. Even though the widespread use of matlab (and increasinglt python (`python.org`) and julia (`julialang.org`) in the realm of off-line data analysis made it possible to share analysis methods, with nSTAT (Cajigas et al., 2012) being a good example of a large,

well maintained package for spike train analysis, similar standards do not exist for on-line analysis and integration of analysis code into experiments. Our aim with open ephys is to promote open standards for such interfaces that will make it easier to deveop share-able software modules, 'plugins' for neuroscience experiments.

The open-source software ImageJ (Abramoff et al., 2004) is a ubiquitous tool for scientific image processing, and is a prime example of how successful this approach can be: The core ImageJ software provides standards for plugin interfaces, which allows developers to quickly build and distribute their tools without having to worry about the infrastructure of any other parts of the program. Users of ImageJ can, for instance, use any file format, and combine any community developed algorithms seamlessly without having to worry about compatibility between them. This also means that the results of the processing are more easily replicable, because the same plugins can be used across labs without any hand-built glue logic or format conversions.

Similar standards are still lacking for data acquisition software in neuroscience, and providing a solution to this need is one of the core aims of open ephys. By adopting a modular plugin based structure for our software, we already made it fairly easy for other developers to write plugins for our software. For example, a developer writing a method for detecting specific neural events such as spindles (Warby et al., 2014) doesn't need to know anything about file formats, data handling, or visualization to be able to write a plugin that detects spindles in real-time, and the resulting software will be able to run in other labs seamlessly.

Examples of this plugin development are spike-sorting plugins developed by Shay Ohayon at Caltech that allowed him to characterize the response properties of individual neurons in real time, common average reference plugins, interface for closed-loop control via python, julia, or matlab code, or a system for evaluating novel types of intracortical electrodes that is currently being developed by a team around by Prof. Jon Viventi at NYU. Developers have also contributed plugins that allow Open Ephys to write data in different file formats, integrate video tracking, or use it as an EEG system.

Although it is becoming increasingly common for scientists to share their analysis code, the code itself is not usually required in order to make sense of the data generated in a study, as long as the statistical methods are well documented. For closed-loop experiments where the manipulation of the neural system depends on an ongoing analysis of the acquired data, this is no longer true. Depending on the experiment, statistical analysis of data coming out of closed-loop experiments will for instance require constructing null-hypothese by running the same algorithm on synthetic or modified data in order to understand how an observation depends on the neural system rather than on the manipulation. Therefore, the result of entire experiments might be uninterpretable without knowledge of the exact same algorithm that was used to generate them (Fig.A-3). Many current approaches to closed-loop experiments that rely on specialized hardware and custom-tailored algorithms that interact with commercial hardware and software make this impossible.

The ability to easily develop and share plugins that interact with neural data through common open interfaces is therefore important not just for scientific productivity, but for its reproducibility. This presents a technical challenge because algorithms for closed-loop experiments need to interact intimately with many other parts of the data acquisition sys-

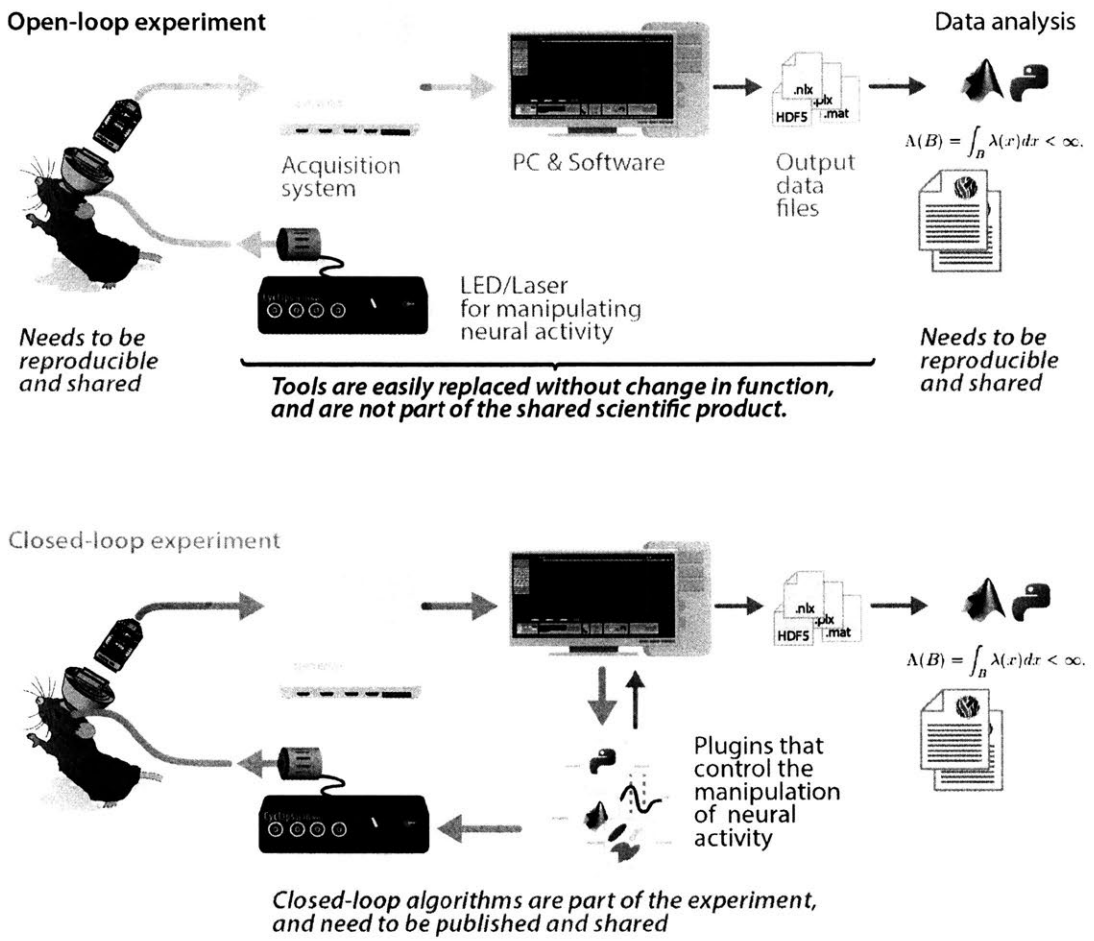

Figure A-3: **Closed-loop experiments require full sharing of methods.** In open-loop experiments (top), perturbations are carried out without taking brain state into account. In this case, only the details of the experimental setup, a description of the analysis methods, and the resulting data are the scientific product that is published and shared. In closed-loop experiments (bottom), algorithms are used to update the perturbation in real time, based on the state of the brain at a given moment. In this case, the exact function of the algorithm that interacts with the experimental preparation needs to be shared in order to make interpretation of the experiment possible.

tem. The key variable that affects whether a given closed-loop experiment is technically feasible from the point of view of the acquisition system is the round-trip latency, that is the time between an event in the incoming data, and the reaction to this event on some actuator.

The approach that we're taking with open ephys is to attempt to make the system fast enough to allow researchers to use well defined and replicable software algorithms in place of faster, but less replicable hardware or hybrid solutions. To make up for the sacrifice in speed that comes with running algorithms on commodity hardware, the data acquisition needs to be sufficiently fast, and the software needs to be designed in a way that minimized introduction of additional delays for data buffering. Currently, due to the limitations of the USB interface, algorithms in software are limited to round-trip times of of around 10ms on the open ephys system which is enough for applications of neural state estimation or manipulation of neural activity at the theta ($6-10$Hz) time scale (Siegle and Wilson, 2014), but not fast enough to react to individual spikes, or other fast neural events reliably, and certainly not fast enough to perform dynamic-clamp like (Scott, 1979; Sharp et al., 1992) experiments. Other, similar systems, most notably SpikeGadgets (`spikegadgets.com`) and Ripple (`rippleneuro.com`) are interfacing Intan (and similar) chips to PCs with an Ethernet protocol instead of USB and are achieving latencies of down to ~1ms.

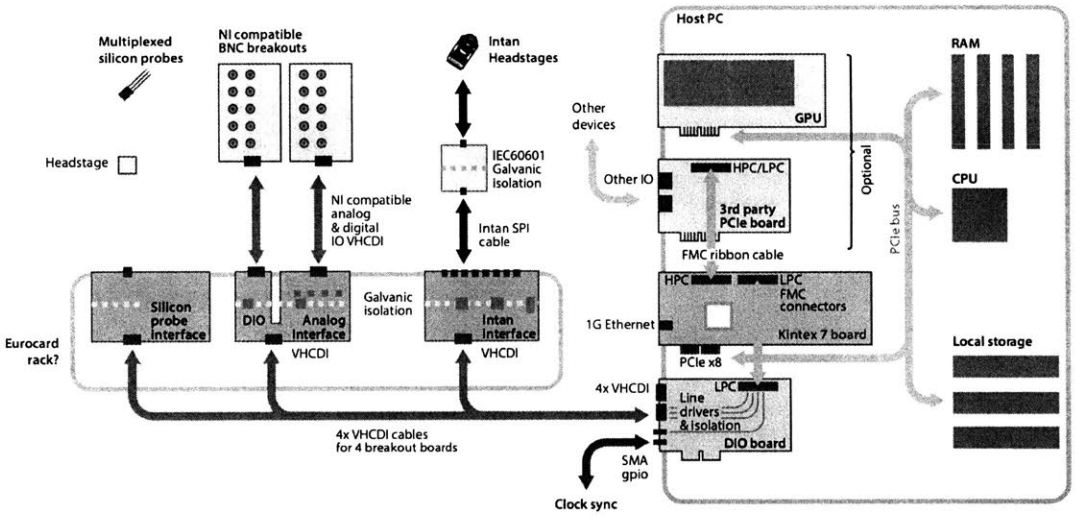

Figure A-4: **Overview of proposed PCIe based data acquisition system.** Example hardware configuration of a Open Instruments system with three connected breakout boards. Tha basis for the system is a Kintex kc705 fpga board (green). In addition to the DIO board (blue) that provides the electrical connections between the FPGA and the breakout boards (red), a 3rd party FMC board is shown, connected to the FPGA through the second FMC connector.

Beyond the latencies of low-level ethernet, the next step (`https://github.com/open-ephys/next-gen-system/`) is to bypass most interface protocols and write neural data directly into the memory of the acquisition PC via DMA over PCIe. This approach will make it possible to reduce latencies to well below 1ms and make it possible to implement closed-loop

interventions that will only be limited by the available computing resources rather than by the latency of access to the experimental system.

The proposed system architecture will also decouple the interface between user software and the hardware-specific firmware from the data acquisition hardware, making it easier for developers of new methods to develop practical working systems, and avoiding the redundant effort of re-implementing this interface for each new tool Fig.??. Standardizing this interface will also make it possible to seamlessly integrate multiple data sources into heterogeneous but prefectly synchronized data streams.

Bibliography

Abramoff, M. D., Magalhães, P. J., and Ram, S. J. (2004). Image processing with ImageJ. *Biophotonics international*, 11(7):36–42.

Cajigas, I., Malik, W. Q., and Brown, E. N. (2012). nSTAT: Open-source neural spike train analysis toolbox for Matlab. *Journal of Neuroscience Methods*, 211(2):245–264.

Denk, W., Strickler, J. H., and Webb, W. W. (1990). Two-photon laser scanning fluorescence microscopy. *Science*, 248(4951):73–76.

Dombeck, D. A., Khabbaz, A. N., Collman, F., Adelman, T. L., and Tank, D. W. (2007). Imaging large-scale neural activity with cellular resolution in awake, mobile mice. *Neuron*, 56(1):43–57.

Harrison, R. R. (2007). A Versatile Integrated Circuit for the Acquisition of Biopotentials. In *IEEE Custom Integrated Circuits Conference, 2007. CICC '07*, pages 115–122.

Newman, J. P., Zeller-Townson, R., Fong, M.-f., Arcot Desai, S., Gross, R. E., and Potter, S. M. (2013). Closed-loop, multichannel experimentation using the open-source NeuroRighter electrophysiology platform. *Frontiers in Neural Circuits*, 6:98.

Scott, S. W. (1979). *Stimulation Simulations of Young yet Cultured Beating Hearts*. PhD thesis, State University of New York at Buffalo.

Sharp, A. A., Abbott, L. F., and Marder, E. (1992). Artificial electrical synapses in oscillatory networks. *Journal of Neurophysiology*, 67(6):1691–1694.

Siegle, J. H., Hale, G. J., Newman, J. P., and Voigts, J. (2015). Neural ensemble communities: Open-source approaches to hardware for large-scale electrophysiology. *Current Opinion in Neurobiology*, 32:53–59.

Siegle, J. H. and Wilson, M. A. (2014). Enhancement of encoding and retrieval functions through theta phase-specific manipulation of hippocampus. *eLife*, 3:e03061.

Voigts, J., Herman, D. H., and Celikel, T. (2015). Tactile object localization by anticipatory whisker motion. *Journal of neurophysiology*, 113(2):620–632.

Voigts, J., Sakmann, B., and Celikel, T. (2008). Unsupervised whisker tracking in unrestrained behaving animals. *Journal of neurophysiology*, 100(1):504–515.

Voigts, J., Siegle, J. H., Pritchett, D. L., and Moore, C. I. (2013). The flexDrive: An ultra-light implant for optical control and highly parallel chronic recording of neuronal ensembles in freely moving mice. *Frontiers in Systems Neuroscience*, 7.

Wagenaar, D., DeMarse, T. B., and Potter, S. M. (2005). MeaBench: A toolset for multi-electrode data acquisition and on-line analysis. In *2nd International IEEE EMBS Conference on Neural Engineering, 2005. Conference Proceedings*, pages 518–521.

Warby, S. C., Wendt, S. L., Welinder, P., Munk, E. G. S., Carrillo, O., Sorensen, H. B. D., Jennum, P., Peppard, P. E., Perona, P., and Mignot, E. (2014). Sleep-spindle detection: Crowdsourcing and evaluating performance of experts, non-experts and automated methods. *Nature Methods*, 11(4):385–392.